Master Thesis

Best Practices for Adjoint-based Shape Optimization of Turbomachinery Stages

H.J.P.M. Gaens

TU Delft

Aan mijn ouders,
zonder wie niets van dit alles mogelijk was geweest

Best Practices for Adjoint-based Shape Optimization of Turbomachinery Stages

Master Thesis

by

Hendrik J.P.M. Gaens

in partial fulfillment of the requirements for the degree of

Master of Science

in Aerospace Engineering

at the Delft University of Technology,

to be defended publicly on Tuesday 16th of June, 2020 at 9:30 AM.

Student number:	4352858	
Supervised by:	Dr. Ir. M. Pini	TU Delft - Propulsion & Power
Thesis committee:	Prof. Dr. Ir. P. Colonna	TU Delft - Propulsion & Power
	Dr. Ir. R. Dwight	TU Delft - Aerodynamics
	Dr. Ir. M. Pini	TU Delft - Propulsion & Power
	Ir. A. Giuffré	TU Delft - Propulsion & Power

TU Delft

Acknowledgements

This master thesis is the result of close to a year of research work and the culmination of more than a lustrum as a student at Delft University of Technology. Both the journey and its destination would not have been the same without the love, friendship, help, support and guidance from the people around me.

I would first of all like to extend my gratitude to my thesis supervisor, Matteo, for his inspiration, motivation and expertise. I truly enjoyed and learned from his open and enthousiastic cooperation. By extension, I want to thank the entire Turbomachinery group for the strong and inclusive collaboration: it has been a pleasure being part of the team. In particular, thank you to Andrea, Antonio and Nitish for their availability, advice and guidance.

None of this would have been possible without the constant and unconditional love and support of my parents, Jan and Annemie, and my sister Emma. They inspire and encourage me to give my very best, both in my work and as a person. I also want to thank the rest of my family, whom I can always count on.

Finally, I want to thank my friends for their support and encouragement, and most of all for contributing to the countless fun, happy and memorable moments over the years. A particular acknowledgment goes to Wouter, Frederic, Bart, Anna, Jonathan and Johannes for their input to this master thesis.

Hendrik J.P.M. Gaens
Delft, June 2020

Abstract

In the pursuit of a new ultra-efficient generation of turbomachines, novel and more sophisticated flow simulation and optimization methods have to be adopted. With the development of harmonic balance (HB) methods and adjoint optimization, questions arise on the concrete benefits of using one method over another. This research investigates the difference in predictive capability and computational cost between unsteady harmonic balance and steady-state flow solving methods in particular. The research is performed using the *SU2* software suite. The relevant set of scaling parameters is established based on a dimensional analysis. Variation of several of these nondimensional parameters - namely the flow and work coefficient, specific heat ratio γ, isentropic pressure-volume exponent γ_{Pv} and volumetric flow ratio - constitute the different setups. Given the excessive computational times associated with full optimizations, this large set of case studies is subjected to one flow evaluation. Trends and conclusions are made based on the resulting data. It is found that the accuracy difference between steady and HB solvers decreases slightly with an increase in flow coefficient as reduced frequency goes down, and increases significantly with the stage work coefficient as Mach effects increase. Varying working fluids under the ideal gas law is found not to impact the stage and solver performance given the volumetric flow ratio as a similarity parameter. In cases where γ_{Pv} is significantly larger than γ, a major increase in stage Mach numbers is observed. Consequently, the difference between results found by steady-state and harmonic balance solvers is considerably larger. Upon increasing the volumetric flow ratio over the stage, stage efficiencies have been found to increase and solver performance differences to decrease. A pair of complete optimizations then aims to bring additional insights and to verify the validity of the simulation results. The optimizations illustrate the effects of the behavior observed in flow simulations on a full optimization process and reiterate the difference in computational time between both methods. In both cases, the HB-optimized turbine stages are more efficient than the equivalent steady-optimized cascades, namely by 0.58% and 0.12%. The predictive capability of steady-state solvers in comparison with unsteady solvers is found to be dependent on reduced frequency, work coefficient and stage maximum Mach number. A new parameter consisting of those three quantities, the adjusted reduced frequency, forms a linear relationship with the deviation in steady versus unsteady results. It can thus be used as an indicative parameter in preliminary design to trade off accuracy and computational time and select the right solver for a given case.

Contents

List of Figures ix

List of Tables xi

1 Introduction 1

2 Background 5

2.1 Losses and Unsteadiness . . . 5

2.2 Flow Solver . . . 6

2.2.1 Overview of Flow Solving Methods . . . 6

2.2.2 Harmonic Balance Method . . . 7

2.3 Shape Optimization . . . 15

2.3.1 Overview of Shape Optimization Methods . . . 15

2.3.2 Adjoint Optimization . . . 17

2.4 SU2 . . . 20

2.5 Non-ideal Compressible Flow . . . 21

3 Methodology 25

3.1 Similarity and Scaling Principles . . . 26

3.2 Geometry Generation . . . 27

3.3 Meshing . . . 29

3.4 Simulation . . . 30

3.5 Optimization . . . 32

3.5.1 Mesh Deformation . . . 33

3.5.2 Adjoint Implementation . . . 34

3.6 Post-Processing . . . 34

3.7 Best Practices . . . 35

4 Case Studies **37**

4.1 Overview of Test Cases . . . 37

4.2 Stage Type (Duty Coefficients) . . . 38

4.3 Working Fluid . . . 39

4.4 Volumetric Flow Ratio . . . 41

4.5 Technical Approach . . . 42

5 Results and Discussion **45**

5.1 Flow Simulations . . . 45

5.1.1 Convergence and Results . . . 45

5.1.2 Effect of Change in Duty Coefficients . . . 49

5.1.3 Effect of Change in Working Fluid . . . 53

5.1.4 Effect of Change in Volumetric Flow Ratio . . . 56

5.2 Optimization . . . 59

5.2.1 Gradient Validation . . . 59

5.2.2 Optimization Case 1: Stage A1 Operating with Air . . . 61

5.2.3 Optimization Case 2: Stage B1 Operating with Air . . . 66

5.3 Guidelines for Design Optimization . . . 71

6 Conclusion and Recommendations **75**

6.1 Conclusion . . . 75

6.2 Recommendations . . . 76

Bibliography **79**

List of Figures

2.1 Mean flow (zeroth harmonic) of unsteady pressure distribution for vibrating rotor airfoil. 11

2.2 URANS and HB comparison: unsteady mass flow rate and efficiency. 13

2.3 URANS and HB comparison: time-averaged mass flow rate and efficiency. 13

2.4 Entropy at midspan. 14

3.1 Experimental flow diagram. 25

3.2 Visualization of the different boundary conditions applied to the flow domain. 31

3.3 Optimization algorithm structure. 33

3.4 Free-form deformation boxes. 33

4.1 Simulation variables. 37

4.2 Smith chart with investigated stage types. 38

4.3 All nine stage geometries. 40

4.4 Mesh of stage *C1*. 41

4.5 Total-to-total efficiency variation for different time instances. 43

5.1 Mesh convergence study of stage *C1*. 46

5.2 Convergence history of the flow simulation of stage *C1*. 47

5.3 Entropy generation. 48

5.4 Efficiency deviation, reduced frequency and Mach number in function of flow and work coefficient. 49

5.5 Total-to-total efficiency difference between steady-state and HB flow simulation in function of reduced frequency for stage *A1*. 50

5.6 Normalized entropy contours of a steady-state versus harmonic balance flow simulation of stages *A1* and *C2*. 51

5.7 Relative Mach contours of a steady-state versus harmonic balance flow simulation of stages *A1* and *C2*. 52

5.8 Stator pressure fields. 53

5.9 Total-to-total efficiency and total-to-total efficiency difference between steady-state and HB flow simulation in function of γ. 54

5.10 Relative Mach contours of stage *A1*. 57

5.11 Relative Mach contours of stage *A1*, HB - t =0. 58

5.12 Gradient validation. 60

5.13 Adjoint surface sensitivity vectors. 60

5.14 Optimization history of stage *A1* with air as ideal gas. 61

5.15 Total-to-total efficiency of baseline and optimized blade shapes of stage *A1* in function of time. 62

5.16 Baseline versus optimized blade shapes of stage *A1* with air as ideal gas. 63

5.17 Relative Mach contours of stage *A1*. 64

5.18 Isentropic Mach over stator chord of stage *A1* with air as ideal gas. 65

5.19 Entropy contours of stage *A1*. 66

5.20 Optimization history of stage *B1* with air as ideal gas. 67

5.21 Baseline versus optimized blade shapes of stage *B1* with air as ideal gas. 68

5.22 Relative Mach contours of stage *B1*. 69

5.23 Isentropic Mach over stator chord of stage *B1* with air as ideal gas. 70

5.24 Entropy contours of stage *B1*. 70

5.25 Total-to-total efficiency difference between steady-state and HB flow simulation in function of adjusted reduced frequency. 73

List of Tables

3.1 *Meangen* input parameters. 28

3.2 *UMG2* mesh element size options. 30

4.1 Characteristics of stage *C1*. 39

4.2 Selected working fluids. 39

4.3 Nonideal fluid case input. 41

5.1 Mesh convergence study for *C1*. 46

5.2 Nondimensional parameter validation of stage *C1*. 48

5.3 Characteristics of ideal and non-ideal MM in stage *A1*. 56

5.4 Characteristics of different volumetric flow ratios in stage *A1*. 58

5.5 Optimization results for stage *A1*. 62

5.6 Optimization results for stage *A1*. 65

5.7 Optimization results for stage *B1*. 67

5.8 Optimization results for stage *B1*. 69

Nomenclature

β	Expansion ratio - P_{t_i}/P_{s_o}
η	Efficiency
ϕ	Flow coefficient
ψ	Work coefficient
ρ	Density
σ	Solidity
h	Enthalpy
Ma	Mach number
p	Pressure
r^*	Degree of reaction
R_v	Volumetric flow ratio - ρ_{t_i}/ρ_{s_o}
s	Entropy
T	Temperature
U	Rotational speed
y_p	Blade pitch
2D	Two-dimensional
AD	Algorithmic Differentiation
CFD	Computational Fluid Dynamics
CFL	Courant-Friedrichs-Lewy
CPU	Central Processing Unit
FD	Finite Differences
FFD	Free Form Deformation
HB	Harmonic Balance
JST	Jameson–Schmidt–Turkel
LE	Leading Edge
MP	Mixing Plane
RANS	Reynolds Averaged Navier-Stokes
SA	Spalart-Allmaras
SST	Shear Stress Transport
TE	Trailing Edge

1

Introduction

The aerospace industry and by extension the entire energy and transportation sectors are faced by an ever-increasing challenge to reduce their negative environmental impact. Key to reaching this goal is the improvement of the efficiency of thermal engines. These are found in the aforementioned fields in the form of aero-engines, thermal power plants, turbochargers and many more. Understanding the flow characteristics of these turbomachines is paramount to enhancing their performance and efficiency.

Mere decades ago, the only way of determining the flow properties of turbomachines and of optimizing their performance was using basic analytics, correlations and experimentation [1]. Computational fluid dynamics (CFD) was pioneered in the 1960s, when available computer power became capable of solving flow equations. Since then, it has evolved to the point where its speed and versatility have now made it a key tool in flow solving and optimization [2, 3]. CFD has significantly increased the accuracy with which flow behavior can be predicted, and as a result paved the way to improved efficiency in compressor and turbine stages.

Due to CPU and time limits, computational fluid dynamics is inherently tied to the use of certain models that rely on simplifications of occurring phenomena. Steady-state based flow solvers, which assume time-invariant flow, have long been the industry standard for shape optimization [4]. They generally provide decent results and very good computational resource efficiency. However, in order to develop ultra-efficient turbomachines for the next generation of thermal engines, new flow simulation and optimization methods must be adopted. Due to the presence of rotating elements, flow in turbomachinery is characterized by the appearance of various unsteady flow phenomena. Shocks, vorticity and wake interaction are among several phenomena closely tied to turbomachinery that evolve over time [5]. Taking these into account in the simulation will be central to improving the design of turbomachines. Apart from their higher accuracy in flow solving, unsteady simulations enable designers to tackle a wider range of multidisciplinary design problems, by allowing the modeling of aeroelastic effects among others. Traditional time-accurate unsteady solutions - especially in an optimization context - are notoriously costly in terms of memory and computational time [6]. This renders them impractical for optimization purposes in an industrial context. More recently, harmonic balance methods (HB) have increased interest within the turbomachinery community due to the significant advantages they offer compared to more traditional solvers. These reduced order methods are developed to exploit the fact that most flow unsteadiness in turbomachines is (quasi-)periodic in nature. This assumption allows to resolve flows in the frequency domain as if they were steady, for a given set of (blade passing) frequencies. The harmonic balance method offers a compromise between accuracy and required computational

power.

In general, optimization methods are based on the idea that certain (geometric) parameters are automatically changed after which a flow evaluation of the given setup is performed. This process is then repeated until a certain optimal set of parameters is determined. Therefore, two main features of the optimization process determine its computational time: the CPU time of the evaluation itself, which is dependent on the type of solver used, and the number of evaluations required, which is determined by the type of optimization algorithm. Gradient-based optimization methods are generally efficient and focused ways of getting to an optimum. Determining the gradient itself can be done in a few different ways but is generally a computationally intensive calculation. Adjoint optimization methods offer a way to efficiently obtain the gradient of the objective function. They stand out in their ability to calculate gradients such that computational time is independent of the amount of design parameters, making it very interesting for optimization problems in turbomachinery [7].

In the current plethora of optimization methods and steady and unsteady CFD models available for turbomachinery applications, questions may still arise about the actual benefits of using one optimization method over another. The harmonic balance method, as described above, generally offers better accuracy and higher predictive capability over an equivalent steady-state CFD model, but at the expense of a much higher computational cost (at least one order of magnitude in terms of RAM memory requirement and three times in terms of runtime cost). Given that the flow physics within a turbomachine stage are mostly governed by a few dimensionless parameters, there should be a relation between these and the actual benefits a HB-based optimization method would ultimately provide to the designer. In other words, in the quest of developing next-gen turbomachines, do unsteady optimization methods provide advantages over steady-state ones? If so, when does the increased accuracy of the harmonic balance method outweigh the decreased computational time of a steady-state one? This work aims to fill this knowledge gap.

More concretely, a design guideline is set out that will allow for the selection of the best-suited optimization method for a given design problem. Accuracy and computational performance of steady-state and harmonic balance methods will be compared. There will be special focus on their implementation, the optimization algorithm and the variation of working fluid - given the recent interest in organic Rankine cycles and other exotic turbomachinery. The investigation is carried out by focusing on two-dimensional axial turbine stages.

Research objectives

From the identified knowledge gap, the following research objective can be defined:

Contribute to the field of turbomachinery design by providing best practices on what flow solving method to use for a specific turbomachinery design problem.

A main research question can be formulated based on this objective.

For which turbine applications is it convenient to resort on adjoint-based unsteady (harmonic balance) design methods for the fluid-dynamic optimization of the stage?

More precisely, the research project is aiming to provide an answer to the following sub-questions:

1. Which fundamental flow and stage parameters are expected to have the largest effect on the difference in outcome between steady-state and harmonic balance based shape optimization?
    - Which fundamental parameters make up the nondimensional groups governing similarity?
    - How do these parameters affect the difference in outcome between steady-state and harmonic balance based shape optimization?
    - What are the physical explanations for the observed trends and behavior?
2. What is the effect of variations in the selected flow and stage design parameters on the difference in optimal blade shape and efficiency obtained using harmonic balance and steady-state flow solving methods in adjoint optimization?
    - What are the major quantitative trends in the difference in flow results when changing the given flow and stage parameters?
    - What are the major quantitative trends in the difference in optimal blade shape and efficiency when changing the given flow and stage parameters?
    - What are the physical explanations for the observed trends and behavior?
3. Is it possible to set up a design guideline that can help in deciding whether to use an unsteady or steady-state CFD model for the optimization of a certain turbine stage?
    - What is the relation between accuracy of results and computational time for both flow solving methods and for changing flow and stage parameters?
    - Can boundaries be defined within a design space of flow and stage parameters within which to use one of both flow solving methods?

Two hypotheses are set out for this research project, based on these aforementioned research questions and objectives.

1. Variation in the selected flow and stage characteristics results in a clear and consistent difference in blade shape and efficiency resulting from optimizations using steady-state and harmonic balance methods.
2. It is possible to translate the observations referred to in hypothesis 1 into a sound design guideline or tool.

Report outline

This report aims to convey the work done in this research as well as discuss its results. It is subdivided into several parts. Chapter 2 presents the reader with background information on previous work done in flow simulation and blade shape optimization. Chapter 3 then introduces the methodology that was followed throughout the research, from meshing to adjoint implementation. Chapter 4 subsequently describes the selection and set-up of the case studies in the research. The simulation and optimization results are presented and discussed in chapter 5. Finally, the report is concluded in chapter 6.

2

Background

This chapter presents a selection of some of the literature and state-of-the-art on the most relevant topics within the scope of this research project.

2.1. Losses and Unsteadiness

There are a number of different loss generative processes that can be identified in axial turbines. Understanding these loss mechanisms and the underlying (unsteady) flow physics is key to anticipating and later explaining the flow and solver behavior in the simulations and optimizations performed throughout this research.

The three main classical types of losses in two-dimensional turbomachinery are boundary layer, mixing and shock losses. Boundary layer or friction loss is the energy lost due to viscous dissipation and is associated with shear forces as a result of the velocity gradient between the blade wall and what can be considered the free flow. The velocity gradient found in the boundary layer is not linear: in most cases, velocity change and consequently entropy generation are larger close to the blade surface [8]. They are found to increase with Reynolds number. The phenomena at their core are relatively independent from flow unsteadiness.

Mixing losses are encountered at the outflow of a cascade. They encompass an array of different mechanisms. Viscous shear strain occurs in vortices and wakes. Thermodynamically, entropy is generated when flows at different velocities and/or temperatures are mixed. In a turbomachinery setting, this situation presents itself in mixing of flow from pressure and suction sides of a blade, or from a separated boundary layer. Mixing losses and their underlying flow phenomena are strongly associated with unsteady flows, and are therefore especially interesting in discussing differences between steady and unsteady solver performance.

Being irreversible in nature, shock waves are by definition sources of entropy. Oblique shock waves as found in turbines account for less entropy generation than an equivalent normal shock. Consequently, the loss in shocks within the blade passage is often not the main negative effect of transonic flow in a turbine cascade. More worryingly, the resulting shock system may cause havoc downstream, majorly increasing trailing edge loss and facilitating boundary layer separation [8].

Key to this research is the notion of unsteadiness in flows in turbomachinery. Unsteadiness as a term is used to describe those flow phenomena that change with time. A parameter that specifically indicates the level of unsteadiness of a flow field is the reduced frequency (f_r). This reduced frequency represents the ratio between the time scale of the transport and the time scale of the unsteadiness [9]. The unsteadiness time scale is defined as the stator pitch y_p over the peripheral velocity U. The transport time scale is proportional to the axial chord b and inversely proportional to the axial velocity V_{ax}. The reduced frequency can alternatively be written in function of the solidity σ and the flow coefficient ϕ. Equation 2.1 presents the equation for the reduced frequency.

$$f_r = \frac{b\ U}{y_p\ V_{ax}} = \frac{\sigma}{y_p} \tag{2.1}$$

If the f_r is smaller than one, transport of phenomena dominates, and the flow can be assumed (quasi) steady. In the opposite situation, with $f_r \gg 1$, the process is deemed unsteady.

Unsteadiness is an inherent property of flows in turbomachinery, given the presence of rotating elements. Spatial non-uniformities like static pressure fields, (stator) blade wakes, shock waves and vortex structures turn into time non-uniformities in the rotating frame of reference [9].

Static pressure fields are radial non-uniformities in pressure resulting from an upstream blade row. The pressure field usually goes back to uniform after one to two chord lengths. In most cases, a stage row will therefore still experience the static pressure disturbance created by the upstream blade. Blade wakes are regions of disturbed and decelerated flow downstream of a blade - or any solid body in a flow for that matter. They are often associated with separated boundary layers and flow mixing. Another type of unsteady phenomena common to flows in turbomachines are vortical structures. These kinds of secondary flows are often found at the hub or tip of a 3D blade. Vortices can interact with other vortices or with wakes to generate more complex flow disturbances. Shock waves are a result of supersonic Mach numbers. They affect the pressure distribution downstream and impact the next blade row in a way not too different from the general static pressure fields previously described. A common parameter of these phenomena is their forcing frequency. This frequency, which represents the periodicity of the effects of the disturbance on the downstream - often rotor - row. In the case of the unsteady flow characteristics described here, the forcing frequency is equal to the blade passing frequency, defined as the vertical speed of the rotor blade divided by the stator pitch.

$$f_b = \frac{U}{y_p} \tag{2.2}$$

2.2. Flow Solver

2.2.1. Overview of Flow Solving Methods

Over its existence, computational fluid dynamics (CFD) has evolved to become an indispensable tool in analysis, design and optimization of turbomachinery [2, 3]. At the moment, adjoint-based shape optimization methods in turbomachinery generally make use of the steady flow assumption [7]. In simplifying the flow situation to steady-state, one assumes that the flow and its accompanying properties are invariant in time. Not having to deal with a time derivative makes steady flow solving and optimization very computationally efficient.

Two main techniques are in use for steady flow solving over multiple blade rows, : mixing plane and

frozen rotor. The mixing plane (MP) approach considers the rotor and stator row as two separate problems. At their interface, properties from one zone are averaged and serve as a uniform boundary condition to the next. It is immediately clear that this approach introduces inaccurate physical behavior in a turbomachinery context, where wake and shock interaction and their propagation into the next row are important phenomena. At first sight, these issues are resolved in the frozen rotor approach, where the true flow is passed through to the following stages. However, this method introduces new physical inconsistencies, as it solves for these stages at a set frozen relative position. In a rotating system, this has no real physical meaning: the rotation of the row is not taken into account, making propagation of phenomena not true to reality. On top of that, this 'snapshot' position of both stages does not represent global properties of a certain stage over time. Consequently, a mixing plane is used in all steady-state simulations performed throughout this research.

As touched upon in the previous section, flow in turbomachinery is inherently unstable. While steady optimization techniques have served the industry rather well, in order to further improve on the design of turbomachines, more accurate techniques are absolutely necessary. Unsteady flow solving introduces an entire new level of challenge and complexity. They preferably preserve the accurate spatial discretization from steady-state models, while also resolving the time history of the solution.

Three major types of unsteady flow solution methods can be identified: time-linearized, nonlinear time-accurate and harmonic balance methods. The time-linearized method assumes unsteady disturbances to be very small in comparison with the mean flow variables. Doing so makes it possible to see the nonlinear unsteady flow as a combination of a nonlinear mean flow and a linear small disturbance. While the eventual time-linearized equations are efficiently solvable, time-linearized methods are limited by the same small disturbance assumption they are based upon, in the sense that they prevent the method from being able to model dynamically nonlinear problems [10] . The nonlinear time-accurate method differs heavily from time-linearized methods. The time-accurate technique directly solves nonlinear flow problems, and therefore delivers high accuracy. As the flow phenomena are to be resolved at every single time step, these time-accurate models come at heavy computational costs. A time-accurate analysis may take up to 100 times as long as an equivalent time-linearized solver [10]. The harmonic balance method has been developed in an effort to obtain new and more efficient ways of simulating non-linear unsteady flows. Problems like internal flows in turbomachines or external flows around helicopter rotors are characterized by flows that are temporally and spatially periodic. Their unsteadiness can often, at least to a large degree, be represented in terms of a finite number of discrete finite dominant frequencies. A smaller number of analyses can be done, which can be Fourier extrapolated based on this principle. The result is a major computational benefit compared to time-accurate solution methods. Both frequency- and time-domain harmonic balance methods exist.

2.2.2. Harmonic Balance Method

As explained previously, the harmonic balance method has been developed to offer an alternative to both steady solvers and well-resolved time-accurate unsteady solvers. The idea behind the harmonic balance method is to cast the unsteady governing equation in a set of coupled steady equations corresponding to a uniform sampling of the flow within the time period [4]. This is done by decomposing time-dependent flow variables into Fourier series. The flow equations then use these Fourier coefficients as the unknown variables. This is where two methods diverge: the frequency-domain and time-domain harmonic balance method.

Frequency-domain harmonic balance methods solve the Fourier coefficients directly. Their idea is similar to the earlier discussed time-linearized methods in that they divide the flow field into a steady (linear) or time-averaged (nonlinear) and an unsteady perturbation part. In this case however, this quasi-

periodic perturbation equation is solved not in time but in frequency domain [11–13]. Again, due to the small disturbance flow assumption involved, this method is unable to model dynamic nonlinearities. Therefore, not frequency- but time-domain harmonic balance methods are used for the scope of this research project. They cast the equation back to time domain using inverse Fourier transforms, as will be showed mathematically later.

In the mixed time-/frequency-domain harmonic balance method proposed by Hall [14], the unsteady nonlinear flow is described by a Fourier series in time. Using an harmonic balance technique, a set of coupled steady partial differential equations corresponding to a uniform sampling of the flow within the time period is written for the Fourier coefficients. Implementing a pseudo-timestep, the equations can then be solved using time-marching techniques [14]. The ability to solve these steady equations using conventional Reynolds Averaged Navier-Stokes (RANS) methods also makes it possible to apply their convergence acceleration techniques [4].

Next, a mathematical derivation of the time-domain harmonic balance is shown step by step, based on literature [2, 4, 14–17]. The semidiscrete form of the Navier-Stokes equations in Cartesian coordinates can be written as:

$$V\frac{\partial \mathbf{U}}{\partial t} + R(\mathbf{U}) = 0 \tag{2.3}$$

U is the vector of conservative variables, equal to $(\rho, \rho v_1, \rho v_2, \rho v_3, \rho E)$. $R(\mathbf{U})$ represents the residual vector from the spatial discretization of the viscous and convective fluxes. V is the cell volume. Time discretizing 2.3 yields:

$$V\mathcal{D}_t(\mathbf{U}^{q+1}) + R(\mathbf{U}^{q+1}) = 0 \tag{2.4}$$

Finally, adding a fictitious pseudo-time term in order to march to a steady-state condition, results in the following problem:

$$V\frac{\Delta \mathbf{U}^{q+1}}{\Delta\tau} + V\mathcal{D}_t(\mathbf{U}^{q+1}) + R(\mathbf{U}^{q+1}) = 0 \tag{2.5}$$

Subsequently, the discrete Fourier transform is applied to the vector of conservative variables U. The resulting Fourier coefficients are:

$$\hat{U}_k = \frac{1}{N}\sum_{n=0}^{N-1} U_n e^{-i\omega_k t_n} \tag{2.6}$$

$[U_0, U_1, ..., U_{N-1}]$ makes $\tilde{\mathbf{U}}$, the vector of the conservative variables evaluated at N time instances. $\hat{\mathbf{U}}$ is the vector of corresponding Fourier coefficients $[\hat{U}_0, \hat{U}_1, ..., \hat{U}_{N-1}]$ The number of time instances in the interval (N) and frequencies (K) are often related as $N = 2K + 1$. Larger amounts of time instances or non-uniform time instances have been studied and implemented, and described in literature. The Fourier coefficients can also be presented by the product of the discrete Fourier transform matrix (DFT) **E** and the vector of the conservative variables at N time instances:

$$\hat{\mathbf{U}} = \mathbf{E}\tilde{\mathbf{U}} \tag{2.7}$$

The DFT matrix **E** is defined by:

$$E_{k,n} = \frac{1}{N} e^{-i\omega_k t_n} \tag{2.8}$$

The inverse is also true:

$$\tilde{\mathbf{U}} = \mathbf{E}^{-1}\hat{\mathbf{U}} \tag{2.9}$$

with

$$E^{-1}_{k,n} = e^{i\omega_k t_n} \tag{2.10}$$

For the time derivative operator $\mathcal{D}_t$ from 2.4 yields:

$$\mathcal{D}_t(\tilde{\mathbf{U}}) = \mathcal{D}_t(\mathbf{E}^{-1}\mathbf{E}\tilde{\mathbf{U}}) = \mathcal{D}_t(\mathbf{E}^{-1}\hat{\mathbf{U}}) = \frac{\partial \mathbf{E}^{-1}}{\partial t}\mathbf{E}\tilde{\mathbf{U}} \Rightarrow \mathcal{D}_t = \frac{\partial \mathbf{E}^{-1}}{\partial t}\mathbf{E} \tag{2.11}$$

Taking the derivative of $\mathbf{E}^{-1}$ based on the definition in 2.10, one can write:

$$\frac{\partial \mathbf{E}^{-}1}{\partial t} = \mathbf{E}^{-1}\mathbf{D} \tag{2.12}$$

In this equation, **D** is built up as follows:

$$D_{k,n} = i\omega_k \delta_{k,n} \tag{2.13}$$

Here, δ is the Kronecker delta. Now, the spectral operator matrix **H** is defined as:

$$\mathbf{H} = \mathbf{E}^{-1}\mathbf{D}\mathbf{E} \tag{2.14}$$

Combining equations 2.11, 2.12 and 2.14, one can write:

$$\mathcal{D}_t(\tilde{\mathbf{U}}) = \mathbf{H}\tilde{\mathbf{U}} \tag{2.15}$$

Going back to the Navier-Stokes equations, one can write equation 2.5 at a single time instance as:

$$V\frac{\Delta \mathbf{U}_n^{q+1}}{\Delta\tau} + V\mathcal{D}_t(\mathbf{U}_n^{q+1}) + R(\mathbf{U}_n^{q+1}) = 0 \tag{2.16}$$

Additionally, it is possible to linearize the residual as shown here:

$$R(\mathbf{U}_\mathbf{n}^{\mathbf{q+1}}) = R(\mathbf{U}_n^q) + \frac{\partial R(\mathbf{U}_n^q)}{\partial(\mathbf{U}_n^q)}\Delta R(\mathbf{U}_n) \tag{2.17}$$

Making use of the linearity of the time derivative operator and its connection to the spectral operator matrix, the final set of equations is given by:

$$\left(\frac{VI}{\delta\tau} + \frac{\partial R(\mathbf{U}_n^q)}{\partial(\mathbf{U}_n^q)} + V\mathbf{H}\right)\Delta\mathbf{U}_n + R(\mathbf{U}_n^q) = -V\mathbf{H}\mathbf{U}_n^q \tag{2.18}$$

The result is a set of steady equations corresponding to N time instances within the period. They can now be solved using conventional steady solution methods. The new spectral time derivative operator as well as the far-field and periodic boundary conditions connect all time levels.

The resolved Fourier coefficients are then to be time sampled to obtain the unsteady solution in time domain. In multistage turbomachines, a row can be submitted to several blade passing frequencies. As a result, the harmonic balance method applied to solve the flow in a certain row will often take multiple frequencies that are not necessarily harmonically related. The Fourier coefficients are related to their respective physical quantities evaluated at certain time instances. The amount of time intervals and their distribution over the period have an effect on the solution and the stability of the flow simulation. Generally, at least two time instants per period are needed to capture a frequency, but an odd number is required for stability [17]. In the majority of literature and research, uniform time sampling is used, with the number of time instances N related to the amount of frequencies K as $N = 2K + 1$. It is clear that for one frequency for example, there are three time instances, complying with the requirement that has just been stated. In case of several frequencies, this minimum of three time instances is required over the shortest period. If the difference in frequency is very large, it makes that a lot of samples are required on the longest period. As a result, computational time increases.

Model Accuracy and Computational Performance

The harmonic balance method promises a significant improvement in the accuracy of the flow simulation compared to conventional steady flow solvers. Being an unsteady flow solving method, it allows for the simulation and resolution of flow characteristics that would not be observable in a steady simulation. As a consequence, when applied in an optimization context, its ability to more accurately resolve the flow will enable the optimization to result in a better final solution. At the same time, the reduced-order nature of the harmonic balance method makes it faster than time-accurate unsteady flow simulations. This section observes the performance of some harmonic balance implementations, and discusses how the harmonic balance method compares to steady and time-accurate unsteady flow solvers.

Hall [14] applied the harmonic balance method to the modeling of flutter on a 2D transonic rotor. The harmonic balance solution was determined using different amounts of harmonics, namely $N = 1, 3, 5 and 7$. It is clear from the results displayed in figure 2.1 that for case of really small amplitudes of motion, the solutions for different amounts of harmonics are almost identical. As the unsteadiness is so small ($\bar{\alpha} = 0.01$ deg), the resulting flow is equal to the steady flow, and the implementation of the harmonic balance method as well as the addition of multiple harmonics does not affect the outcome in a significant way. As unsteadiness grows, the relevance of using an unsteady flow solving method such as the harmonic balance method increases, as can be seen in the second plot in figure 2.1. Here, the effect of implementing larger numbers of frequencies can be seen as well, though apart from the solution with only one harmonic, they all give similar results. In computing the first harmonic of unsteady pressure and unsteady pitching moment, once again the harmonic balance solution with only one harmonic gives significantly different results and even non-convergence. This one-harmonic HB solution is effectively the same as a time-linearized solution, and therefore shows poor behavior at larger amplitudes of unsteadiness.

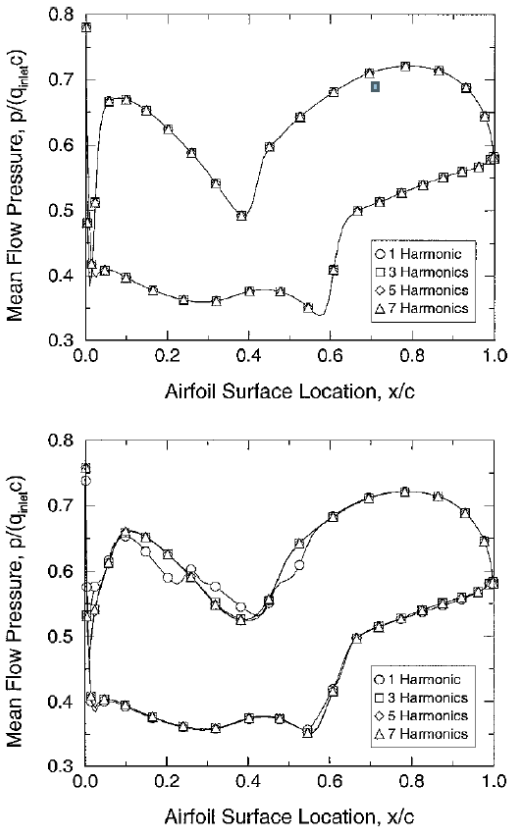

Figure 2.1: Mean flow (zeroth harmonic) of unsteady pressure distribution for vibrating rotor airfoil. Top: small-amplitude motion ($\tilde{\alpha}$ = 0.01 deg), bottom: large-amplitude motion ($\tilde{\alpha}$ = 1.0 deg) [14].

The results obtained by Huang [10] in a two-dimensional viscous turbine cascade under vibration tell a similar story. The resulting mean pressure distribution as well as the real and imaginary components of the first harmonic of that pressure coefficient again show that the harmonic balance method using only one harmonic gives deviating results, confirming the nonlinearity of the problem. As seen in Hall [14], increasing the amount of harmonics involved improves the accuracy of the simulation. The improvement itself gets smaller with increasing numbers of harmonics taken into account. The same behavior is found by others, including Ekici [18] and Cvijetic [19]. Huang additionally verifies the performance of his harmonic balance method against Petrie-Repar's time-linearized solver, which has proven its validity in similar setups. For both two-dimensional compressor cascades, the harmonic balance method shows great agreement with the reference solver. Due to the limits of the time-linearized solver however, this verification was performed for very small pitching amplitudes.

Rubino [7] compares the performance of the harmonic balance method and a steady solution method in an environment that is more relevant to the scope of this research project. Where Hall and Huang focused on vibration, Rubino investigates a two-row axial turbine stage for both subsonic and transonic conditions. Here, the unsteadiness does not come from (imposed) vibrations but from propagation of unsteady flow from subsequent rows and stator-rotor interaction. The steady simulations rely on a mixing-plane approach, the working of which has been explained previously in this report. The unsteady harmonic balance solver uses a sliding mesh method at the stator-rotor interface. In the sliding mesh technique, the cell zones will move relative to one another along their interface. It is commonly used in unsteady solutions, most often in time-periodic problems. Another point of particular interest concerning this research is the connection to adjoint optimization. The work is not limited to the discussion of flow results: adjoint sensitivities obtained using both steady and HB methods are compared.

Firstly, for both subsonic and transonic stages, entropy and pressure distribution results from the steady-state mixing plane and harmonic balance method are compared. Results from the subsonic stage show differences of between 3 % and 5 % in static pressure at the outlet of the stator, entropy and stage total-to-static efficiency. For the transonic case, while the difference in entropy generation is larger than before, the eventual difference in efficiency is close to non-existent. Shocks are found to occur on both stator and rotor blades. Subsequently, the design sensitivities are obtained from the adjoint solution (see section 2.3.2) for both the MP and HB method. They correspond to the gradient represented by the derivative of the entropy generation to changes in shape of the blades. The gradients are validated against gradients found using a second-order finite difference method. The main striking aspect in the results for the subsonic blade row is how the difference between the objective function gradients from MP and HB is rather small on the stator blade and very large for the rotor blade. The way in which both methods handle the stator-rotor interaction plays a major role in the reason for this discrepancy. The differences in gradient are mostly found close to the interface between both rows. In a MP situation, the flow at the row interface makes for different static pressures at the interface. On top of that, by averaging out the flow properties, the plenty unsteady flow phenomena such as wake interaction are not propagated into the rotor row. In the transonic blade row, while the difference between MP and HB-based sensitivities are still there, they are noticeably smaller than in the subsonic flow case. Furthermore, the differences on the rotor blade are less concentrated around the leading edge. The explanation for this finding is in the appearance of an additional flow phenomenon: shock waves. The shock waves that are generated in the stator row of the transonic flow case cross the interface and react with the wake, dissipating the effect of that wake and its interaction with the rotor. As the MP method gives discrepancies due to its inability to model the rotor-wake interaction, the dissipation of the wake makes its transonic solution less different from the solution obtained by the HB method. Additionally, as the MP method cannot capture the shock and its interactions, differences in the gradient are encountered on other locations on the rotor blade.

In terms of convergence and computational time, Hall [14] finds that with the harmonic balance method, the solution converges in about the same number of iterations for all N. Computational times per iteration are 2.15, 4.62 and 7.45 times as long as for the steady flow solver, for one, three and five harmonics (N) respectively. Huang [20] also shows that the convergence rates of the harmonic balance method for different amounts of harmonics are virtually equal. The computational time is then linearly dependent on the number of sub-time levels involved. Also in Rubino [7], computational cost of HB-based adjoint sensitivities are found to be around $2K + 1$ times higher than for steady-based gradients with K the number of modes.

Another interesting work in this field - and one that will act as a source of inspiration for this thesis work - is D'Amato's masters thesis '*A comparison between steady and unsteady methods for turbomachinery design using scaling analysis*' [21]. A particularly interesting idea in this work is that it does not just compare steady and harmonic balance methods for one case. Instead, the idea is to vary a number of flow and stage parameters to observe what such a change does to the difference between the results of both methods. Three test cases are set up based on combinations of flow coefficient ϕ and loading coefficient ψ. One is for a high efficiency stage (ψ and ϕ both around 0.5), one at a higher loading factor, and a final case where both flow and load coefficients are higher than the first stage. Three parameters are then varied, namely expansion ratio, working fluid and axial stage gap. Results show for example that the accuracy of steady-state analyses deteriorates with smaller axial stage gap. While D'Amato's work remains one of qualitative observations, this research aims to expand it, extend it to an optimization environment, and to define a more quantitative design tool or guideline of when to choose an unsteady analysis instead of a steady-state one.

Literature clearly confirms the significant advantage of the harmonic balance method over steady state-flow solvers in resolving nonlinear and unsteady flow features, while finding a very reasonable increase in computational time and cost. It is now interesting to compare the method to time-accurate

unsteady flow solvers in order to verify the accuracy of these HB techniques and get a sense of the computational time savings they offer. Sicot's [4] research shows a convergence study of a time-domain harmonic balance method and compares the results with the solutions obtained using a time-accurate unsteady flow solver. One stage of a subsonic compressor is resolved using both methods. The three time-instance computations fail to converge in the simulations of this research, probably due to the sampling being too coarse for good interpolations. Figure 2.3 shows the mass flow rate and the isentropic efficiency over the period for both Unsteady RANS (URANS) and HB. Looking at the left graph, it looks like the five time instant harmonic balance solution significantly underestimates the amplitude of the change in mass flow. Going up to seven time instants ($N = 7$) gives a trend that resembles the URANS reference more closely, but that now shows too large of an amplitude. Adding an extra frequency results in a very good match with the URANS solution. Increasing the number of time instances even further barely gives any observable increase in accuracy. Looking at the isentropic efficiency, it is immediately clear that both five and seven HB instants result in a very poor approximation. Implementing nine gives a much better result and eleven and more time instants give solutions very close to the one obtained using the time-accurate solver. Figure 2.2 shows the same physical quantities but averaged over the entire period. Again, as expected, increasing the amount of time instants brings the harmonic balance solution closer the the unsteady flow solution. In general it is clear that the harmonic balance technique gives results that are very close to those obtained using the time-accurate unsteady solver. Figure 2.2 also shows the corresponding results found using a steady mixing plane method, and thus it illustrates the results of the harmonic balance method being significantly closer to the URANS than to the MP solutions.

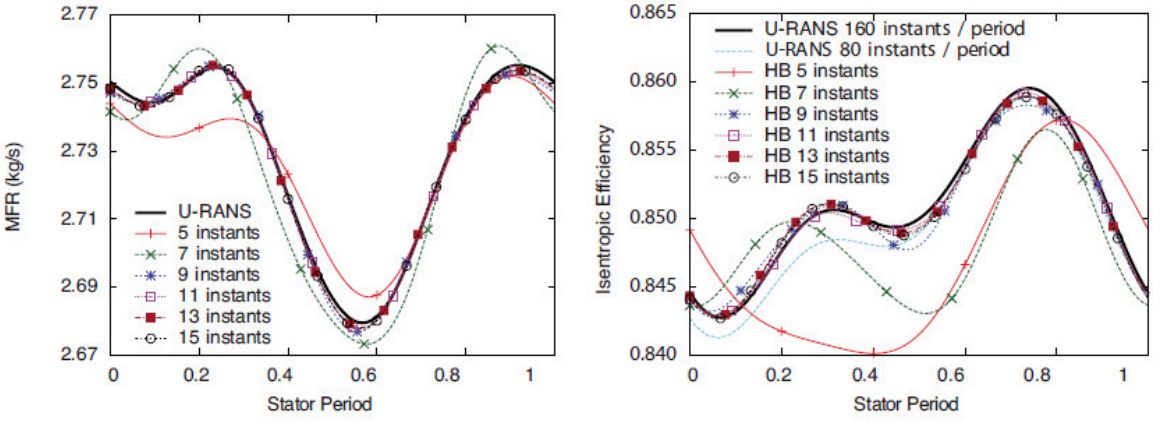

Figure 2.2: URANS and HB comparison: unsteady mass flow rate and efficiency [4].

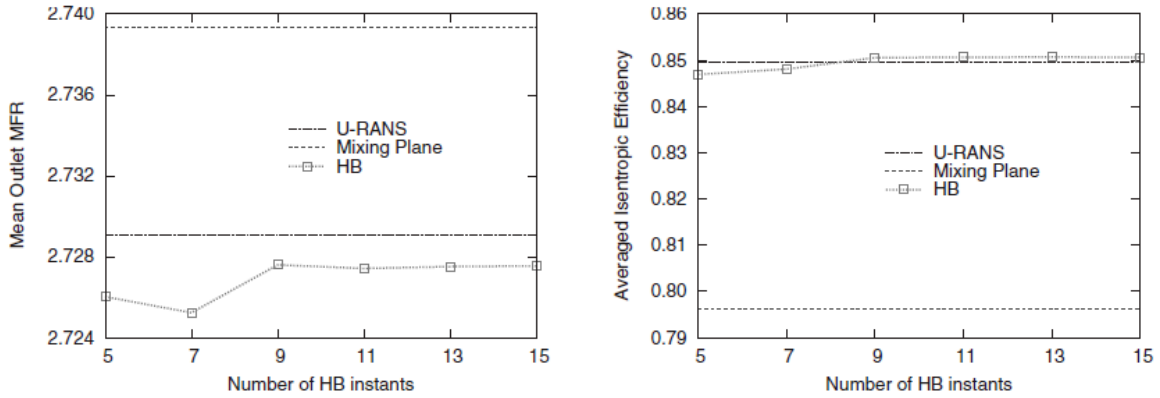

Figure 2.3: URANS and HB comparison: time-averaged mass flow rate and efficiency [4].

Figure 2.4 shows the entropy at midspan for the URANS and HB solutions. Generally, it is clear that the HB simulation struggles to compute the wake pattern once it passed the interface between both rows. Especially at five time instances, the performance is rather lacking due to poor time sampling, the HB method source term and the nonmatching mesh interface. Still, the wakes seem to be at the right position and correctly aligned, suggesting that the rotor-stator interactions are well captured. Increasing the amount of time instances further enhances the solution. A similar trend is observed for the pressure distributions at mid span. At five time instants, the pattern looks rather noisy and does not match the URANS results well, but increasing the number of time instances N makes for a good approximation of the time-accurate solution.

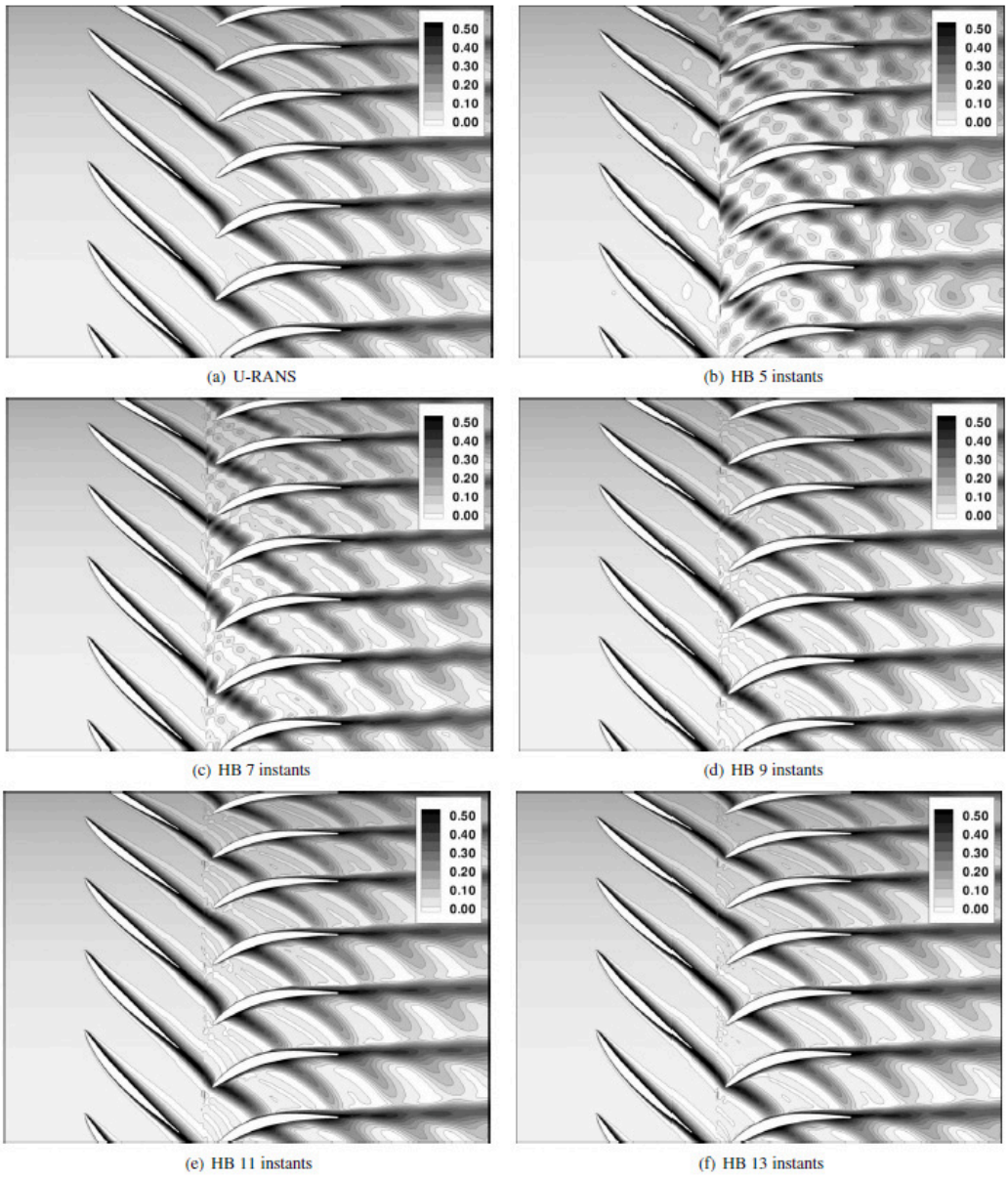

Figure 2.4: Entropy at midspan [4].

Sicot states that performing a harmonic balance simulation using nine time instances generally proves to give results that are very close to time-accurate flow solution, while it is five times faster to perform. Eleven time instances almost perfectly match the URANS results in every regard, while the simulation is still four times faster [4].

The test case of Sicot is a three-dimensional one, which does introduce additional complexities into the harmonic balance implementation. Matching the mesh and applying the (periodic) boundary conditions is a real challenge in three-dimensions. The observed problems with non matching mesh interfaces and modeling might partly be attributed to this complexity. Additionally, Sicot describes that due to the three-dimensional flow phenomenon of tip leakage vortices, the domain is easily corrupted and fails to converge. Therefore, additional initialization is needed.

Gopinath [2] also performed a three-dimensional harmonic balance implementation, and compared the results and performance with a time-accurate solver. Flow features are found to be well captured, while order of magnitude savings in CPU times are registered compared to time-accurate unsteady solving methods.

Another trade-off between a time-accurate and a HB flow solver is found in a recent research by Rubino [15]. Both solution methods are applied to a two-dimensional supersonic cascade in an organic Rankine cycle under a time-varying inlet pressure. Here too, results show that the harmonic balance method is able to approach the time-accurate unsteady solution very well, while being around an order of magnitude faster.

Finally, Huang [10] also compared the computational time of the harmonic balance method (though with only one harmonic) against a time-accurate solution method and found the HB solution to take less than a sixth of the time of the time-accurate solution.

2.3. Shape Optimization

2.3.1. Overview of Shape Optimization Methods

With the evolution in computational power and applications over the past decades, computational fluid dynamics and related methods such as computational structure mechanics have become not just a tool for performance analysis but an integral part of the design process. The physical behavior of a to-be-optimized item - be it aerodynamically, structurally or other - is governed by an extensive set of parameters. Many of these parameters are strongly related, making it hard to determine the effect of changing a certain parameter on the overall behavior. Computational optimization tools can help in this task: their algorithms are written in a way that performance of a design is maximized by modifying its parameters.

An optimization generally can be formulated as follows [22]:

Minimize:
$$J(\mathbf{U}(\boldsymbol{\alpha}), \mathbf{X}(\boldsymbol{\alpha})) \tag{2.19}$$

Subject to:
$$g(\boldsymbol{\alpha}) \leq 0 \tag{2.20}$$
$$h(\boldsymbol{\alpha}) = 0 \tag{2.21}$$
$$\alpha_i^l \leq \alpha \leq \alpha_i^u \tag{2.22}$$

Where:
$$\boldsymbol{\alpha} = [\alpha_1, \alpha_2, ..., \alpha_n] \tag{2.23}$$

In this formulation, $\boldsymbol{\alpha}$ is the vector of design parameters. These are the variables that define the design and that are modified in the optimization in order to improve that certain design. In the case of

aerodynamic design optimization in turbomachinery, these are for example the coefficients that define the shape of the airfoil on a certain blade. J is the objective function: this is the quantity to be either maximized or minimized. An example is the minimization of the total pressure difference over a stage. In every iteration of an optimization algorithm, the design vector is altered, and the corresponding objective function value is evaluated. This process is repeated until a sufficient minimum is reached. The function evaluation in the case of aerodynamic design optimization is the primal flow solver. The objective function is dependent on the flow variables **U** and geometry **X**. Equations 2.20, 2.21 and 2.22 represent inequality constraints, equality constraints and limits to the design variables. A common alternative to constraints is introducing penalties within the objective function. A configuration with an undesired characteristic will then worsen the objective function value. A weight can determine the impact of that certain characteristic.

The improvement of flow solution methods discussed in the previous chapter clearly has a severe effect on the computational time of the entire optimization process. The shear number of flow evaluations additionally increases the effect of the efficiency of the flow solver. Along with shorter evaluation times, a no less important improvement is to be made in decreasing the number of evaluations needed by the optimization algorithm to find the required minimum. This aspect is governed by the optimization algorithm itself.

Optimization methods are generally subdivided into gradient-free, also called zero order methods, and gradient-based higher order methods. Zero order methods only use the objective function value in order to perform their search for an optimum. The most basic derivative-free method is the random search approach. In this method, random design vectors are selected and their respective objective function values are determined. The design vector resulting in the smallest objective function is selected as the optimum. It is clear that this method is extremely inefficient. It requires a lot of evaluations and then still the method is rather hit-and-miss. The random walk method scores similarly in terms of randomness. From a certain set of design variables, a random search direction and step size is used to find the next to-be-evaluated design vector. Slightly more advanced is the simulated annealing method. In this method, based on annealing in metals, a neighboring state is considered. Probabilistically, the optimizer opts whether or not to go to the new state of the design vector. This process is repeated until the wanted 'low energy state' is achieved. A completely different class of zero order methods are evolutionary algorithms. These algorithms are similar in idea to biological evolution and natural selection as described by Darwin [22]. Genetic algorithms (GA), one type of evolutionary algorithms, start from a random selection of design vectors. They are evaluated after which the design variables of the 'fittest' pairs are used to form a second generation of design vectors. Evolutionary algorithms are generally more computationally demanding, as they require evaluating the objective function value of all individuals at every iteration. How the 'parent' design vectors are selected and how the variables are combined and passed on to the next generation of design variable vectors has a severe effect on the result and behavior of the optimization, and many different methods have been developed and evaluated over the course of time. Though better than the very basic random methods, the shear number of evaluations needed to reach an acceptable minimum means that evolutionary algorithms are not useful for the scope of this project.

Gradient based optimization methods base their search not only on the objective function value, but also on the derivative of the objective function with respect to the design variables. That way, they are able to more efficiently find a search direction, and get to an optimum in lower amounts of evaluations. However, the need to evaluate the gradient (and sometimes higher derivatives as well) can introduce a lot of additional computational cost. The most basic gradient based optimization method is the steepest descent method. As the gradient is an indicator of the direction in which the objective function is increasing/decreasing the most, the gradient is used as the search direction. The weight assigned to that search vector, determining the step size, can be chosen in a number of different ways.

A second method of finding a step direction and size is the so-called Newton method. Here, the step is determined with a combination of the gradient and the Hessian: the matrix of second-order partial derivatives. Given that these second-order derivatives are to be determined on top of the gradient, this method - while effective at finding the optimum - is computationally demanding. Quasi-Newton methods can be used to approach the Hessian. There is one thing that can be said for all these methods: an efficient way of calculating the gradient is clearly of paramount importance for the overall efficiency of the algorithm. One, rather simple, method to determine the gradient in a certain design point is using the finite difference method. The objective function value is then evaluated at a certain design point, as well as for a slightly perturbed version of the design vector. An approximation of the gradient can then be found as follows [22]:

$$\forall i \in \{1, \dots, n\} : \quad \frac{\partial J}{\partial \alpha_i} \approx \frac{J(\boldsymbol{\alpha} + h\,\overrightarrow{\mathbf{e_i}}) - J(\boldsymbol{\alpha})}{h} \tag{2.24}$$

A second (or higher) order accurate approximation can be selected in order to more accurately determine the gradient, however such a choice would also mean an additional increase in evaluations and so in computational time. Clearly, for design problems with a large amount of design variables, the finite difference method method quickly becomes too computationally demanding. The complex variable method is not very different from the finite difference method. It uses a Taylor series expansion of the objective function and makes use of an imaginary perturbation instead of a physical one. Algorithmic differentiation (AD) is another way of obtaining a gradient. This algorithm makes use of the fact that in most computations, a number of very basic operations are being performed. Along the way, their derivatives are determined. The chain rule can then be applied in order to obtain larger derivatives, and finally determine a gradient. In essence, this technique enables one to determine these derivatives with next to no additional computational cost. There are two distinct modes within algorithmic differentiation: forward accumulation and reverse accumulation. Both modes have got their advantages and disadvantages. While in forward mode, the more computations are to be performed, the backward mode comes with larger memory requirements. Finally, there is the adjoint method, which will be one of the focus points of this research project. This method, which comes from control theory, enables calculating the objective function gradient by solving the flow governing equations and the adjoint equations [22–24]. The solution of the adjoint equations is similar in computational time to the solution of the flow governing equations. Additionally, the cost for solving these adjoint equations is independent of the number of design variables. This makes it extra attractive in problems governed by many different variables, such as turbomachinery blade design.

2.3.2. Adjoint Optimization

As explained in the previous introductory words on adjoint optimization, the adjoint method represents a way to determine the gradient of the objective function value with respect to the corresponding design variables. It was pioneered in the area of fluid dynamics by Pirronneau [25] and Jameson [26]. There are two main types of adjoint formulations that can be distinguished: continuous and discrete adjoint methods. In the continuous adjoint method, adjoint equations are analytically derived from the partial differential equation (PDE) form of the flow equations and then discretized in order to compute the sensitivities [20, 27]. When using the discrete adjoint method, the flow equations are first discretized, after which the adjoint equations are derived. Generally, the discrete adjoint method delivers more accurate objective function sensitivities, though both methods have been used in aerodynamic turbomachinery optimization and result predominantly in the same solutions in case of a properly dense mesh [27]. Discrete adjoint codes are harder to develop and usually require more memory and computational time [3]. The method makes use of the chain rule to compute the derivative of the objective function J with re-

spect to the design variables $\boldsymbol{\alpha}$ by splitting the derivative into derivatives that are more easily resolved. The objective function is a function of the design variables and the flow parameters.

$$J = J(\boldsymbol{\alpha}, \mathbf{U}(\boldsymbol{\alpha})) \tag{2.25}$$

As a result, the derivative can be written as follows:

$$\frac{dJ}{d\boldsymbol{\alpha}} = \frac{\partial J}{\partial \mathbf{U}} \frac{d\mathbf{U}}{d\boldsymbol{\alpha}} + \frac{\partial \mathbf{U}}{\partial \boldsymbol{\alpha}} \tag{2.26}$$

Now, $\frac{dJ}{d\boldsymbol{\alpha}}$ can be determined by evaluating three other derivatives. The derivative of the flow conservation variables with respect to the design vector is still a difficult evaluation if to be done directly. In order to reduce computational cost, a different way is implemented. A state equation $\mathbf{R}$ is introduced:

$$\mathbf{R}(\boldsymbol{\alpha}, \mathbf{U}(\boldsymbol{\alpha})) = 0 \tag{2.27}$$

Its derivative with respect to the design variables results in the following expression:

$$\frac{\partial \mathbf{R}}{\partial \boldsymbol{\alpha}} + \frac{\partial \mathbf{R}}{\partial \mathbf{U}} \frac{d\mathbf{U}}{d\boldsymbol{\alpha}} = 0 \tag{2.28}$$

Equation 2.28 can be rewritten as follows:

$$\frac{d\mathbf{U}}{d\boldsymbol{\alpha}} = -\left[\frac{\partial \mathbf{R}}{\partial \mathbf{U}}\right]^{-1} \frac{\partial \mathbf{R}}{\partial \boldsymbol{\alpha}} \tag{2.29}$$

Now, merging equations 2.26 and 2.28, an expression is obtained without the derivative of the flow conservation variables with respect to the design vector. The result looks as follows:

$$\frac{dJ}{d\boldsymbol{\alpha}} = -\left[\frac{\partial J}{\partial \mathbf{U}}\left(\frac{\partial \mathbf{R}}{\partial \mathbf{U}}\right)^{-1}\right]\frac{\partial \mathbf{R}}{\partial \boldsymbol{\alpha}} + \frac{\partial J}{\partial \boldsymbol{\alpha}} \tag{2.30}$$

or:

$$\frac{dJ}{d\boldsymbol{\alpha}} = \lambda^T \frac{\partial \mathbf{R}}{\partial \boldsymbol{\alpha}} + \frac{\partial J}{\partial \boldsymbol{\alpha}} \tag{2.31}$$

where λ is the adjoint variable, satisfying the adjoint equation:

$$\left[\frac{\partial \mathbf{R}}{\partial \mathbf{U}}\right]^T \lambda = -\left[\frac{\partial J}{\partial \mathbf{U}}\right]^T \tag{2.32}$$

The state or constraint $\mathbf{R}$ as described here holds for steady-state flow. In an unsteady harmonic balance environment, based on the harmonic balance method derivation in section 2.2, the adjoint equations become:

$$\left[\frac{\partial J}{\partial \mathbf{U_n}}\right]^T + \sum_{k=0}^{N-1} \lambda_k \left[\frac{\partial \mathbf{R}}{\partial \mathbf{U}}\right]^T = \lambda_n \tag{2.33}$$

The required sensitivity gradient can be determined as follows:

$$\frac{dJ}{d\boldsymbol{\alpha}} = \frac{\partial J}{\partial \boldsymbol{\alpha}} + \sum_{n=0}^{N-1} \lambda_n^T \frac{\partial J_n}{\partial \alpha_n} \tag{2.34}$$

The required derivatives are generally computed using the reverse Algorithmic Differentiation mode.

Computational Performance

The accuracy of an adjoint gradient determination method is often evaluated by performing a comparison to the sensitivities obtained using a finite difference method. This verification has been performed many times, in many different researches across many different design problems [20]. It is clear that the agreement between adjoint and finite difference sensitivities is mostly excellent. Rubino [7] finds a very good agreement between gradients obtained using AD and FD. Huang also shows that the convergence history of the adjoint solver is similar in rate as the primal CFD solver. Adjoint optimizations have been performed numerous times in a turbomachinery context, verifying their working. An gradient validation will also be part of the shape optimization process in this research project.

Shape Parametrization

The design case of interest for this research is the shape optimization in 2D turbine blades. In the optimization definition that has been discussed before, the shape is then to be represented by a parameterized airfoil shape. It is important for a parameterization method to allow for consistent, effective and efficient modelling [28]. Parameters are to be able to capture the shape features that are to be represented. Finally, changing the values of the variables should result in a physical, usable model.

Parameterization can be done in many different ways. Firstly, individual mesh points can be used to define the foil shape. In that case, the design vector is made up of the y-coordinates of the grid points along the chord. An advantage of this method is the ability to change the shape on a very small scale and in a very localized way. The result, however, is generally a very large amount of design variables. Even though the performance of adjoint optimization methods is next to independent on the number of design variables, this is not exactly elegant. A more important drawback is that changing a separate coordinate does not really have a physical meaning, in the sense that it just creates a discrete bump on the surface. Therefore, additional smoothening is often to be performed.

Another way of parameterizing blade shapes is by mathematical definitions of curves. An example of this can be seen in the way NACA 4-digit series airfoils are constructed. They are defined by a function that describes the camber distribution and another that describes the thickness. Following the same principle, a turbomachinery blade shape can be described by a curve, represented by a select number parameters. One method is the so-called class shape function transformation (CST), which represents a certain shape as a variation of a set shape function. A general class function can be defined for an airfoil. By multiplying it with a Bernstein polynomial, that class function can be shaped in a certain way. The scaling factors of the Bernstein polynomials are then the parameters for the design vector in the optimization process. While CST methods are consistent, deliver a smooth and physical airfoil shape,

and do not require a large amount of parameters, they can only model very global and large changes in shape. In case more local shape changes are to be applied at a certain location, the CST method fails to deliver.

The Hicks-Henne function method is often used in (turbomachinery) blade shape optimization [3, 16, 20, 29]. Again, the shape is parameterized with a set of smooth functions. Just as with the CST method, only a few functions are needed to model the shape. Bumps are introduces, with parameters determining their magnitude, maximum point and width. This means that, unlike with the class shape function transformation, more local deformations can be applied at specific locations on the airfoil, while unlike with the grid perturbation method, the shape still remains smooth.

It is clear that CST coefficients are efficient at changing the overall blade shape, but rather terrible at modeling smaller and more localized perturbations of the blade shape. Hicks-Henne coefficients prove a better method to do so, but are still lacking in some ways. Blades in a turbomachinery context, given the type and velocity of flow, clearly exhibit regions of extreme sensitivities, such as the leading edge, shock surface and blade tip [30]. Small perturbations of the blade surface might then yield significant improvements in overall efficiently, by locally managing the shock location and size, the tip leakage vortex and so on.

Another way of parameterizing and deforming blade shapes is free-form deformation (FFD). This method is the one of choice for the purpose of this thesis project. Free-form deformation is a commonly used method in which the blade surface is enclosed in a box or grid of which the control points can be moved. The surface inside is stretched and deformed accordingly. FFD is implemented inside the *SU2* software suite and has been used extensively to optimize two-dimensional turbine blades [31]. A disadvantage of free-form deformation is that while options are implemented to ensure continuous surfaces, unfeasible geometries can still be generated. Attention is required with regards to scaling factors on design sensitivities and on constraints in order to manage this issue.

2.4. SU2

The software that will be used throughout this research project is the *SU2* analysis and optimization suite. This open-source, C++ based software suite has its origin at Stanford University, California, United States, and was originally developed to solve complex, multi-physics analyses and optimization tasks using arbitrary unstructured meshes [32]. It proved to be readily extensible for solving partial differential equations. The main focus of *SU2* lies in RANS based simulations of compressible, turbulent flows, and it is mostly used for applications in the field mechanical and aerospace engineering. It provides a platform capable of performing shape optimizations based on adjoint gradient determination.

One major asset of the *SU2* environment is the way it is able to integrate different functions in order to straightforwardly perform coupled multi-physics analysis and optimization. In other software, such coupled applications are often a major challenge, as not all required capabilities might be available within the same software environment, or as their integration might be very complicated. *SU2* was set up with this goal in mind. The result is a universal platform consisting of several different modules that can be made to interact relatively easily. Flow solvers, adjoint solvers, optimizers, mesh and shape deformation and parameterization and more can be combined within this same software environment.

Another aspect that stands out about *SU2* is the fact that it is an open-source package, which comes with a plethora of advantages. Mainly, it enables developers worldwide to not only use and change the code for their specific applications or research, but to then also share those implementations with the rest of the user base. The result is a software that is constantly being improved and added to. This

manifests itself both in terms of improvement of existing capability and completely new functionality. As a user of the *SU2* suite, this also makes that this master thesis research has the opportunity to be a part of this community-built platform of innovation. The software being open-source also means some control has to be exerted over it, in order to keep it structured, correct and well-integrated. For this reason, changes are monitored, release versions are controlled and documentation is maintained.

Maybe the largest motivator for using *SU2* for the purpose of this master thesis project is the role it plays within the turbomachinery group at Delft University of Technology. The research group is actively engaged in contributing to *SU2* and is one of the main drivers behind *SU2*'s development. This enables the author of this thesis to share knowledge among colleagues, both in order to contribute and to learn.

SU2 is not the only (open-source) flow solving software on the market. Several other, well-established software environments exist that are similar in idea to *SU2* and that share some functionality. Apart from its modularity and multifunction integration, there are several reasons to select *SU2* over its competitors.

OpenFOAM is a very widely used open-source flow solving software. It is also a C++ based environment, and shares a few advantages with *SU2*. It is also probably the most solid open-source competitor. Because of its broad and diverse user base and the open-source aspect, *OpenFOAM* is in constant evolution. It also offers a rather complete environment, in that it enables parallel mesh generation, postprocessing and similar extended functionality. For the scope of this project however, *SU2* offers significant advantages over *OpenFOAM*. Firstly, the native support for gradient-based optimization, and adjoint optimization in particular is an important part of the functionality of *SU2*, and sets it apart. Moreover, while *OpenFOAM* is very widely used, also outside of the field of aerospace engineering, *SU2* is quite aerospace focused, and is used and adapted often for turbomachinery applications. *SU2* is also better with compressible flow. Another important advantage of the Stanford-born code is the rate and ease at which new capabilities can be implemented. *OpenFOAM* might be a touch more matured, *SU2* is developing fast and overall very much more in line with the functionalities required within the scope of this project. *Ansys CFX* is very well established among commercial CFD software, and equally so within the field of turbomachinery. While it is accurate, complete and really well suited for turbomachinery applications, there are still aspects in which *SU2* has the edge. First of all, again, the degree to which gradient based optimization can be performed within *SU2* is just not there in *CFX*. Secondly, *Ansys CFX* is not an open-source code. While that makes it well controlled, clean and robust, it means that it is harder to adapt to specific requirements for a certain research project. Finally, Keep [33] has performed a comparison between *SU2* and *CFX* for an organic Rankine cycle application, and found that there was close agreement between the results obtained by both solvers. While this project will not be focused on organic Rankine cycles, the verification does show the maturity and capabilities of *SU2*.

2.5. Non-ideal Compressible Flow

An ever increasing amount of research in the field of turbomachinery is focused towards unconventional and exotic working fluids. These can serve applications in geothermal, solar and waste heat power - among others - which are characterized by relatively smaller thermal reservoirs at lower temperatures [34, 35]. Supercritical carbon dioxide (sCO_2) and organic Rankine cycle (ORC) machines are good examples of such innovations. These working fluids are often more complicated in molecular structure and/or operate in more critical or unconventional thermodynamic regimes. Accurate ways of simulating the flow behavior is crucial to the design and optimization of these types of turbomachines. As in any type of turbomachinery, CFD plays a major role in performing that action. In more conventional air-driven turbomachines, the ideal gas law is often assumed valid. The equations in 2.35 show the equations of state of the polytropic ideal gas model as present in *SU2*. As the name suggests, the gas

is assumed in an ideal state. While this assumption holds reasonably well in a range of operating conditions, the equations fail to adequately model thermodynamic states of fluids at more extreme pressures and temperatures.

$$\begin{cases} p(T,v) = \frac{R\,T}{v} \\ e(T) = c_v\,T \\ s(T,v) = c_v\ \ln(T) + R\ \ln(v) \\ c_v = \frac{1}{\gamma - 1}\,R \end{cases} \tag{2.35}$$

This way of accounting for the thermodynamic state of the working fluid is straightforward, computationally inexpensive and holds up well in a broad range of pressures and temperatures. These ideal conditions do not apply to both the fluid characteristics and thermodynamic operating state of machines based on ORC and sCO_2. These types of turbomachinery are characterized by compressibility, strong thermo-physical fluid property gradients and other non-ideal flow effects [36]. As a result, design optimization processes may produce very different - and better - results when accounting for these effects.

Another important part of the flow solver, especially given the interest in different and exotic working fluids, is the equation of state. *SU2* comes with a number of different gas models, including ideal gas, Van der Waals and Peng-Robinson. The polytropic ideal gas and Van der Waals equation of state are used, depending on the case and as assigned in chapter 4.

Non-ideal compressible fluid dynamic (NICFD) equations, unlike ideal gas equations of state are often based on a (semi-)empirical approach, making them challenging to implement. Research by Nederstigt [35] has focused on setting up such non-ideal sets of equations. The equations of state of the polytropic Van der Waals fluid model present in *SU2* and used for the non-ideal flow simulations have additional relations to account for the non-ideal behavior of fluids. The coefficients a and b are introduced to fulfill that purpose. Their physical meaning is shown in the equations 2.37. a represents the average attraction between particles, while b is the space occupied by the molecules in the fluid. Critical temperature and pressure are required as inputs in *SU2* along with the acentric factor.

$$\begin{cases} p(T,v) = \frac{R\,T}{v-b} - \frac{a}{v^2} \\ e(T,v) = c_v\,T - \frac{a}{v} \\ s(T,v) = c_v\ \ln(T) + R\ \ln(v-b) \end{cases} \tag{2.36}$$

$$\begin{cases} a = \frac{27}{64}\ \frac{R^2\,T_{cr}^2}{P_{cr}} \\ b = \frac{1}{8}\ \frac{R\,T_{cr}}{P_{cr}} \end{cases} \tag{2.37}$$

Important in Nederstigt's work is the introduction of the isentropic pressure-volume exponent γ_{Pv} as a replacement for the specific heat ratio γ. It can be defined as

$$\gamma_{Pv} = -\frac{v}{P}\frac{c_p}{c_v}\left.\frac{\partial P}{\partial v}\right|_T \tag{2.38}$$

In an ideal state, γ_{Pv} is equal to the specific heat ratio γ. Likewise, γ_{Pv} can be used to identify a certain condition as non-ideal. γ_{Pv} is either lower or higher than γ close to the critical point. Research finds large deviations in Mach number along the expansion for these cases [36]. Where γ_{Pv} is larger than γ, the average Mach number is found to be higher than in ideal conditions for the same volumetric flow ratio.

The opposite holds when $\gamma_{Pv} < \gamma$. Giuffré's research covers hexamethyldisiloxane (MM), representing ORC applications and supercritical CO_2. MM looks to be the most interesting for further examination in this research for two main reasons. Firstly, the variation in performance trends is found to be larger for MM [36]. Secondly, due to the nature of MM's phase diagram, the to be tested cases do not excurse in the two-phase region, as is often the case for sCO_2. Giuffré finds efficiency differences of up to 2 percentage points between simulations including and excluding non-ideal flow effects. CFD results confirm the increased Mach number in $\gamma_{Pv} > \gamma$ cases. The expected increase in shock and other unsteady effects suggests that this case would be most interesting for the HB versus steady-state comparison of this master thesis research.

Additionally, research shows the volumetric flow ratio, also known as the total-to-static density ratio, R_v to be a more suited similarity parameter than the expansion ratio β [36]. The two are related as $R_v = \beta^{1/\gamma}$. This rather novel discovery will be applied to the work in this thesis research.

3

Methodology

This chapter sets out the methodology that is followed throughout the research process. The reader is provided with an in-depth description of the different steps or work packages that together make up the research.

Reiterating the research objectives described in chapter 1, the goal of this thesis work is to obtain best practices that can provide indications on whether to employ an adjoint-based HB method for the fluid-dynamic optimization of turbine stages. Figure 3.1 shows the main steps to be undertaken in the execution of this research. These are the work packages that together comprise the thesis work. The research is based on four core topics, visualized by the blue steps in the flow diagram. The other work packages crucial to achieving and linking the experimental flow are shown by means of the white boxes. The flow diagram also includes information on the software used at every step of the technical approach.

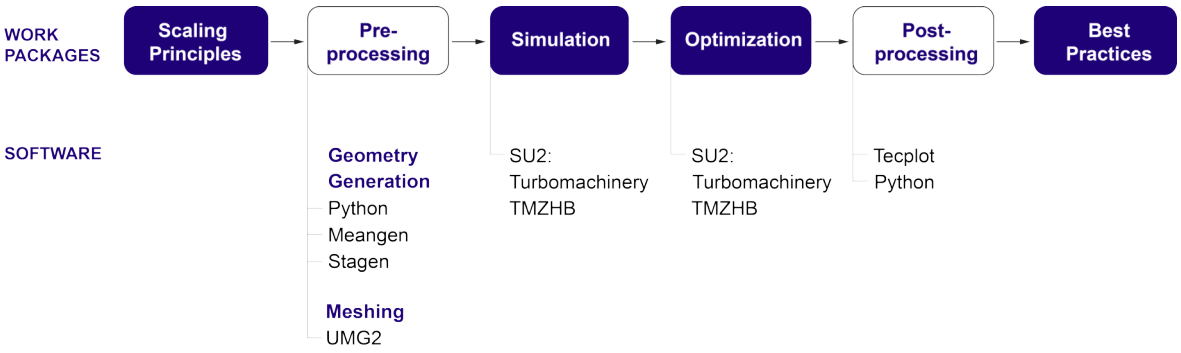

Figure 3.1: Experimental flow diagram.

The first fundamental step is to establish the scaling principles. A set of most relevant design parameters is selected as similarity parameters by means of a scaling analysis. The classical similarity relations are extended to account for non-ideal fluid dynamics. The validity of the scaling parameters is to be confirmed by the research. Certain similarity parameters will be varied in order to assess their effect on simulation and optimization results, and on the differences between results from steady-state and HB flow models in particular. The scaling principles govern the input parameters for the to be evaluated 2D turbine stage geometries. From there, a set of geometries and their corresponding meshes can be set up. Constructing the geometries is performed using the *Meangen* and *Stagen* software tools. The

open source and in-house *UMG2* software is used for creating the respective meshes.

Considering the large computational time associated with full optimizations, a set of simulations is first performed on all of the different design variations. The resulting data set allows to investigate the effect of each variation on the results of the steady-state and harmonic balance solvers. Subsequently, a second and smaller set of adjoint blade shape optimizations is carried out on a selected number of cases. These aim to investigate the efficiency gain in the optimized stage obtained using one solver over the other. Additionally, the optimizations are crucial to establishing whether the same behavior is found as in the corresponding simulations. In other words, the optimizations are a way of verifying whether valid best practices for optimization can be set up based on the results from the primal flow solver. These simulations and shape optimizations are performed in the *SU2* open source CFD environment. The steady-state model implemented in the *turbomachinery* and *turbo_ffd* branches of *SU2*, and the harmonic balance unsteady flow solver in feature *TMZHB_temp* are used.

The next building block of the aforementioned work flow is processing and interpretation of the results. In this step, the simulated and optimized blade shapes and the efficiencies obtained from the different optimizations are assessed, both individually and in relation to one another. Raw numbers are transformed into observations and trends. Physical explanations are to be found for these results.

Finally, the observations resulting from the simulations and optimizations can be translated into design guidelines or best practices for future 2D turbomachinery design. More specifically, the trends identified within the flow and solver behavior under varying scaling parameters can help in selecting the most appropriate flow solution method for a 2D shape optimization. Validation and verification are important aspects of any research work, and they are implemented at various points along the experimental process. The implementations include mesh convergence studies, model validation and verification, adjoint gradient validation and validation of the numerical outcome of the optimizations.

Each of these work packages is discussed in further detail in the following subsections.

3.1. Similarity and Scaling Principles

Similarity laws are crucial in setting up representative test cases and comparing the simulation results on equal footing. The accompanying similarity parameters are obtained by performing a dimensional analysis. In the process, a set of variables that represents the physical properties of a turbine stage is reduced to a smaller number of nondimensional groups. The term scaling principles refers to the main property of these nondimensional parameters. Two turbine stages, even though physically different in size or properties, yield identical performance when they share the same similarity parameters. Buckingham's theorem states that from a set of n parameters governing a certain characteristic, a set of $p = n - k$ dimensionless parameters can be determined that still represents the initial dependency. k stands for the number of base physical dimensions. Four aspects need to be maintained in order to obtain full similarity. These are

- Geometric similarity (geometrical quantities)
- Dynamic similarity (Reynolds and Mach numbers)
- Kinematic similarity (velocity triangles, resulting from flow coefficient, work coefficient and degree of reaction)
- Thermodynamic similarity (thermodynamic conditions)

In the case of this thesis, the physical variables governing the efficiency of a turbine are shown in equation 3.1.

$$\eta = f(\underbrace{\phi, \psi, r^*,}_{\text{flow -, work coeff., degree of reaction}} \underbrace{\rho_{t1}, T_{t1},}_{\text{tot. inlet density and temperature}} \underbrace{\rho_2,}_{\text{static outlet density}} \underbrace{\gamma, R, \mu,}_{\text{specific heat ratio, gas constant, viscosity}} \underbrace{U,}_{\text{rotor transverse velocity}} \underbrace{\mathbf{s}}_{\text{geometrical characteristics}}) \tag{3.1}$$

The vector of geometrical characteristics contains the blade chord, span, pitch etc. The base physical dimensions involved are mass, length, time and temperature. Buckingham's π theorem can then be used to determine the nondimensional parameters binding the larger set of parameters and impacting the efficiency of the stage. The eight resulting parameters are the following:

$$\eta = f(\phi, \psi, r^*, R_v, \gamma, Re_t, \boldsymbol{\sigma}) \tag{3.2}$$

Where subscript t represents the transverse (rotational) flow direction, and σ represents the vector of dimensionless geometric characteristics. For non-ideal compressible flows, this equation becomes

$$\eta = f(\phi, \psi, r^*, R_v, \gamma_{Pv}, Re_t, \boldsymbol{\sigma}) \tag{3.3}$$

The set of similarity parameters is close to identical to the one derived in reference work [21]. One crucial difference is that the volumetric flow ratio has been introduced instead of the expansion ratio, as suggested by Giuffré [36]. Test cases within this research will be set up such that only one similarity parameter is varied at a time, such as to make a parametric study which is both physically sound and formally correct, namely where all independent variables are actually not related to each other. The dimensionless parameters that are considered in detail are ϕ, ψ, R_v and γ or γ_{Pv}.

3.2. Geometry Generation

All test cases in this research deal with two-dimensional turbine stages consisting of two blade rows: a stator row followed by a rotor row. Unlike in real turbine stages, which often have less stator than rotor blades, all cascades in this research have an equal stator and rotor pitch. This is due to the limitations tied to periodic phase boundary conditions in *SU2*. Blade shapes are generated with the *Meangen* and *Stagen* tools. These are part of the *Multall* software suite by Prof. J. Denton [37]. The *Meangen* - *Stagen* geometry generator is selected for this project as it requires only a few relatively basic inputs to generate a stage geometry. This allows for a very conceptual and fast design process, obtaining perfectly adequate blade shapes straight from the set of base test case characteristics. The inputs required for the geometry generation in *Meangen* are summarized in table 3.1. *Stagen* outputs data files containing the coordinates of the generated blades are obtained at the end of the process.

The first set of inputs to *Meangen* are the stage flow coefficient ϕ, the work coefficient ψ and degree of reaction r^*. These three kinematic similarity parameters are at the core of the architecture and performance of a given turbine stage. The flow coefficient is an indicator of the flow capacity of the stage, and is proportional to the volumetric flow rate of the stage. It is defined as the ratio between the meridional velocity - axial in case of the axial turbines relevant to this work - and the rotational speed of the rotor row:

$$\phi = \frac{V_{ax}}{U} \tag{3.4}$$

The load or work coefficient ψ is a measure of the work capacity of the stage. A higher work coefficient represents a higher stage with a higher specific work and thus a higher blade loading. The load coefficient is proportional to the specific work and inversely proportional to the square of the rotational speed, as shown below

$$\psi = \frac{w}{U^2} \tag{3.5}$$

The degree of reaction r^* represents the static expansion of the flow throughout the rotor, and is defined as

$$r^* = \frac{\Delta h_r}{w} \tag{3.6}$$

The process of selecting these parameters - and the entire set of case studies by extension - is discussed in detail in chapter 4. On top of these nondimensional parameters, additional stage characteristics are required as inputs for *Meangen*. For this thesis, a meanline design program is developed in *Python* which provides these final inputs required by the geometry generator software. Additionally, it acts as a verification tool for the meanline, conceptual design that takes place within *Meangen* and *Stagen*.

Table 3.1: *Meangen* input parameters.

Physical quantity	Input variable
Nondimensional stage parameters	r^*, ϕ, ψ
Fluid thermodynamic properties	R, γ
Stage inlet boundary conditions	$P_{t_{in}}, T_{t_{in}}$
Rotor rotational speed	Ω
Mass Flow	$\dot{m}$
Expansion ratio	β
Blade chord	b
Solidity	σ
Blade thickness	t

The input parameters for all different geometries in this research are determined in the same way. The flow and work coefficients are what determine the test cases and are therefore evidently different for each different geometry. The degree of reaction is kept constant for all test cases. The characteristics tied to the working fluids, the inlet conditions, the volumetric flow ratio, mean radius, chord and mass flow remain unchanged across all geometries as well. The rotational speed varies in order to comply with the set enthalpy change (*dh*) and work coefficient of the stage, following equation 3.7. The enthalpy drop over the stage is determined from the temperature difference, which itself can be derived from the expansion ratio, as shown in the equations below.

$$U = \sqrt{\frac{dh}{\psi}} \tag{3.7}$$

$$dh = c_p\ (T_{t1} - T_3) \tag{3.8}$$

$$T_3 = \frac{T_{t1}}{\beta^{\frac{\gamma-1}{\gamma}}} \tag{3.9}$$

As touched upon in chapter 2 and explained in more detail later in this chapter, not the expansion ratio but the volumetric flow ratio will act as a governing parameter. The expansion ratio β can be deduced from the volumetric flow ratio R_v with the help of the following isentropic relation

$$\beta = R_v^{\gamma} \tag{3.10}$$

Mean radius and chord length are kept constant over the different stage geometries. The resulting variation in aspect ratio is deemed insignificant given the two-dimensional nature of the simulations. Solidity is determined using the Zweifel loading criterion, which relies on the velocity triangles, which in their turn are determined from the flow coefficient, work coefficient and degree of reaction. The equations resulting from Zweifels criterion and used to determine the solidity in both stator and rotor are shown below. The blade pitch follows from multiplying the solidity with the blade chord.

$$\sigma_s = \frac{0.8}{2\ \cos^2\alpha_2\ (\tan\alpha_2 - \tan\alpha_1)} \tag{3.11}$$

$$\sigma_r = \frac{0.8}{2\ \cos^2\beta_3\ (\tan\beta_2 - \tan\beta_3)} \tag{3.12}$$

In these equations, α and β represent the absolute and relative flow angles, respectively. Stations 1, 2 and 3 indicate the stator inlet, stator outlet and rotor outlet locations. Finally, the blade thickness is increased with work coefficient in line with reference material.

3.3. Meshing

The in-house 2D meshing tool *UMG2* is used to generate the meshes to be used in flow solving and optimization in *SU2*. *UMG2* was first introduced by Ghidoni as a fully automatic anisotropic mesh generation method for domains of arbitrary shape [38]. *UMG2* is an unstructured mesh generator at its core, but has an implemented feature that allows for structured meshes in the boundary layer region of the blade. It can directly output meshes in *.su2* format, significantly simplifying the process compared to other meshing software. *UMG2* requires several sets of inputs and settings in order to fulfill its role.

The first and main element of the mesh is the geometry of the stage. *UMG2*'s geometry input file is to contain coordinates of all blade walls and in-, outflow and periodic boundaries in the mesh domain. The blade shapes are defined in the data files resulting from *Stagen*. This data file carries the geometry information in the form of two sets of two times 200 x-y coordinate points. Each set represents the suction and pressure side of the stator or rotor blade. The in- and outflow boundaries are set to be located one full blade chord length (0.0167 m) before and after the stator leading edge and rotor trailing edge, respectively. Periodic boundaries are set up in the form of the mean blade camber lines plus and minus half the blade pitch. This way, the full annulus can be reduced to a single-blade mesh. The periodic boundaries allow for a larger flow field to be reconstructed, while significantly reducing computational

time compared to a full annulus simulation. A second *UMG2* input file defines what physical boundary conditions are to be applied to each of the defined geometrical features. Inflow, outflow, periodic boundaries and no-slip walls are assigned to their respective coordinate series defined in the geometry file.

The options concerning element size of the unstructured mesh are shown in table 3.2. h_{min} and h_{max} show the minimum and maximum spacing between grid nodes in meters. The final column is an additional constraint on the amount of grid nodes per radius of curvature. In other words, a higher radius of curvature - for example the blade leading and trailing edges - will require a higher node density. The fineness of the mesh is verified by means of a grid convergence study, the results of which are discussed at the start of chapter 5. Close to the blade surface, encompassing the boundary layer, a structured mesh region is constructed. Based on reference cases and basic boundary layer thickness calculations, the structured mesh is set to have a total thickness of $1.3 \cdot 10^{-4}$ m. There are 28 layers of cells perpendicular to the blade, increasing in thickness the further away from the blade surface. The first cell row has a thickness of $4 \cdot 10^{-7}$ m in order to ensure a $y+$ value of 1 or lower over the entire blade surface. The node spacing and structured mesh parameters remain unchanged for all different geometries that are set up for this research in chapter 4.

Table 3.2: *UMG2* mesh element size options.

Boundary	h_{min} [10^{-4} m]	h_{max} [10^{-4} m]	Node / RadCrv
Inflow & Outflow	6.0	6.0	5
Mixing Plane	3.0	3.0	5
Blade	0.5	1.0	15
Periodic	2.5	2.5	5

After running *UMG2* to generate the mesh, a second operation is required within *SU2* in order for the solver recognize the mesh as periodic. This is done using *SU2_PERIO*, part of the *SU2* software suite. Due to current inherent limitations in *SU2_PERIO*, the stator and rotor rows are meshed individually, after which both mesh files are merged into one. While complicating the process, the resulting mesh is verified to be fully functional. The final *.su2* file contains all the mesh information for use in an *SU2* simulation or optimization.

3.4. Simulation

SU2 offers the choice of a number of different solvers, among which an Euler and several types of Reynolds Averaged Navier-Stokes (RANS) solvers. Given the unsteadiness and working fluid related effects inherent to the research, the RANS solver is deemed most appropriate for the scope of this project. In this compressible RANS solver, the finite volume method is used to resolve the partial differential equations. Both upwind Roe and centered Jameson-Schmidt-Turkel (JST) flux formulations are available and will be used accordingly. There is an additional choice between Van Albada and Venkatkrishnan slope limiters.

There are multiple ways of closing the RANS equations. Two main types of Eddy Viscosity Models are available in *SU2*, namely Menter's Shear Stress Transport (SST) [39] and Spalart-Allmaras (SA) [40] turbulence models. All simulations and optimizations in this research work make use of the very robust one-equation SA turbulence model. Being a one-equation model, SA is less computationally demanding than models with two transport equations such as SST. Additionally, SA generally performs well in

turbulent flows, boundary layers and adverse pressure gradients. The combination of computational efficiency and good performance has made it popular in turbomachinery. An implicit Euler (pseudo) time marching method is used in this study for its stability. The Courant–Friedrichs–Lewy (CFL) number is set to guarantee good convergence and valid results.

A number of different boundary conditions can be selected in *SU2*. The following have been used in the simulations performed in this research:

- Inlet and outlet boundary conditions uniformly apply total inlet pressure and temperature, and static outlet pressure respectively.
- An adiabatic no-slip wall boundary condition is set on the stator and rotor blade surface.
- Periodic boundary conditions are applied on the upper and lower boundaries of the domain.
- A special mixing plane boundary separates the stator from the rotor domain in the steady-state simulations. This type of boundary condition averages out the flow quantities on the stator outlet and imposes them at the rotor inlet plane.

Flow properties at the inlet, outlet and mixing plane - or any longitudinal cross-section for that matter - are determined using *mixed-out averaging*. This mass-momentum-energy based mixing is more complicated than area or mass averaging, but more representative, especially in non-uniform flow fields. Figure 3.2 illustrates the different boundary conditions and their location of application within the flow field.

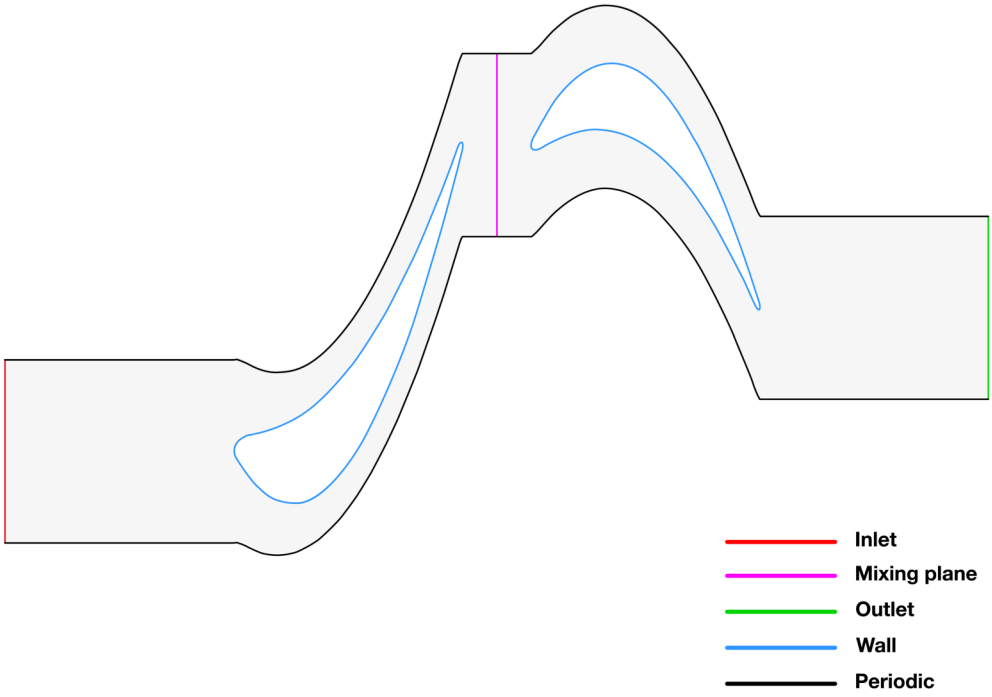

Figure 3.2: Visualization of the different boundary conditions applied to the flow domain.

Three branches of the *SU2* suite are used throughout the research. Flow evaluations for the steady-state mixing plane cases are performed in the *turbomachinery* branch. A dedicated *turbo_ffd* branch is used for shape optimization of those multirow stages. Finally, the *TMZHB* branch is characterized by

the harmonic balance method implementation and is therefore used for the unsteady simulations and optimizations.

In harmonic balance simulations, the number of time instances and associated harmonics and period are required inputs for *SU2*. The base angular frequency is based on the blade passing frequency as shown in equation 3.13. The set of frequencies that act as input to the simulation consists at least of zero, this angular blade passing frequency and its additive inverse. In case of more time instances, multiples or linear combinations of the base blade passing frequency can be added to the frequency set.

$$\omega = 2\pi \frac{U}{y_p} \tag{3.13}$$

The period is related to the angular frequency as follows:

$$P = \frac{2\pi}{\omega} = \frac{U}{y_p} \tag{3.14}$$

Multiple options exist concerning the thermal conductivity model used. In the simulations related to this thesis, the Prandtl number is assumed constant when determining the thermal conductivity of the working fluid.

3.5. Optimization

This part of the methodology sheds light on the optimization procedure available in *SU2* and used for the purpose of this research. The research makes use of unconstrained optimizations, as the goal is not to reach a perfectly feasible stage geometry, but to observe the effect of the flow solver on the shape perturbation as clearly as possible. The optimization problem can then be formulated as

$$\min_{\alpha} J(\boldsymbol{\alpha}), \quad \boldsymbol{\alpha} = (\alpha_1, \alpha_2, ..., \alpha_n) \tag{3.15}$$

where N is the number of design variables.

The objective function J used for all optimizations performed throughout this master thesis project is the entropy generation, s_{gen}, which is to be minimized throughout the optimization. This parameter is readily defined within *SU2* and can be defined as

$$s_{gen} = \frac{T_{t,in}}{v_0^2}(s_{out} - s_{in}) \tag{3.16}$$

The entropy values are determined using mixed-out averaging. v_0 represents the spouting velocity. Figure 3.3 shows the way *SU2* determines both the objective function and the sensitivities.

The blade parametrization step takes the design variables and comes up with a set of blade surface coordinates. The blade surface coordinates from the parametrization are used in the grid deformation step, representing the *SU2_DEF* module, to determine the volumetric grid coordinates. A flow solver iteration delivers the flow solution U. Finally, the adjoint step checks constraints and objective function. Additionally, the parametrization step can compute the sensitivity of the surface coordinates with respect to the design variables. In its turn, using the grid coordinates, the deformation procedure is called

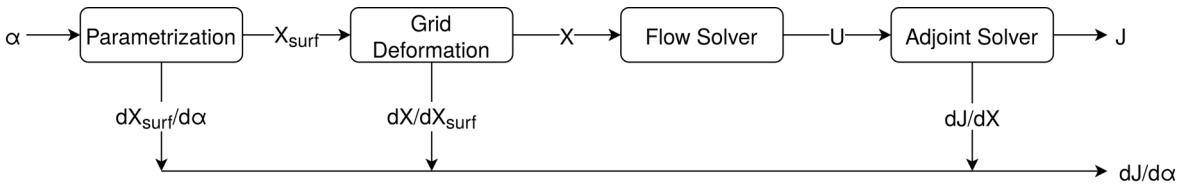

Figure 3.3: Optimization algorithm structure.

to determine the sensitivity of the volume to the surface grid coordinates. Finally, the adjoint solver delivers the sensitivity of the objective function with respect to the volumetric grid coordinates. Using a simple dot product, the three mentioned sensitivities result in the total gradient of the objective function with respect to the design vector.

3.5.1. Mesh Deformation

SU2 offers a selection of a number of different surface parametrization and mesh deformation techniques. Shape deformation in the optimizations performed in this thesis work make use of free-form deformation (FFD). Each of both blades is contained within an FFD box. Each FFD box is divided into a grid of 6 by 7, and as a result has 42 control points. It is decided to only allow perturbation of the control points in the y-direction, in order to limit complexity and keep the axial blade chords constant. As a result, each case has a total of 84 design variables. Figure 3.4 visualizes the shape of the FFD boxes and their control points.

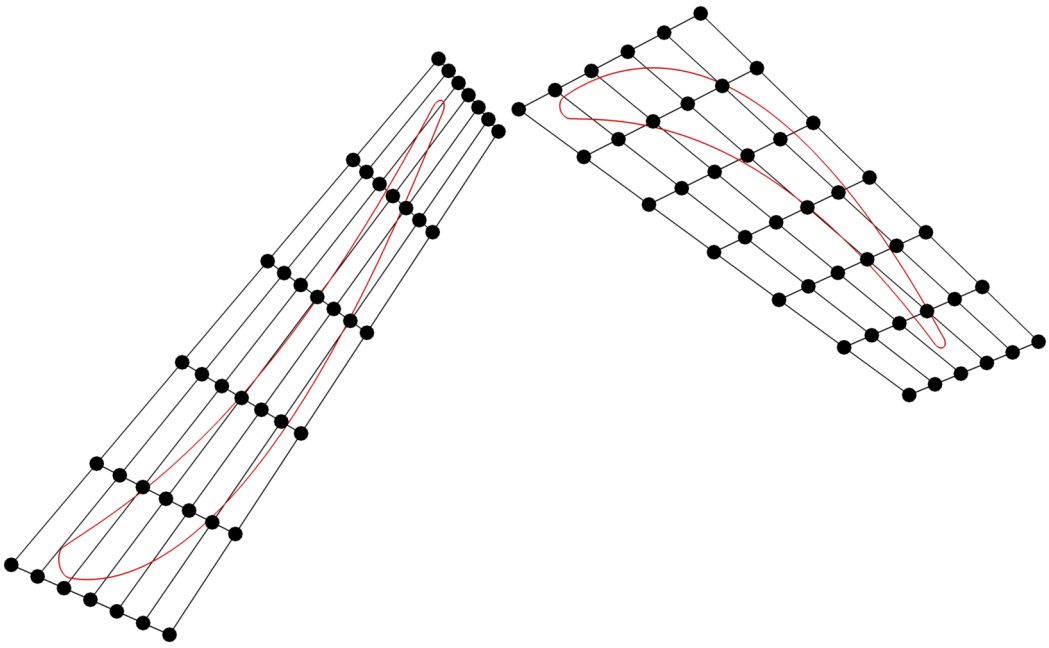

Figure 3.4: Free-form deformation boxes.

The FFD boxes and their position are specified within the *SU2* config file. A second-derivative continuity parameter makes sure that the blade wall within the box remains a continuous and smooth line. The *SU2_DEF* module is used to adapt the mesh file to contain the FFD information.

3.5.2. Adjoint Implementation

Both discrete and continuous adjoint solvers are available within the *SU2* software suite. The discrete adjoint method, as discussed in chapter 2, is selected for this particular application for its ability to determine the exact gradient as well as its favorable convergence behavior.

The discrete adjoint implementation in the *SU2_CFD_AD* module applies Algorithmic Differentiation (AD) to parts of the flow solver in order to determine the Jacobian to improve computational time and errors over manual linearization. Duality-preserving methods are applied to make sure the adjoint's convergence rate is the same as that of the flow solver.

3.6. Post-Processing

Various methods and tools are used in order to perform the different types of analysis in post-processing. This subsection gives an overview of the different programs that are used - both existing and written as part of the thesis work.

One aspect all post-processing has in common is the data it needs to work with. This consists of the different output files that are written as part of the simulation or optimization process by the *SU2* software suite. The most important data files are briefly described.

- *flow.dat* files contain an array of flow parameters at every grid point within the flow domain.
- *surface_flow.dat* files display the same information as present in the *flow.dat* files, but only along the blade surfaces.
- *history.dat* files present the evolution of some of the main stage characteristics and convergence residuals for every iteration of the simulation.
- *of_grad.dat* contains the gradients of the objective function(s) for each design variable.
- *surface_sens.dat* files have the surface sensitivities with relation to the objective function over the blade surfaces.

The main piece of software used in visualizing results and creating plots and figures is *Tecplot 360*. *SU2* is specifically set up to be compatible with either *Tecplot* or the open source *Paraview* software. Of both, *Tecplot* is deemed more capable for the task at hand. *flow*, *surface_flow*, *surface_sens* files and more can be simply loaded into *Tecplot* in order to visualize different flow characteristics throughout the geometry or flow field. The software additionally allows manipulation of a data set in order to plot flow parameters not present in the original input file, make corrections etc.

Additionally, a post-processing tool written in *Python 3* in the context of this research project is aimed at more analytical data processing. Using *flow.dat* files from *SU2* as inputs, it can perform more complex calculations, easily average information over a zone or cross-section and plot specific parameters.

Particularly interesting is its ability to calculate the flow coefficient, work coefficient and degree of reaction of the stage. Comparing these to the values initially envisioned in preliminary design is an important part of verifying the experimental process. The flow coefficient is determined from the flow results as follows.

$$\phi = \frac{\overline{V}_{ax,2}}{\overline{U}} \tag{3.17}$$

In this equation, the axial velocity is obtained from the *X-Momentum* output by dividing it by the corresponding local density. The subscripts 1, 2 and 3 represent the stator inlet, stator outlet and rotor outlet respectively. Quantities are mass averaged at the relevant station. In case of the harmonic balance results, flow data is first averaged over the five time instances. The work coefficient ψ is extracted as

$$\psi = \frac{\overline{w}}{\overline{U}^2} = \frac{\overline{U}\,(\overline{V}_{t,2} - \overline{V}_{t,3})}{\overline{U}^2} \tag{3.18}$$

Where V_t represents the transverse component of the velocity vector. Finally, the degree of reaction is reconstructed using

$$r^* = \frac{\overline{W}_3^2 - \overline{W}_2^2}{(\overline{W}_3^2 - \overline{W}_2^2)\,(\overline{V}_2^2 - \overline{V}_3^2)} \tag{3.19}$$

in which V is the absolute and W the relative velocity vector.

Finally, as a small side-project to the thesis, a tool is written in order to extract the time-unsteady flow results from the outputs of a harmonic balance simulation. This is achieved in the form of a *Rust* code developed in collaboration with Jonathan Van der Cruysse, PhD. candidate in computer science at McGill University. The code reads the config file of the simulation as well as the set of *flow.dat* or any output file coming from *SU2*. It then performs an inverse Fourier transform on the respective data. New output files are outputted for every chosen set of physical time steps. This can be useful for analyzing phenomena in physical time domain, or for illustrative purposes like in the form of a GIF.

3.7. Best Practices

From the plethora of data and trends resulting from the set of flow simulations and optimizations, conclusions can be drawn in the form of best practices for future 2D turbomachinery design problems. In particular, the focus is on the behavior of steady-state and harmonic balance unsteady solvers under varying operating conditions. These observations can be used to make predictions on solver performance for different stages, based on some of their nondimensional parameters. Concretely, the aim is to find a simple relation consisting of preliminary design parameters that is proportional with the difference in results ($\Delta\eta_{TT}/\eta_{TT,st}$) found across the set of flow simulations and optimizations. Such relation is obtained by means of an empirical process. The parameters affecting the divergence in flow results to the largest extent are identified from the wide set of flow simulation results. They are subsequently compiled into a simple relation, adjusted by iteration. Out of interest, a genetic algorithm is used to identify a similar relation, the result of which can be used as a verification.

4

Case Studies

As described previously, the aim of the research work discussed in this thesis report is to investigate the effect of variations in certain stage and flow parameters on the performance of harmonic balance versus steady-state flow solvers in design optimization. A crucial step in the process is therefore the selection of cases and variables which will be subject to the simulations and optimizations. This chapter describes in detail the process of selecting the different scaling parameters whose variation will result in the different case studies that are performed throughout the experimental part of the thesis work. It additionally shows how the methodology described in chapter 3 is used for this purpose.

4.1. Overview of Test Cases

The similarity variables determining the test cases are the flow and work coefficient, the specific heat ratio and the volumetric flow ratio, as shown in figure 4.1. The following subsections discuss how and why these particular sets of variables are selected.

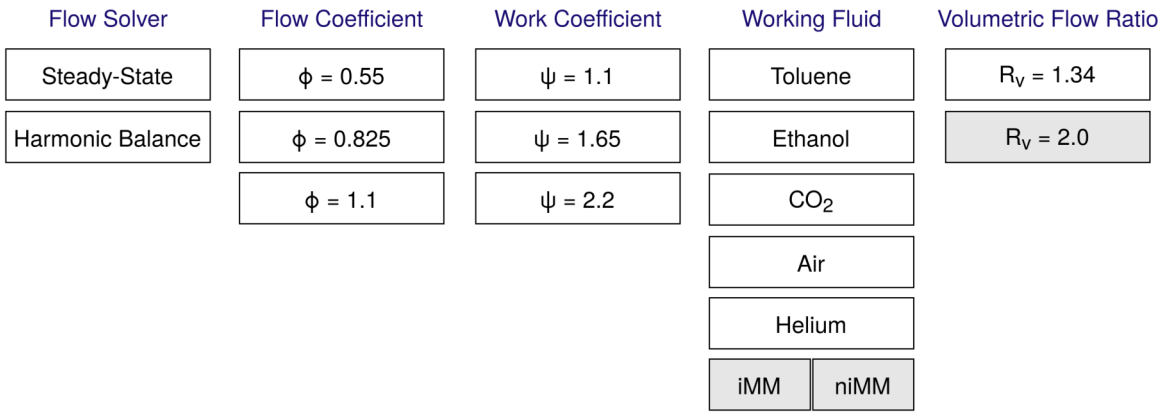

Figure 4.1: Simulation variables.

4.2. Stage Type (Duty Coefficients)

The goal of this part of the thesis work is to select a number of 2D turbine stage geometries that will be used for simulation and optimization later in the research. Given the limited time set aside for the master thesis project and the computational intensity that comes with these simulations and optimizations, choosing a select number of relevant test cases is crucial to obtaining a scientifically valuable result. In that light, it is decided to select nine different geometries. These nine stages are defined by a unique combination of one of three flow coefficients and one of three work coefficients. This way, the effect of varying both these defining parameters independently can be studied. This allows for focus on two of the main points of interest of the research: scaling parameters, and their individual, isolated effect on solver performance. The starting point of this selection is the Aachen 1.5 stage turbine, with $\phi = 0.55$ and $\psi = 2.2$ as its dimensionless parameters. From there, the flow and work coefficients for the other eight design points are selected as to evenly cover the main design space of axial turbines, with the lowest flow and work coefficient case in the maximum efficiency region of the Smith chart and stretching all the way to more extreme values of ϕ and ψ. These design points are shown on the Smith chart in figure 4.2. Different flow and work coefficients have been labeled with different ciphers and letters, giving each test case a unique label.

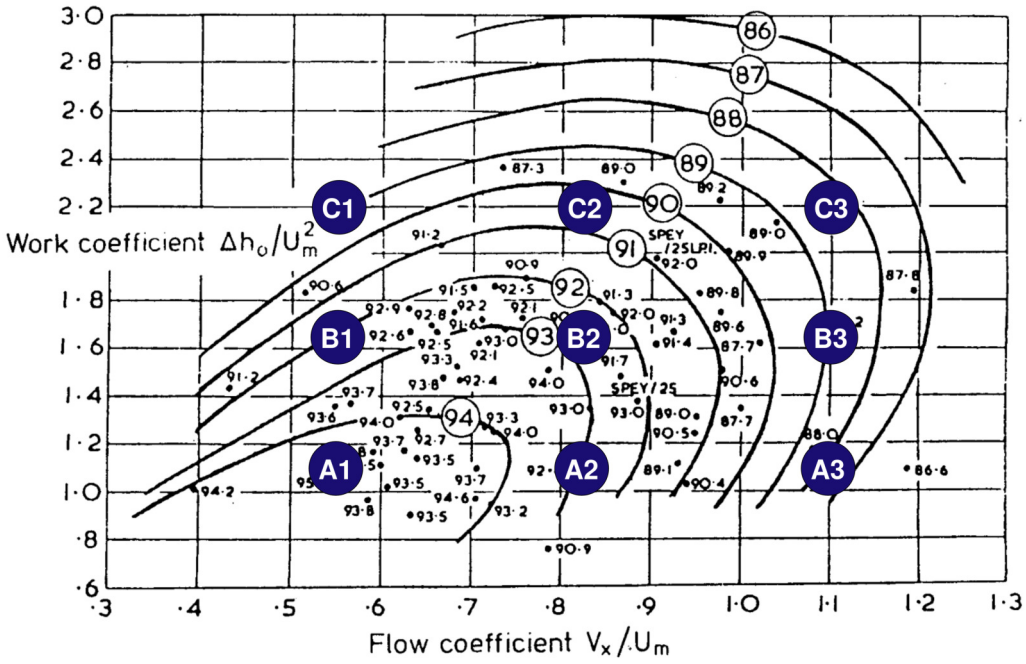

Figure 4.2: Smith chart with investigated stage types.

The degree of reaction is kept at 0.35 for all nine selected geometries, as it provides the highest efficiency over the range of work coefficients of the case studies. Low degrees of reaction generally are more suited for higher work coefficient cases and vice versa. The value of 0.35 is also found in the Aachen 1.5 stage reference turbine and D'Amato's representation of it [21]. The main stage characteristics of the *C1* stage are shown in table 4.2. As discussed in chapter 3, other stage characteristics are kept constant among the nine different design cases in order to isolate the effect of the changes in work and flow coefficient. Solidity is varied according to Zweifel's law, which in its turn completely depends on the flow and work coefficient and the degree of reaction.

The resulting blade shape for all nine stages that are created are shown in figure 4.3.

Table 4.1: Characteristics of stage *C1*.

Parameter	Unit	Value
ϕ	[-]	0.55
ψ	[-]	2.20
r^*	[-]	0.35
γ	[-]	1.4
R	[J/kg·K]	287.058
p_{t_1}	[Pa]	300,000
T_{t_1}	[K]	348.15
R_v	[-]	1.3359
$\dot{m}$	[kg/s]	5
Ω	[rpm]	9,000
b	[m]	0.0167
σ	[-]	0.800
t/b	[-]	0.250

The mesh of stage *C1*, as generated by *UMG2* is shown in figure 4.4.

4.3. Working Fluid

Apart from work and flow coefficients, the working fluid is another variable of which the effect on both flow solvers is to be investigated. Five different working fluids are selected for analysis in order to obtain a sizable dataset while keeping in mind computational requirements. They are selected to cover a range of γ, with air being the reference fluid.

Table 4.2: Selected working fluids.

Working Fluid	γ [-]	R [J/kg·K]	μ [μPa·s]
Toluene	1.043	90.24	6.5
Ethanol	1.13	180.50	9.7
CO_2	1.289	188.92	15.9
Air	1.4	287.06	20.9
Helium	1.67	2077.26	18.6

A very important aspect of performing simulations with varying working fluids - and so varying heat capacity ratios - is keeping all other similarity parameters constant. As a result, inlet pressure and temperature, pressure ratio and U change with different working fluids - as of course do γ, R and μ.

A second stage in the research focuses on non-ideal fluids. Giuffré [36] has described the γ_{Pv} poly-

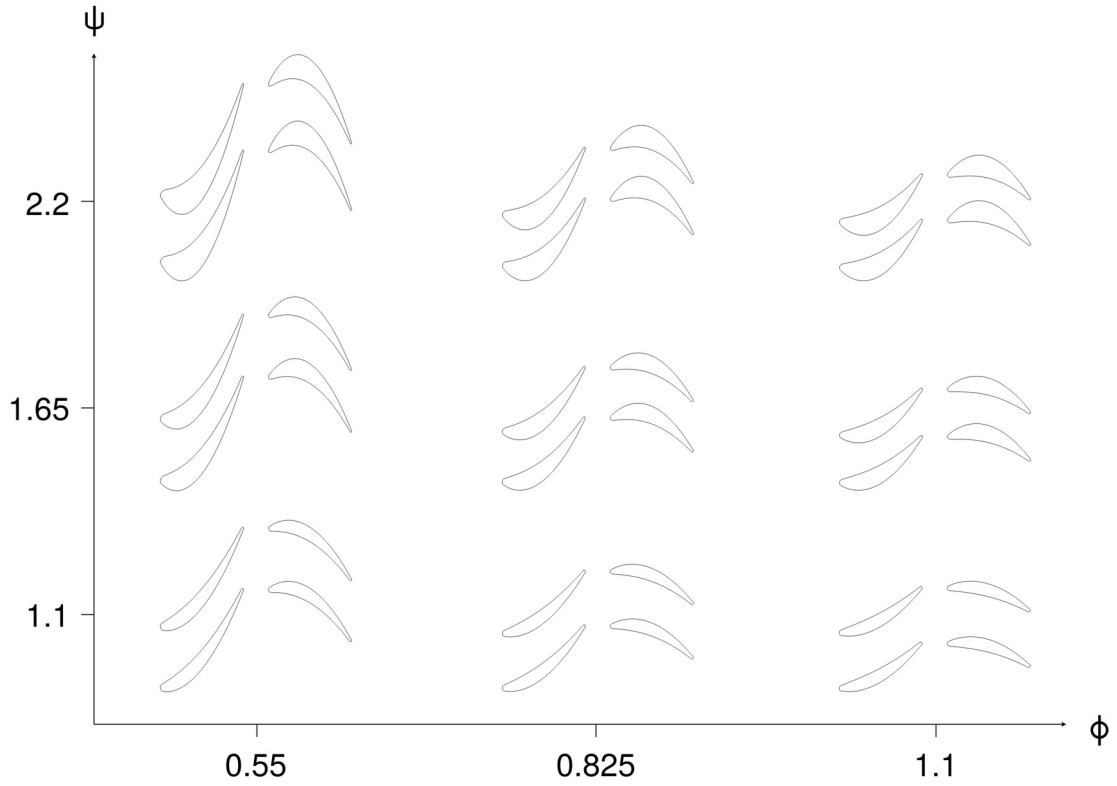

Figure 4.3: All nine stage geometries.

tropic coefficient and compared stage performance for cases in which γ_{Pv} is very different from γ, as described in more detail in chapter 2. In light of those finds, the experiments in this thesis are expanded to feature a $\gamma_{Pv} \gg \gamma$ versus $\gamma_{Pv} = \gamma$ case study. Giuffré shows that at higher values of γ_{Pv}, the flow Mach number increased significantly. In that light, this study is expected to find larger differences between harmonic balance and steady-state solving and optimization in nonideal flows at high values of γ_{Pv}. The working fluid used in this analysis is hexamethyldisiloxane (MM). This complex chemical compound (γ = 1.025) is commonly used in organic Rankine cycles. Siloxane is additionally chosen because for other working fluids such as CO_2, a supercritical expansion such as performed here would result in an incursion into the two-phase region, significantly adding to the difficulty of the problem. This ideal versus nonideal performance case is only carried out on one stage geometry. This gives a good idea of the effect on steady versus HB results without excessive computational costs. For the reference case, an ideal gas MM simulation is performed on the *A1* geometry. This stage is chosen for its location in the highest efficiency region of the Smith chart. Apart from the change in γ, the other similarity parameters are kept constant, analogous with the other working fluid cases discussed above. The main input parameters for the non-ideal case are shown in table 4.3. Here, ω represents the acentric factor, a state description parameter indicating the non-sphericity of molecules in a medium. This case is chosen in such a way that γ_{Pv} is significantly higher than γ. Total input pressure and temperature are selected to satisfy this condition. In practice, the constant volumetric flow ratio yields a higher expansion ratio, following equation 3.10 with γ_{Pv} instead of γ.

Because of the effect of the expansion ratio on the entropy generation, the rotational speed U is changed to keep the work coefficient constant in similarity. The frequencies needed for the harmonic balance computation are to be adjusted accordingly.

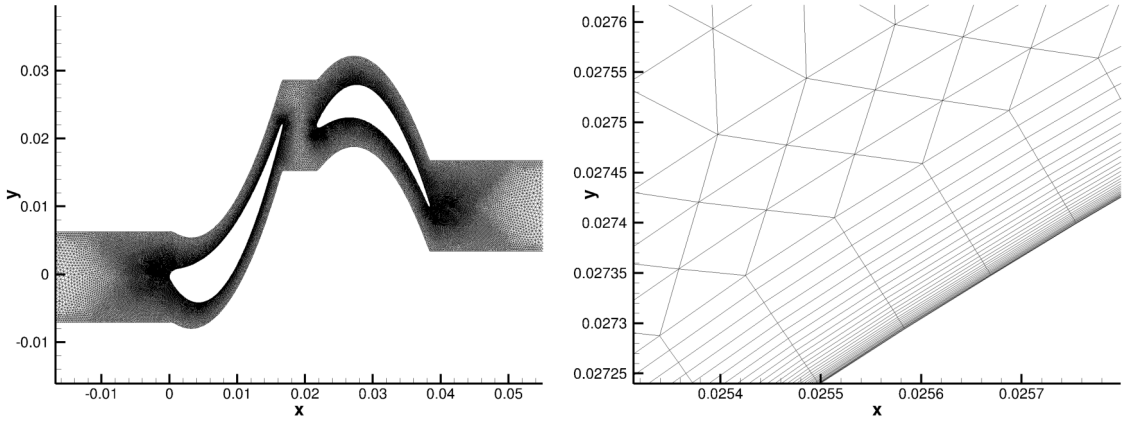

(1) Full mesh domain.

(2) Boundary layer detail.

Figure 4.4: Mesh of stage *C1*.

Table 4.3: Nonideal fluid case input.

Parameter	Unit	Value
P_c	[Pa]	1,939,000
T_c	[K]	518.75
ω	[-]	0.418
γ	[-]	1.025
P_{r_i}	[-]	2.063
T_{r_i}	[-]	1.052
γ_{Pv}	[-]	3.036
R_v	[-]	1.34
U	[m/s]	78.32

4.4. Volumetric Flow Ratio

A third parameter of interest is the volumetric flow ratio. An increase in volumetric flow ratio is expected to result in larger compressibility effects, which might well affect the difference in performance between steady-state and harmonic balance flow evaluations. For this part of the research, an additional set of flow simulations is done on geometry *A1*. Like for the original volumetric flow ratio, the simulations are performed with the five working fluids listed in table 4.2, and using both the steady-state and harmonic balance solver. The volumetric flow ratio R_v is set equal to 2, as opposed to the original value of 1.34. All other similarity parameters are once again kept constant. Consequently, only the output pressure is adjusted to match the volumetric flow ratio, while the rotational speed is changed to keep the work coefficient constant. All other input parameters are identical to those in the reference cases.

4.5. Technical Approach

Given the extreme computational cost of full optimization runs, the research will first feature a broad and in-depth series of flow simulations. This simulation set will allow the analysis and comparison of a large number of variation in stage characteristics.

- Nine different physical stage geometries will be used for simulation, based on three different flow and three different work coefficients.
- On all nine geometries, simulations with five different working fluids are performed. These five are the ones with a white box in figure 4.1 and indicated in table 4.2.

These experiments are all performed using an ideal gas model. These ideal gas equations of state make for lower computational times and less complex thermomodynamic behavior that can impact the flow results. When varying working fluids, using the ideal gas law ensures that the specific heat ratio is the only variable. Simulations make use of the robust and more simple one-equation SA turbulence model. A second order centered JST flux formulation scheme is applied along with the Venkatkrishnan slope limiter. The CFL number is set at six to satisfy the Courant-Friedrichs-Lewy condition and ensure acceptable convergence.

Apart from these 45 cases, additional variations are tested. These are the ones marked with grey boxes in figure 4.1.

- Two extra simulations are done on one set geometry, featuring ideal and nonideal MM as a working fluid. For the nonideal case, the Van der Waals equations of state are used in *SU2*, as described in chapter 3.

Because of incompatibility issues when combining the Van der Waals equations of state and a JST flux scheme, this set of simulations is done relying on the upwind Roe scheme.

- Another extra simulation is on that same geometry, with air and an increased volumetric flow ratio. The solver setup is the same as for the initial 45 cases.

The total amount of test cases is then equal to 48. All cases are resolved using both the steady-state and harmonic balance solvers in *SU2*. This brings the total amount of simulations to 96. All steady-state simulations are based on the implementation of a mixing plane between both blade rows.

A preliminary study is performed to identify the appropriate number of time instances for the harmonic balance computations. In order to do so, three flow simulations are carried out on stage *A1*. Each is characterized by a different amount of frequencies the simulation resolves for, while all other parameters are identical. The three time instance case solves for the blade passing frequency and its additive inverse, while the cases with five and seven frequencies also account for the double and triple of the blade passing frequency, respectively. Figure 4.5 shows the time variation of the total-to-total efficiency for the three cases. With more time instances, computational time goes up as does accuracy of the results. Taking seven time instances as a goal in terms of results, it is clear that the results obtained using only three time instances are significantly different. While the amplitude of the efficiency is similar, the variation is clearly out of phase. At a set time, the difference in results is much smaller when using five time instances (0.47 efficiency percent points compared to 1.25). In terms of computational time, using seven time instances takes 2.35 times longer than when making use of only three. The same

simulation with five time instances requires 1.79 times more CPU time than an identical three time instance simulation, and is consequently around 25% faster than when scaling up to seven. As a good compromise between accuracy and computational time, the harmonic balance simulations performed throughout this research are based on five time instances.

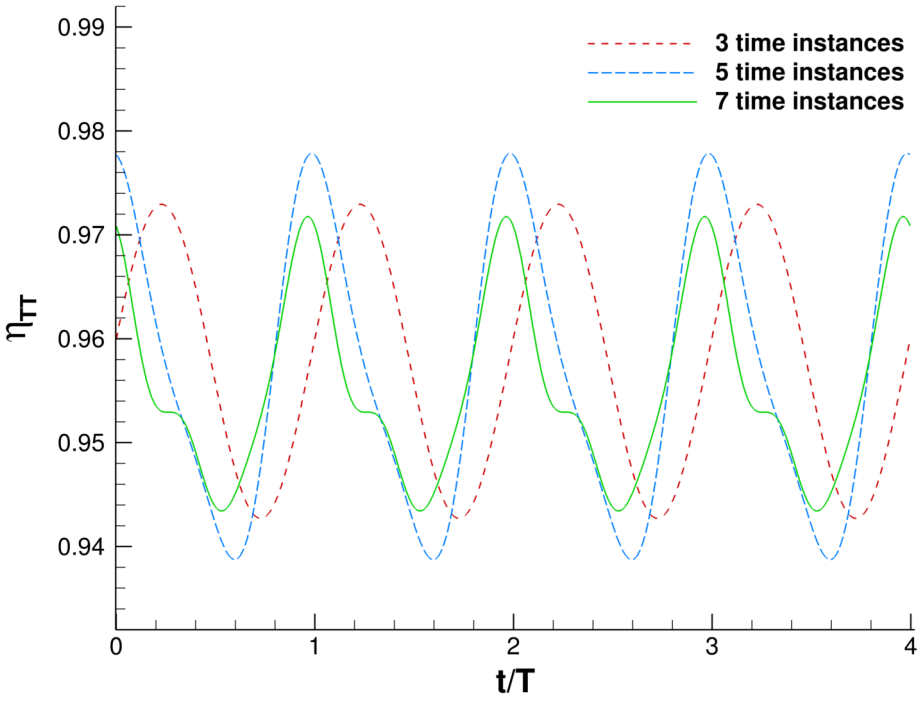

Figure 4.5: Total-to-total efficiency variation for different time instances.

Based on the trends observed in the simulation results (and discussed in detail in chapter 5), two cases are selected for a full shape optimization - along with a reference case. The main goal of the optimization part of the research is to verify whether the optimization results match the flow and performance values obtained from the flow simulations. As an extension, it will allow investigation in to what degree the trends derived from the simulation set hold for full shape optimizations, and so if best practices based on flow simulation can simply be extended for use in an optimization context.

The to be optimized stages are selected in order to cover a few interesting aspects accordingly.

- The $\phi = 0.55$, $\psi = 1.1$ highest efficiency stage referred to as *A1* will act as a reference case. The reference volumetric flow ratio of 1.34 is applied, and air is selected as the working fluid under ideal gas law.
- An increased work coefficient case ($\phi = 0.55$, $\psi = 1.1$ - geometry *B1*) is investigated to gain insight in the effect of increased blade loading. Here, the influence of work coefficient and Mach number is the focus. Again, the case is characterized by $R_v = 1.34$ and ideal air.
- The inputs and physical quantities associated with the test cases are identical to their respective flow simulations and can be found above.
- As described in chapter 3, the optimizations make use of the discrete adjoint solver in *SU2*. FFD boxes facilitate morphing of the airfoils.

- The objective function of the optimization is a minimization of the entropy generation.
- Scaling factors are applied to the objective function accordingly, as to facilitate subtle but significant design step changes and good overall optimization behavior.
- The number of optimization design steps is limited to twenty in order limit computational time while still allowing for plenty of iterations.

A final part of the processes in *SU2* is a full high-fidelity flow simulation of the optimized stages. This way, the MP and HB optimized blade shapes can be compared on equal footing. For this purpose, a simulation is run using the harmonic balance solver but using seven instead of five time instances.

5

Results and Discussion

This chapter presents the results of the simulations and optimizations that are performed throughout this master thesis research. The results are accompanied by thorough discussion and interpretation. Section 5.1 is reserved for the results of the larger set of flow simulations. Within this secion, three main areas of interest are distinguished. These correspond to the effects of varying three main nondimensional groups. Firstly, subsection 5.1.2 studies the effect of the flow and work coefficient. Secondly, the impact of the similarity parameters γ and γ_{Pv} are discussed in 5.1.3. Finally, 5.1.4 focuses on the volumetric flow ratio R_v. Full adjoint shape optimizations are discussed in section 5.2. The development of best practices for future turbomachinery design in section 5.3 finalizes this chapter.

5.1. Flow Simulations

5.1.1. Convergence and Results

Mesh Convergence Study

The properties of the mesh can have a major influence on the results of the simulation. It is therefore of paramount importance to perform a mesh convergence study. In a mesh convergence study, the number of elements in a mesh is varied in order to study its effect on the outcome of the simulation. This will help in selecting a mesh that accurately captures the flow, without being unnecessarily fine and computationally intensive.

Seven different versions of the mesh are set up for this grid convergence study. The reference mesh is the one corresponding to the input parameters in table 3.2. This mesh has 105,920 elements. Three finer and three coarser meshes are set up for comparison. In order to create these meshes, the minimum and maximum node spacing is scaled by a constant factor. The structured mesh composition and thickness are left untouched. Table 5.1 shows the different meshes along with the total-to-total efficiency resulting from the *SU2* steady-state flow evaluation. The final column shows the total runtime of each simulation. The grid convergence study is done using the steady-state solver in the *turbomachinery* branch of *SU2*. Figure 5.1 illustrates the total-to-total efficiency as a function of the number of elements in the mesh, relative to the reference mesh.

Table 5.1: Mesh convergence study for *C1*.

Elements	η_{TT} [%]	Runtime [s]
22,297	91.97	1,365
39,029	93.26	1,647
57,430	93.91	2,223
105,920	94.60	3,375
147,868	94.66	4,499
209,941	94.71	7,806
284,763	94.51	11,903

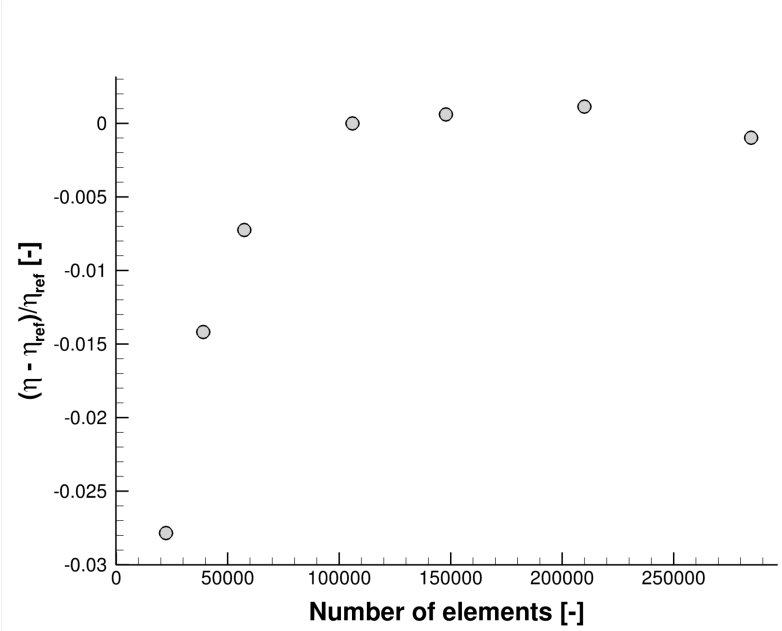

Figure 5.1: Mesh convergence study of stage *C1*.

The results of the mesh convergence study show an obvious trend. The outcome of a flow simulation is clearly dependent on the fineness of the mesh. However, this dependence - indicated by the differences in results - decreases as the number of mesh elements increases. This grid convergence study confirms that the 105,920-element reference mesh is adequate for the purpose of this research. Its results are only marginally different from those obtained with much finer meshes, while guaranteeing a reasonable computational time.

Simulation Convergence

The convergence history of the flow simulation of stage *C1* in the turbomachinery branch of *SU2* is shown in figure 5.21. Likewise, figure 5.22 shows the convergence behavior of the harmonic balance simulation of the same stage, obtained by means of the harmonic balance solver implemented in the *feature_TMZHB_temp* branch of *SU2*. Both convergence plots show a reduction of close to four orders of magnitude in the density residual. The convergence behavior looks satisfactory overall. The

steady-state simulation converges in 6,138 iterations. In harmonic balance, the flow evaluation requires 13,397 iterations - double the amount.

Running on the student's personal computer, using seven of the eight available CPU cores, the steady-state flow simulation takes 55 minutes to converge. At 599 minutes - 10 hours - the HB simulation runs for approximately ten times as long to reach the same residual reduction. This can be attributed to the HB needing double the amount the iterations, and the iteration taking around five times longer than in the steady-state case. Apart from usual variations, the computational times of steady-state and harmonic balance simulations for other geometries and working fluids behave the same. This finding is significant, and it clearly reiterates the core goal of this thesis work. While the harmonic balance method delivers a way of obtaining unsteady flow results at a fraction of the cost of full time-accurate simulations, the computational time is still significantly higher than is the case with steady-state solvers. It is therefore in the interest of research and industries to establish where the harmonic balance solver delivers significant improvements in accuracy, as to be able to decide whether it is worth the increased computational time over an equivalent steady-state simulation.

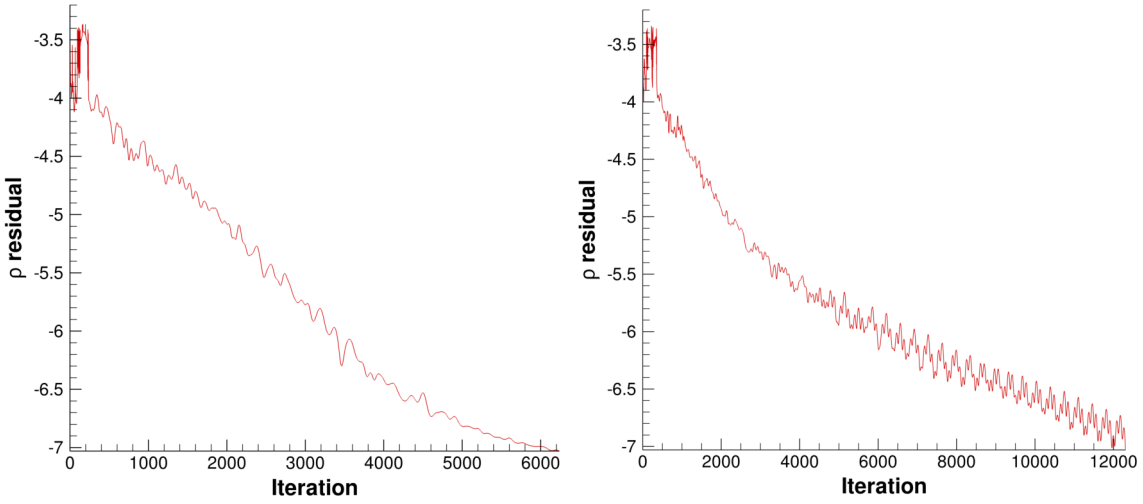

(1) Steady-state.

(2) Harmonic balance.

Figure 5.2: Convergence history of the flow simulation of stage *C1*.

Simulation Outputs

SU2 provides the user with a detailed set of output parameters. Flow files encompass the values of a whole range of flow data. For harmonic balance simulations, different flow output data are written for all chosen time instances. For example, figure 5.3 shows the entropy generation throughout the flow field for both the steady-state flow simulation and the five harmonic balance time instances, for geometry *C1* with air. Entropy generation is chosen for this illustration in order to highlight the difference in operation and results between steady-state and harmonic balance computations. Figure 5.31 clearly shows the effect of the mixing plane in between the stator and rotor blade rows. The flow parameters are averaged out, and as a result the rotor row experiences a uniform flow field at its input. The harmonic balance results illustrate how the wake that is generated at the trailing edge of the stator is transported into the rotor domain and subsequently travels and diffuses throughout the rotor passage. Figures 5.32 through 5.36 also show the rotation of the stator domain and the time variance of the flow field.

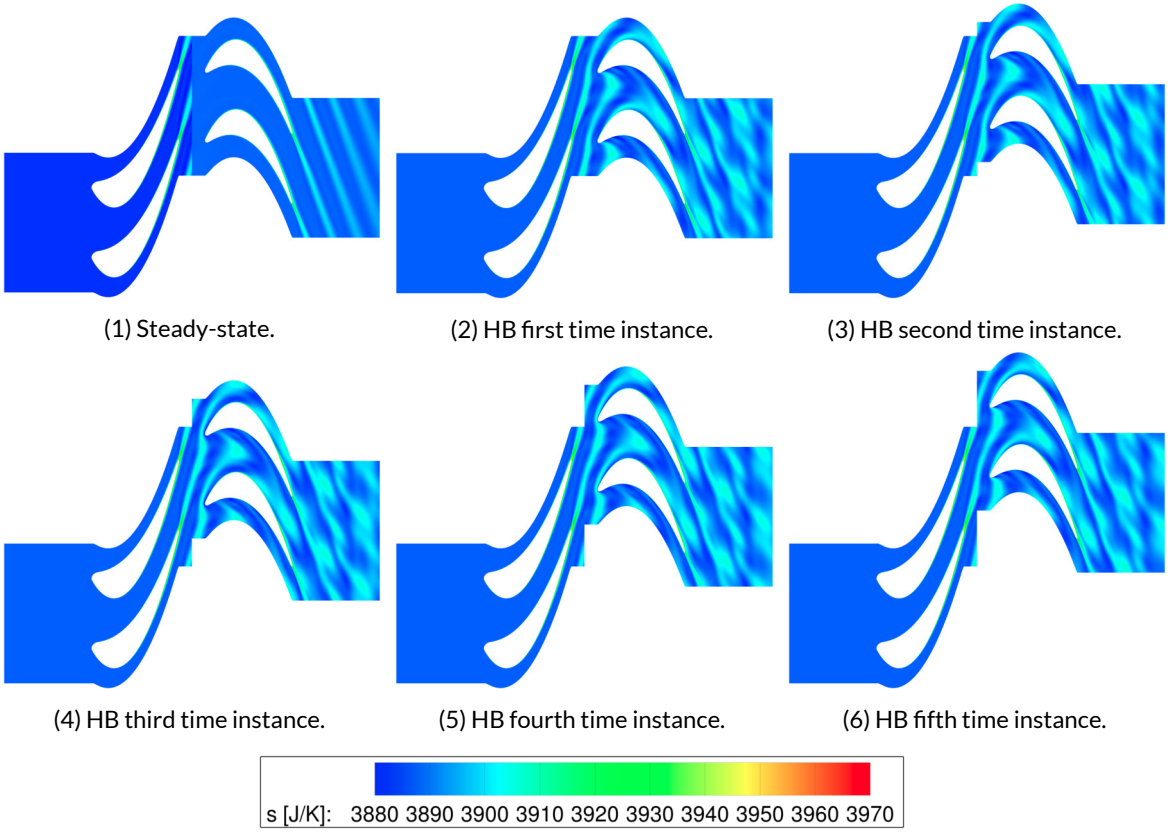

Figure 5.3: Entropy generation.

In order to verify the entire simulation set-up process, the flow coefficient, work coefficient and degree of reaction are derived in post-processing from the simulation results. The calculations performed in order to do so are presented in section 3.6 of the methodology chapter. They are then compared to the values selected in the preliminary design phase as described in chapter 3.

Table 5.2 shows the values of these three nondimensional parameters for the steady-state and harmonic balance simulations of stage *C1* with air in ideal gas. Especially given the manifold of steps between selecting the stage parameters and obtaining the simulation results, the stages closely resemble those envisioned in preliminary design. It is to be noted that the flow and load coefficient and degree of reaction match even better for the stages closer to the ideal point, with stage *A1* in steady-state having values that are off by five, one and half a percent respectively. A second observation is that the harmonic balance simulations generally seem to match the set-out values for these dimensionless parameters less well than the steady-state ones.

Table 5.2: Nondimensional parameter validation of stage *C1*.

Parameter	Theory	Steady	HB
ϕ [-]	0.55	0.48 (-13%)	0.41 (-25%)
ψ [-]	2.2	2.23 (+1.3%)	1.93 (-12%)
r^* [-]	0.35	0.30 (-14%)	0.40 (+13%)

5.1.2. Effect of Change in Duty Coefficients

The flow and work coefficients are the first two scaling parameters whose effect is evaluated. The observations include the impact of variations in these duty coefficient on both the absolute flow results and - more relevant towards the research objective - the difference between steady and HB solvers. The results originate from eighteen separate flow simulations, from three different flow coefficients, three different work coefficients and two flow solvers.

The results of the flow simulations show a clear dependency of steady-state versus HB behavior on stage work and flow coefficient. Figure 5.41 shows the relative total-to-total efficiency difference between the harmonic balance and steady-state flow simulations as a function of flow and work coefficient. Across the board, the performance difference increases strongly with work coefficient. The relation with flow coefficient is less clear-cut, with the trend also suggesting smaller deviation as the flow coefficient increases at the low work coefficients. The total opposite is true at the highest work coefficient, where increasing the flow coefficient looks to be accompanied by a strong increase in the discrepancy between the steady-state and harmonic balance results.

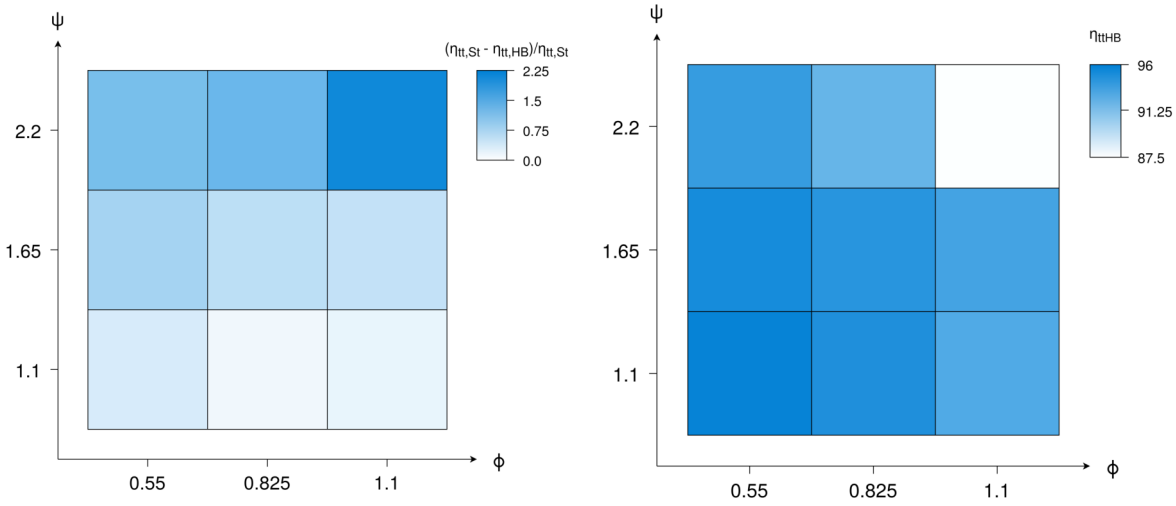

(1) Efficiency deviation.

(2) Total-to-total efficiency.

(3) Reduced frequency.

(4) Stage max Mach.

Figure 5.4: Efficiency deviation, reduced frequency and Mach number in function of flow and work coefficient.

Overall, the results suggest that there is an inverse relation between the efficiency of a stage and the difference found between its steady-state and harmonic balance flow parameters, as can be seen in figure 5.42. The hypothetical explanation here is that the phenomena that cause losses - and therefore make a stage less efficient - are quite often associated with unsteadiness. Therefore, the phenomena making for less efficient stages - wakes, shocks and vortices - are the ones that are difficult for steady-state solvers to accurately resolve. Still, the relation does not hold everywhere. While geometry *A2* has a lower efficiency that stage *A1*, the steady-state solver clearly finds results closer to the harmonic balance solver than in that second stage geometry. The same holds for the cases at $\psi = 1.65$.

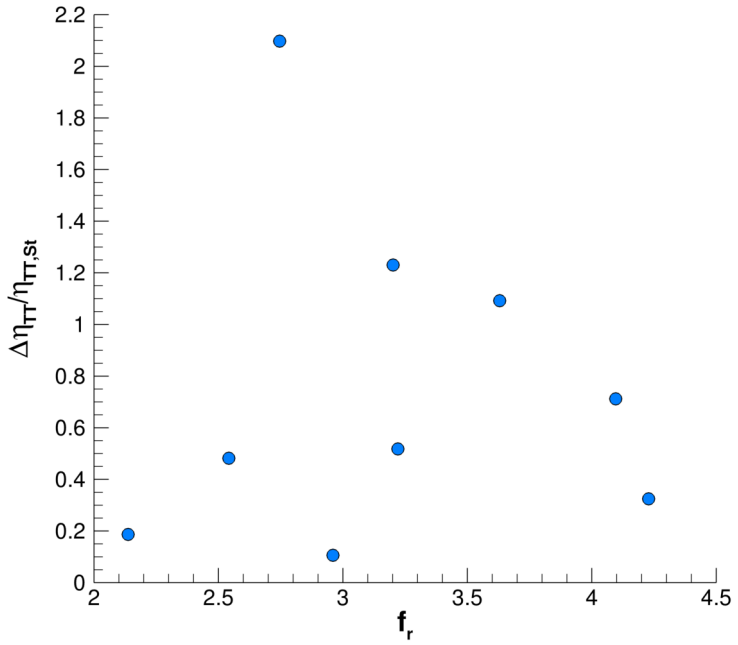

Figure 5.5: Total-to-total efficiency difference between steady-state and HB flow simulation in function of reduced frequency for stage *A1*.

The reason for these observations may lie in the interplay between subsonic unsteady effects - static pressure fields, wake - and high Mach effects. As discussed earlier, the reduced frequency serves as an indicator for the presence of unsteady effects in a flow field. Hypothetically, the reduced frequency is therefore an indicator of the performance difference between both solvers. Figure 5.5 shows the difference in simulated efficiency in function of reduced frequency of a stage. The hypothesis would suggest an increasing trend, with difference between MP and HB results increasing as a function of the reduced frequency of the stage. Unfortunately, there is no such clear-cut trend. Looking at the individual data points as illustrated in figure 5.4 does show the expected behavior to a certain extent. One expects the difference between results obtained by the steady-state and harmonic balance solvers to be larger at higher reduced frequencies. This is indeed the case for the *A1-3* ($\psi = 1.1$) and *B1-3* ($\psi = 1.65$) case studies. A lower flow coefficient yields a higher reduced frequency, as axial velocity is decreased and the transport contribution becomes smaller compared to the unsteadiness. This inverse relation between flow coefficient and the difference in results is clearly observable in figure 5.41. Looking at the data points, there is also an increase in reduced frequency with the work coefficient in the $\phi = 0.825$ and $\phi = 1.1$ columns, though the magnitude of the increase is not as large as was the case with the dependence on flow coefficient. For the $\phi = 0.55$ column, the reduced frequency even slightly reduces as the work coefficient goes up. While this can explain the smaller increase in efficiency difference as compared to the other columns, it is not yet clear why then the difference in results increases at all within the

column itself. Additionally, the reduced frequencies do not yield any explanation for the sharp increase in steady-state-to-HB difference with flow coefficient as observed at the highest work coefficient. The results show a correlation between performance difference and reduced frequency to be present. However, it is clear that more characteristics are at play. In order to deduct a clean indicator of performance difference - which is the goal of this thesis work - these other characteristics are to be identified.

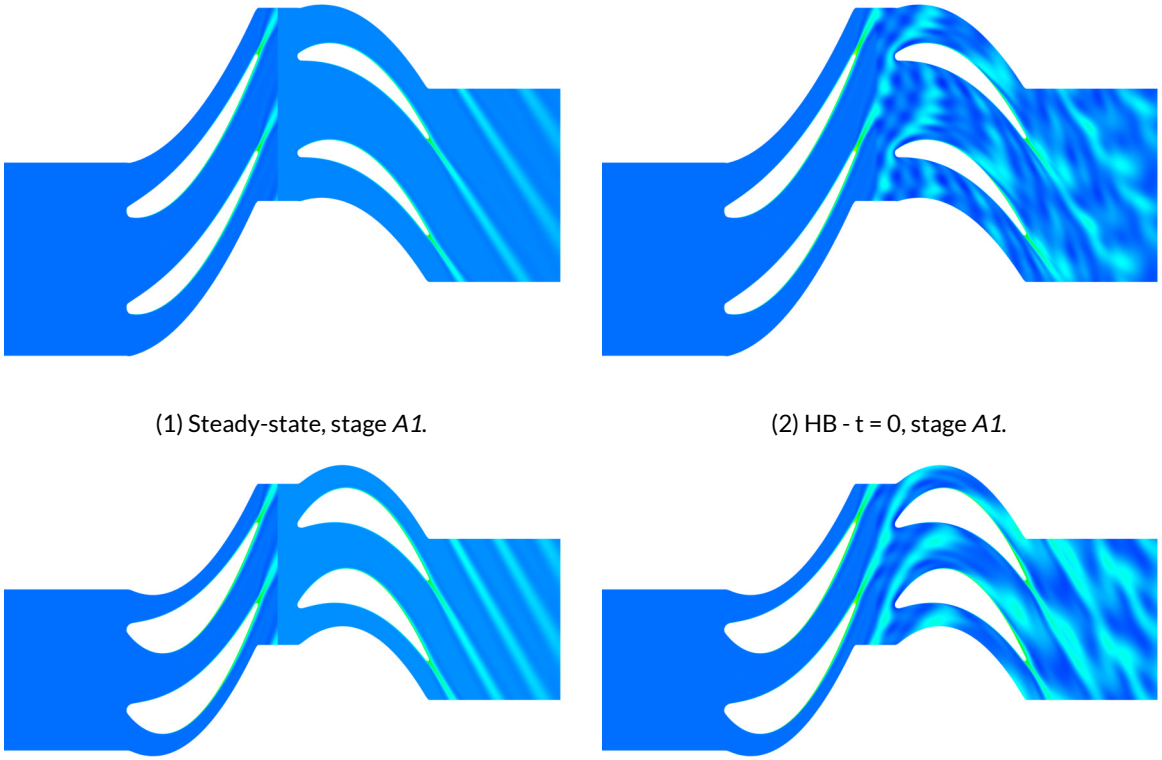

(1) Steady-state, stage *A1*. (2) HB - t = 0, stage *A1*.

(3) Steady-state, stage *C2*. (4) HB - t = 0, stage *C2*.

Figure 5.6: Normalized entropy contours of a steady-state versus harmonic balance flow simulation of stages *A1* and *C2*.

Some of the deviant behaviors concerning the reduced frequency dependence are indicative of the effect of the Mach number and shock waves in the flow parameters and consequently the solver performance. Introducing the Mach numbers achieved in each of the flow fields as shown in figure 5.44 fills in the missing part of the picture. It is clear that the Mach number increases proportionately with the flow coefficient. This is to be expected, due to the direct relation between flow coefficient and flow velocity. Less straightforward is the link between work coefficient and Mach number. The increase is only noteworthy going from $\psi = 1.65$ to $\psi = 2.2$. The results suggest that the effect of the Mach number is not proportional. At speeds well under the transonic region, a step change in Mach number does not effect the efficiency difference to the same extent as an increase from for example Mach 0.9 to Mach 1. Test case *C3*, at $\phi = 1.1$ and $\psi = 2.2$ displays a disproportionately high and supersonic flow velocity. This last point is due to the case's very extreme location within the Smith chart, where apart from physical extremities, the solver may struggle to get accurate results. The high Mach number along with the solver performance directly result in the high deviation that is encountered between the steady-state and harmonic balance results.

A number of these trends can be seen reflected in the flow fields of two stages that perform very differently, like those of *A1* and *C2* shown in figures 5.7 and 5.6. The Mach contours clearly confirm the data in figure 5.44, in the fact that stage *C2* displays higher maximum and overall Mach numbers, espe-

cially over the suction sides of the stator and rotor blades. These critical transonic regions are impacted to a larger degree by the unsteady effects captured in the harmonic balance simulations. The figures in 5.7 do seem to show a large difference between the steady-state and HB velocity fields in the *C2* case as compared to the higher effiency *A1* geometry. This directly contributes to the larger difference in performance as seen in figure 5.44. Opposite to the Mach number, the reduced frequency was earlier found lower in *C2* than in *A1*. The entropy fields as shown in figure 5.6 present a more nuanced picture. The wakes seem to be similar to slightly larger in stage *C2*. However the structure of the wake interaction and overall optical degree of unsteadiness seems more pronounced in the *A1* case - conform with what is expected giving its larger reduced frequency.

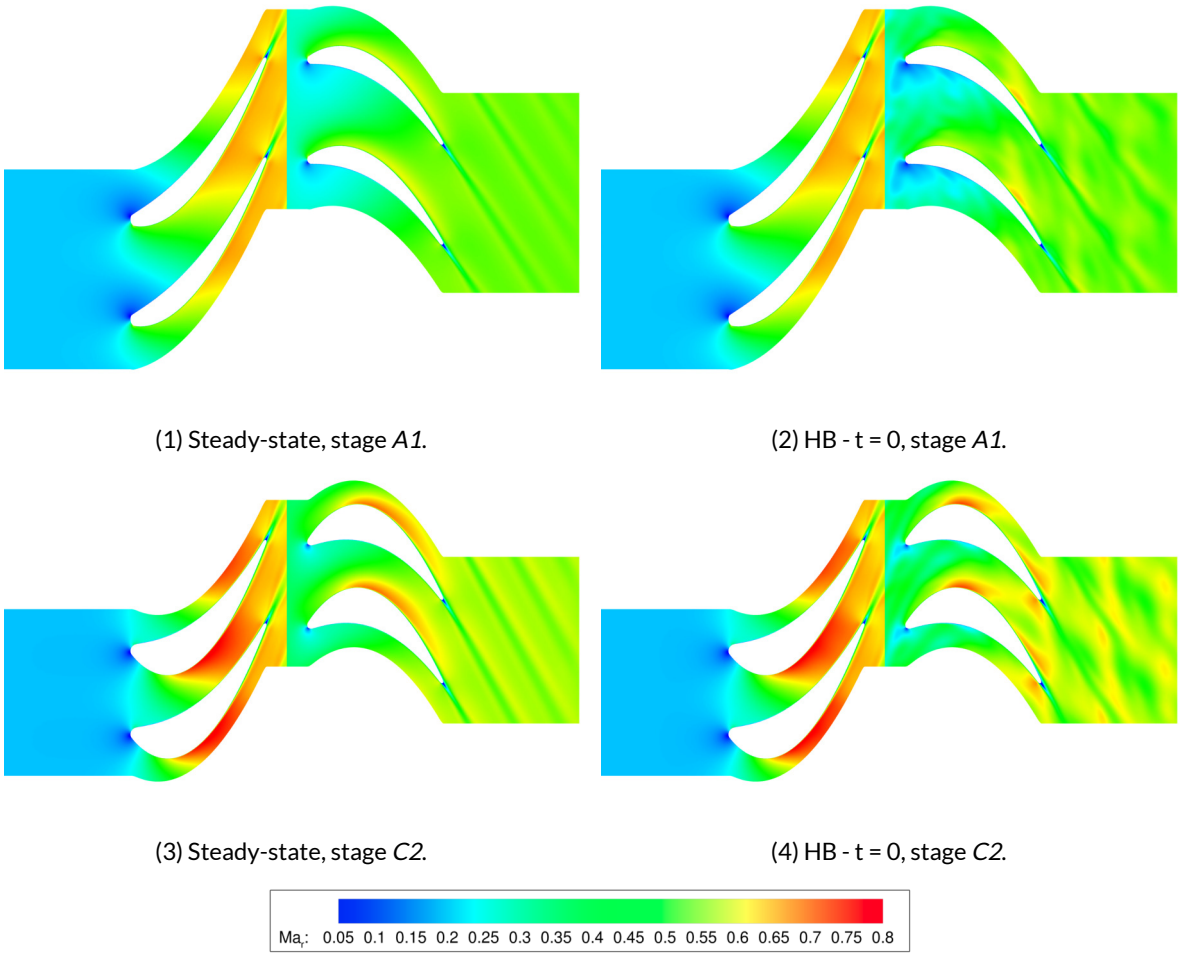

(1) Steady-state, stage *A1*.

(2) HB - t = 0, stage *A1*.

(3) Steady-state, stage *C2*.

(4) HB - t = 0, stage *C2*.

Figure 5.7: Relative Mach contours of a steady-state versus harmonic balance flow simulation of stages *A1* and *C2*.

Still, when looking for a clear trend based on reduced frequency and Mach number, there seems to be a missing factor. The results as illustrated in the plots in figure 5.4 show a general increase in the difference in solver performance with work coefficient ψ. This trend is however not strongly reflected either in the Mach number or the reduced frequency. Physically, the work coefficient is the relation between the specific work of the stage and the peripheral kinetic energy. Consequently, a higher work coefficient indicates a higher blade loading. Within the flow field, the blade loading translates into the pressure distribution around the blade. This hypothesis based on theory is clearly visible in the simulation results. Figure 5.8 shows the static pressure fields in the stator domains of stage *A1* (ψ = 1.1) and *C1* (ψ = 2.2). These visualisations clearly confirm the existence of a more extreme and locally perturbed pressure field at the higher work coefficient. As described in chapter 2, the local pressure field is one of the main sources of unsteadiness within a turbomachinery stage. All geometries considered in this research are

characterized by the presence of two blade rows - a stator followed by a rotor. In such setups, the pressure perturbation originating from the stator row will result in a non-uniform pressure field at the inlet of the rotor domain. Due to the movement of this second, rotor row, this spatial unsteadiness becomes a time unsteadiness. The results obtained by a solver taking into account such behavior - the harmonic balance method in this case - is therefore expected to capture this effect better than the steady-state solver, which averages out the pressure field at the mixing plane. While the reduced frequency is an indicator of the frequency with which the rotor blade cuts through the upstream pressure perturbation, it does not account for the magnitude of such pressure difference. This explains why the reduced frequency, even when adjusted for Mach and shock effects fails to predict the difference in results found with an increase in work coefficient. In that light, the work coefficient may then be used to adjust or correct the reduced frequency parameter.

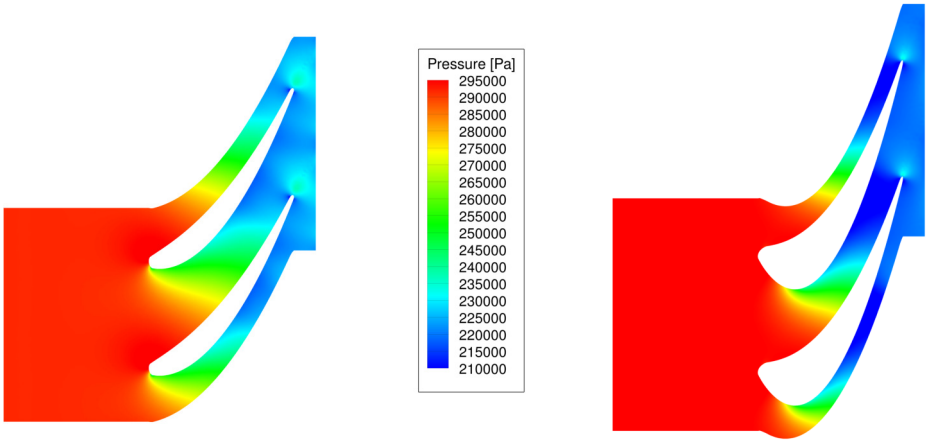

(1) *A1* (ψ = 1.1). (2) *C1* (ψ = 2.2).

Figure 5.8: Stator pressure fields.

Based on the findings discussed above, the aim is to find one or more parameters that can serve as an indicator for the difference between steady-state and HB unsteady flow evaluations. The process of obtaining such indicator is described in detail in section 5.3.

5.1.3. Effect of Change in Working Fluid

Effect of Change in γ

Simulations are done in steady-state and harmonic balance for the five different working fluids listed in table 4.2. While the specific heat ratio and gas constant vary, all other similarity parameters are invariant. This way, both the scaling principles and the independent effect of variations in γ can be optimally studied. The polytropic ideal gas law applies to this set of simulations. Its governing equations are discussed in more detail in chapter 2. The flow simulations are performed on all nine different stage geometries.

The output of this set of flow evaluations leads to several clear and interesting results. Over the entire set of test cases, the total-to-total efficiencies obtained by both the steady-state and harmonic balance solver do not change with variation in specific heat ratios. This is illustrated in figures 5.91 through 5.93. In all but one case, the figures show that the efficiencies found from the flow simulations at differ-

ent working fluids are within a percentage point from each other. Looking at the small variation there is, no clear increasing or decreasing trend or dependency is found in the stage efficiency in function of molecular complexity. Analyzing the flow fields and stage characteristics in more detail reveals the underlying physical cause for the lack of variation of stage efficiency with specific heat ratio. Along with the total-to-total efficiency, the flow field and its physical quantities remain almost identical when varying the working fluids within the boundaries of the selected similarity parameters.

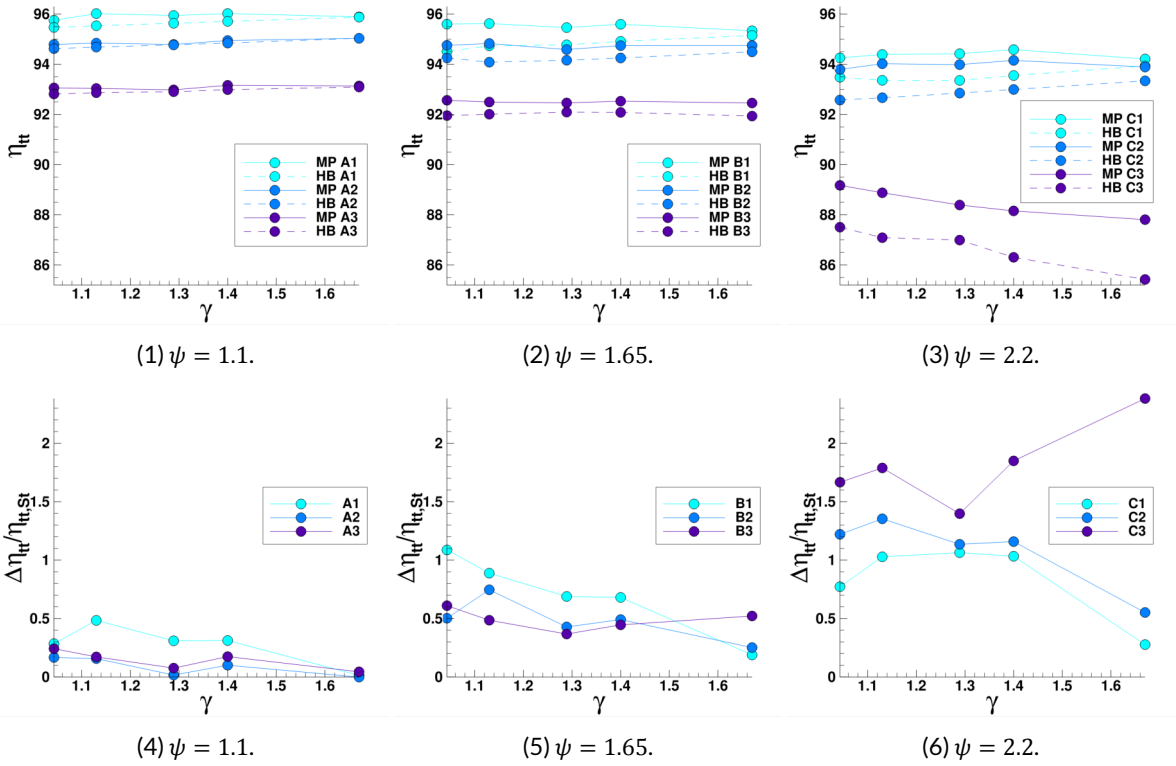

(1) $\psi = 1.1$. (2) $\psi = 1.65$. (3) $\psi = 2.2$.

(4) $\psi = 1.1$. (5) $\psi = 1.65$. (6) $\psi = 2.2$.

Figure 5.9: Total-to-total efficiency and total-to-total efficiency difference between steady-state and HB flow simulation in function of γ.

A similar level of invariance with working fluid is visible when comparing the steady-state and harmonic balance results. Figures 5.94 through 5.96 highlight the difference between total-to-total efficiency found by both flow solvers in function of the working fluid and confirm these observations. Due to both the very small size and the lack of consistency in the variations of results, both the flow characteristics and solver performance are deemed independent of γ. Stage *C3* exhibits slightly larger differences both in stage total-to-total efficiency and difference in solver performance when varying its working fluid. This is at least in part due to the extreme combination of duty coefficients. In this region of the Smith chart, the resolved flow behavior tends to diverge farther from reality. Still, the variation is smaller than two and three percentage points, respectively. This is encountered to an equal degree in the total-to-total efficiency found by the steady-state and the harmonic balance solver. The difference between their results is quasi invariant, as in the eight other stage geometries.

The above described behavior is in line with Giuffré's remark for the use of the volumetric flow ratio as a similarity parameter as opposed to the expansion ratio [36]. Just as in the results of that earlier mentioned work, a constant volumetric flow ratio makes for small(er) variations in results when varying γ. In case the expansion (pressure) ratio β would have been kept constant instead, the flow would show more significant differences between the different working fluids. In essence, the volumetric flow ratio R_v in itself acts as a normalization of the expansion ratio with respect to the specific heat ratio. The relation between expansion and volumetric flow ratio is shown in equation 3.10.

Consequently, in the set of simulations performed and discussed here, the expansion ratio increases with γ. The rotor rotational speed U is increased accordingly in order to keep ϕ constant between the different working fluid cases of each geometry. The relation for the work coefficient ψ of a stage as shown in 3.5 can be rewritten as

$$\psi = \frac{V_{ax}\ (\tan \alpha_1 - \tan \beta_2)}{U} + 1 \tag{5.1}$$

The flow angles can be assumed constant over the different working fluids given kinematic similarity. As discussed above, the axial velocity increases with γ as the expansion ratio grows larger accordingly. The manual increase in U that keeps the flow coefficient constant then fulfills the same role for the work coefficient. The similarity principle clearly holds over this range of test cases, explaining the independence of stage performance on the specific heat ratio, which is then not a scaling parameter of the problem at hand.

Investigating the three different aspects found to govern the behavior (namely f_r, Ma_{max} and ψ) gives insight in the reason for the invariance in performance difference between steady and HB solvers over the different working fluids. The base reduced frequency is defined in equation 2.1. Given that stage geometries do not change over the working fluid variation, clearly the blade chord and pitch remain constant. As a side effect of the balance between the increase in axial velocity and peripheral speed U discussed above, the result is a reduced frequency that is independent of the applied changes in γ. Along with nearly all flow quantities, the Mach numbers encountered in the stage are almost invariant when only changing the working fluid. Seeing as all three parameters hold equally when changing working fluid, the dependence found in the stages with air as an ideal gas is found valid for different working fluids under ideal gas law.

Effect of Flow Non-ideality

Comparing the ideal ($\gamma_{Pv} = \gamma$) MM case to its corresponding non-ideal ($\gamma_{Pv} > \gamma$) setup, a very large difference in results is immediately noticeable. Table 5.3 shows that the non-ideal flow stage is close to seven percent less efficient than the ideal one. Figure 5.10 illustrates the cause of that observation clearly. It shows the Mach number contours for ideal and non-ideal siloxane, obtained by means of steady-state and harmonic balance simulations. The flow phenomena observed in these set-ups are widely different. The results for the ideal MM simulation exhibit Mach numbers that never exceed 0.72. This is in line with the expectations following from the analysis of the results from variation of ideal working fluids in the previous section of the report. The flow field and its physical quantities are close to identical to those of the base *A1* case featuring ideal air, and of any of the working fluids under ideal gas law discussed earlier.

This finding is in sharp contrast with the flow field resulting from the non-ideal simulations at a high value of γ_{Pv} and using the Van der Waals gas law. These show significantly higher Mach numbers, reaching well into the supersonic flow regime at maxima of around Mach 1.5. A normal shock is encountered in the rotor passage, along with oblique shock waves at the trailing edge of the rotor blade. The shocks clearly impact the size and angle of the wake as it sheds off the trailing edge of the rotor blade. Shock and mixing losses will both be significantly higher in the non-ideal $\gamma_{Pv} > \gamma$ case than when resolved with ideal gas assumption. One way of explaining this observation is in the nature of the γ_{Pv} exponent and its role in the relationship between the expansion and volumetric flow ratios. Given the fact that the volumetric flow ratio is constant at 1.34 between the ideal and non-ideal MM setups, the high value of γ_{Pv} in the real gas case results in a significantly higher expansion ratio: 2.4 compared to 1.5 in the ideal gas setup. This expansion ratio translates into higher Mach numbers throughout the domain, which in

Table 5.3: Characteristics of ideal and non-ideal MM in stage *A1*.

Parameter	Ideal	Non-ideal
$\frac{\eta_{TT}-\eta_{TT,Ideal}}{\eta_{TT,Ideal}}$ [%]	n.a.	-6.84
$\frac{\eta_{TT,St}-\eta_{TT,HB}}{\eta_{TT,St}}$ [%]	-0.12	1.22
γ_{Pv} [-]	1.025	3.04
R_v [-]	1.34	1.34
β [-]	1.50	2.41
f_r [-]	4.13	3.52
Ma_{max} [-]	0.71	1.59

turn directly impact the performance figures of the stage. As shown in table 5.3, the non-ideal flow simulation finds a total-to-total stage efficiency that is almost seven percent lower than the efficiency of the same stage if solved using ideal gas models. Strangely, the increase in Mach number is not observed in the stator passage of the stage. In part, the reason for the stark increase in Mach behavior in the rotor has to do with the implications of complex molecules on the peripheral speed, as discussed before in literature [36]. MM needs a lower rotor peripheral speed in order to obtain the same load coefficient and volumetric flow ratio. As a result, the relative Mach number increases more significantly. The difference is a lot less pronounced if one were to look at the absolute Mach numbers throughout the cascade.

The difference in results between the steady-state and harmonic balance solvers is almost non-existent in the ideal MM stage, at 0.1%. This value is in line with the performance differences observed and described for the other ideal working fluids on the high efficiency *A1* stage. The steady-state and harmonic balance solvers deliver much more divergent results at high values of γ_{Pv}, where both methods find results that differ by a little over 1.2%. Performance differences between both solvers of similar or larger magnitudes have been encountered on some of the ideal gas cases only in stages *C2* and *C3*, where flow and especially work coefficients are incomparably higher. The difference between steady and unsteady results in this non-ideal flow simulation is an order of magnitude larger compared to all previous simulations performed on stage *A1*. As already observed earlier in this chapter, high Mach numbers have a significant effect on how closely the steady-state results can match the unsteady ones. Visually, figure 5.10 does not display obvious differences in modeled flow behavior when comparing the steady-state and harmonic balance Mach contours. Other unsteady effects are less present in the non-ideal than in the ideal case, as is expected given the lower reduced frequency that comes with the higher flow velocity.

The large impact of the variation in γ_{Pv} supports its role within the scaling principles. Combining the observations from varying γ and γ_{Pv}, it seems that none of those quantities is by itself a similarity parameter. The ratio between γ_{Pv} and γ is what impacts the flow results and the solver behavior.

5.1.4. Effect of Change in Volumetric Flow Ratio

The final case study in this research concerns the volumetric flow ratio of a turbine stage. The volumetric flow ratio R_v is equivalent to the total-to-static density ratio over the entire turbine stage. As set forward in chapter 4, one additional set of steady-state versus harmonic balance simulations is performed on top of the base $R_v = 1.34$ case studies. This set comprises simulations at a higher volumetric

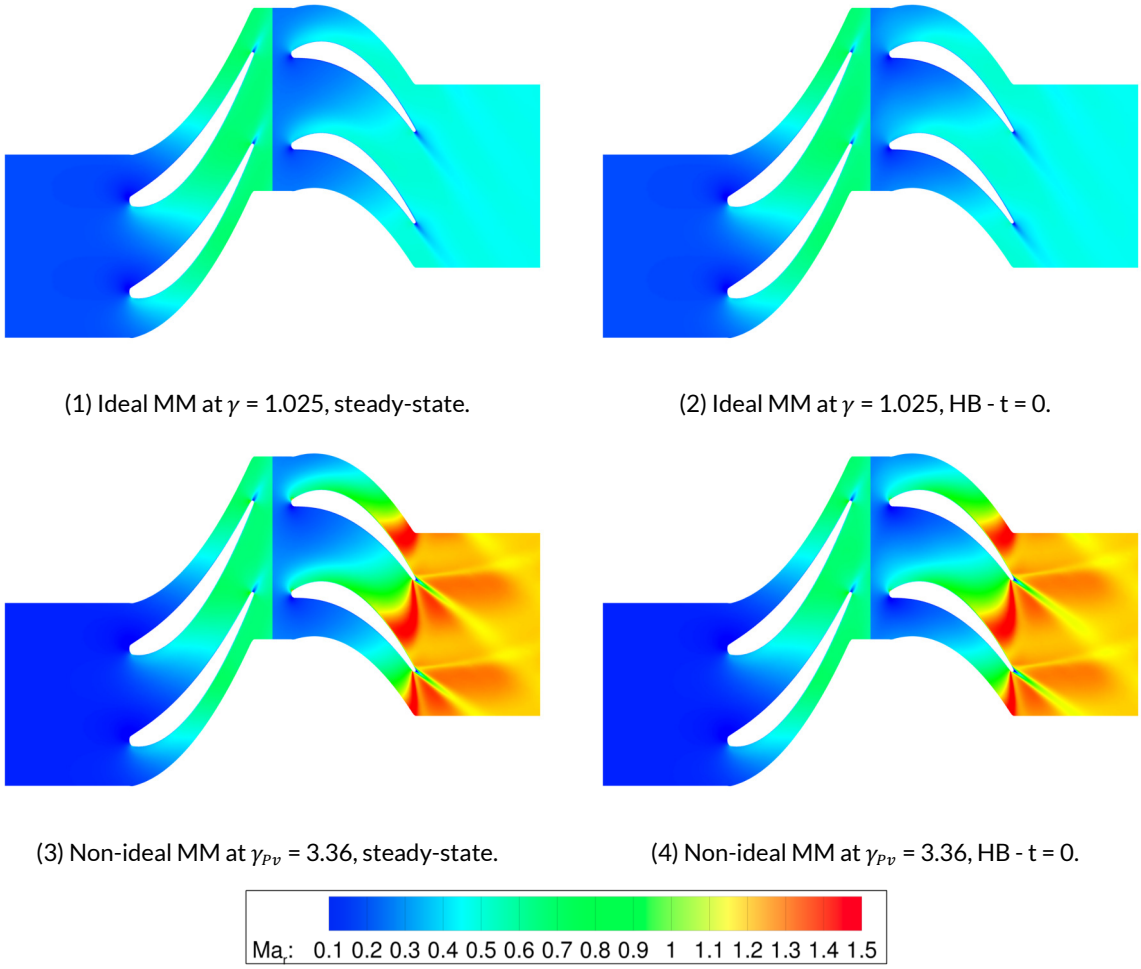

(1) Ideal MM at γ = 1.025, steady-state.

(2) Ideal MM at γ = 1.025, HB - t = 0.

(3) Non-ideal MM at γ_{Pv} = 3.36, steady-state.

(4) Non-ideal MM at γ_{Pv} = 3.36, HB - t = 0.

Figure 5.10: Relative Mach contours of stage *A1*.

flow ratio, namely $R_v = 2$ on the highest efficiency *A1* stage ($\phi = 0.55, \psi = 1.1$).

Table 5.4 shows the main results of the comparison between the base and increased volumetric flow ratio simulations, using air as working medium. The data shows that the total-to-total efficiency of the stage is higher by 0.76% when operating at the higher volumetric flow ratio. This finding is at odds with the image presented by the flow field of the high volumetric flow ratio simulation. The relative Mach contours are shown in figure 5.11. Clearly, increasing the volumetric flow ratio results in significant increases in flow velocity, as would be expected. Mach numbers as high as 1.1 are reached, with a shock clearly showing at the aft end of the suction surface of the rotor blade. Previous research would also suggest a decrease in efficiency due to shock losses when increasing the volumetric flow ratio. In conclusion, while the flow field matches the expectations, some of the stage characteristics do not. It may be possible that boundary layer and mixing losses are decreased due to the high flow velocity, countering the increased shock losses. This hypothesis is hard to verify with the information available within the scope of this project, and would require work on more accurate quantification of the different loss coefficients of these stages.

It is also clear from the data that the results of the steady-state and harmonic balance solver lie closer together at the higher volumetric flow ratio than in the baseline geometry. The higher volumetric flow ratio increases the flow velocity through the turbine stage. This is reflected in the reduced frequency value, which is more than ten percent lower compared to the base *A1* stage. Concretely, less

Table 5.4: Characteristics of different volumetric flow ratios in stage *A1*.

Parameter		Base	High R_v
R_v	[-]	1.34	2.0
$\eta_{TT,HB}$	[%]	95.71	96.66
$\frac{\eta_{TT}-\eta_{TT,Base}}{\eta_{TT,Base}}$	[%]	n.a.	0.76
$\frac{\eta_{TT,St}-\eta_{TT,HB}}{\eta_{TT,St}}$	[%]	0.32	0.15
f_{red}	[-]	4.23	3.79
Ma_{max}	[-]	0.70	1.15

unsteady behavior is present at the higher density ratio, allowing the steady-state solver to obtain a result closer to the one achieved by the harmonic balance evaluation. This behavior has been observed previously in this research. This further reinforces the hypothesis that the case with the higher volumetric flow ratio experiences less unsteady effects, as these mechanisms are tightly intertwined with loss generation.

The other main parameter affecting the performance of both solvers is the Mach number. As discussed above, this is where the results present a challenge to the reasoning. The same hypothesis as advanced when discussing the efficiency by itself may solve the issue. The behavior might be explained if the Mach number obtained at $R_v = 2$ is sufficiently low - even if by a slight margin - to avoid having a profound impact such that the effect of the decreased reduced frequency is dominant. Increasing the volumetric flow ratio is therefore expected to decrease the advantage of using an harmonic balance solver over a steady-state one up to a certain point at which the Mach number effect takes over and drives up the differences again. It would be interesting to extend research to testing an even higher volumetric flow ratio, and to find where the turning point lies. In order to investigate the validity of the results, the $R_V = 2$ simulations have been extended to cover the other four ideal working fluids on stage *A1* as well as ideal air on geometries *B1* and *B2*. All of the results are consistent with what is observed in the base *A1* case discussed in this section, namely higher efficiencies and smaller performance differences at the higher volumetric flow ratio.

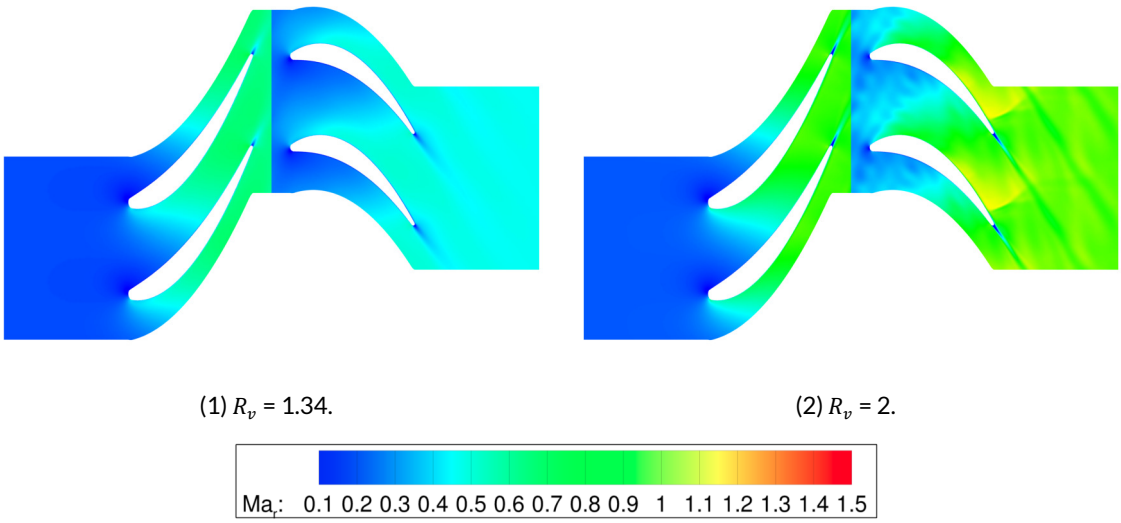

(1) R_v = 1.34. (2) R_v = 2.

Figure 5.11: Relative Mach contours of stage *A1*, HB - t =0.

5.2. Optimization

The objective of this thesis research is in providing best practices for shape optimization regarding flow solver selection. Due to the long computational times associated with optimizations, flow simulations have formed the backbone of the data generation. In order to verify whether the trends observed in the simulation results hold in an optimization environment, two particular case studies have been extended towards an optimization context. In this section of the report, the results of the optimization cases are presented and discussed in further detail. After a gradient validation, the base *A1* case will be discussed in section 5.2.2. Subsequently, the shape optimization of stage *B1* is discussed in section 5.2.3.

5.2.1. Gradient Validation

In the gradient validation process, the total gradients of the objective function with respect to the design variables as calculated by the discrete adjoint (AD) solver are compared to those found using a finite difference (FD) method. This step is a crucial precedent to the shape optimization process, and exists in order to confirm the validity of the adjoint solver and its results. The gradients found using FD are considered to represent the exact values. Therefore, in an ideal case, the gradients resulting from the adjoint solver will match their FD counterparts. In reality, numerical errors among other causes result in inherent deviations in both FD and AD results, so small differences are commonplace and to be expected. Finite difference methods rely on perturbing each element of the design vector - FFD control points in the case of this research - in order to find the objective function response to this change. Unlike adjoint methods, the computational time corresponding to finite difference evaluation is therefore dependent on the number of design variables. This has earlier been mentioned to be one of the main advantages of the adjoint method. This gradient validation will also provide a tangible illustration of this improvement in computational requirements. For the sake of computational efficiency, only the eight outside control points are taken into account, as opposed to the full 84. This is not expected to influence the conclusion of the validation. Figure 5.12 shows the results of the gradient validation performed on stage *A1* in the *turbo_ffd* branch of *SU2*. Both subfigures represent the same results in different ways. In 5.121, the gradients retrieved from both finite difference and adjoint solvers are shown in function of the design variables. Figure 5.122 shows the data points with both the FD and AD gradients. In an ideal case, all points lie on the $y = x$ diagonal.

The results show a good match between the adjoint and finite difference results overall. A clear observation during the process is the extreme sensitivity of the FD gradients depending on the finite difference step selected for the evaluation. The value of $1 \cdot 10^{-3}$ was deemed the best out of several tries and the results obtained by using it are the ones show in these figures. The last half of the design variables seem to yield larger differences in the found gradients. Given that these first four points are associated with the control points of the rotor blade, the results suggest larger discrepancies in the rotor than in the stator row. In particular, two control points give rather large differences in the calculated sensitivity. These control points correspond to the leading edge and trailing edge control points. In these regions, sensitivities are large and it is more difficult to correctly capture the gradients. While less pronounced, the trailing edge control point in the stator blade is also the one displaying the largest discrepancy between the adjoint and finite difference sensitivity. Figure 5.13 shows the adjoint s_{gen} gradients along the blade surfaces of the *A1* stage. It clearly confirms the relative sensitivity of the trailing edge region. Additionally, the figure shows the presence of relatively higher sensitivities around the leading edge and suction side of the blades. The gradient validation is deemed acceptable for the purpose of this research.

Finally, the gradient validation process underlines very clearly the advantage of opting to use an

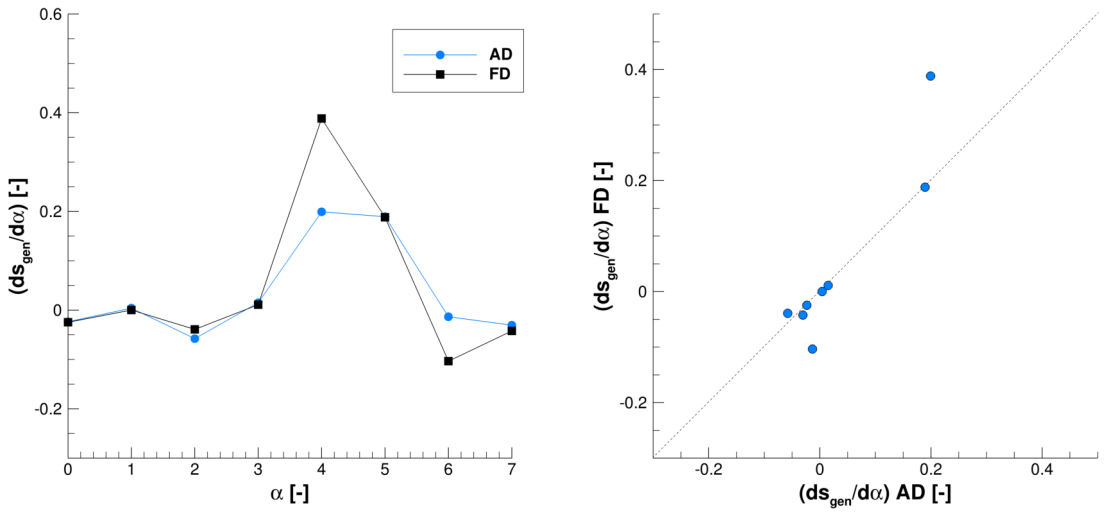

(1) Entropy gradients in function of design variable. (2) FD entropy gradients in function of AD gradients.

Figure 5.12: Gradient validation.

adjoint solver as opposed to a finite difference or similar method of determining the gradients. Altogether, the flow and adjoint evaluation in steady-state took approximately one hour to complete. The finite difference solver took more than four times longer for this particular case. In the eventual optimization cases, there will be 84 design variables given the subdivision of the FFD boxes. This would translate in a finite difference evaluation time of approximately 45 hours. Given the added fact that an optimization loop requires several dozens of gradient evaluations, the adjoint method offers enormous computational gains to the optimizations in this research and beyond.

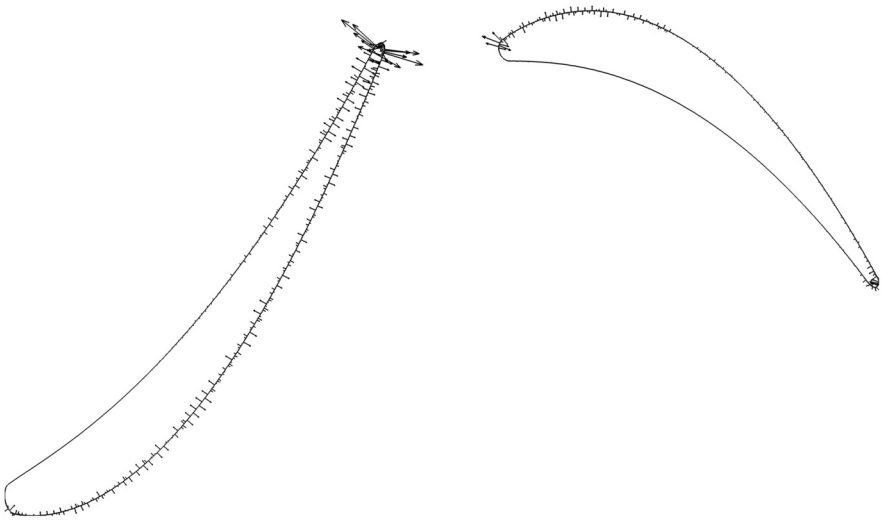

Figure 5.13: Adjoint surface sensitivity vectors.

5.2.2. Optimization Case 1: Stage A1 Operating with Air

As set out in chapter 4, this first optimization case study represents a baseline reference stage. It consists of the *A1* geometry ($\phi = 0.55, \psi = 1.1$) operating at a volumetric flow ratio of 1.34 with air as working fluid. Shape optimizations are performed using both the steady-state solver in the *feature_turbo_ffd* branch and the harmonic balance unsteady solver in the *feature_TMZHB_temp* branch of *SU2*.

Figure 5.14 shows the design history of both the steady-state and harmonic balance shape optimizations. The course of both optimization processes is clearly similar in nature. Small entropy reductions are realized over the first few design steps. Subsequently, a large gain is achieved at the 7th/8th and 7th/8th/9th design steps of the steady and harmonic balance optimization, respectively. The final design steps again only yield small improvements. The large change in the objective function corresponds to a major remeshing operation of the stage geometry. Both simulations were limited to a maximum of twenty design steps. Given the immense computational cost and the streak of minimal improvements, the harmonic balance optimization was stopped after eighteen design iteration. It is important to note that a design step does not directly correspond to a flow and adjoint evaluation. More often than not, multiple designs and respective evaluations constitute one design step. The total number of flow/adjoint evaluations is 101 and 67 for the steady-state and harmonic balance optimization. The respective computational times for both optimizations are 58.99 hours (2.5 days) and 376.31 hours (16 days). The runtimes of these shape optimizations are a reiteration of why the research pursued in this thesis work is of importance. While significantly faster than full time-unsteady methods, the harmonic balance optimization in this example still takes more than six times longer than the equivalent steady-state based optimization. Accounting for the fact that the steady-state optimization is left running for two more design steps, the ratio in computational times on equal footing would be in the range of 7.5 to 1. It is therefore important to establish for which cases the results are worth that increased computational investment.

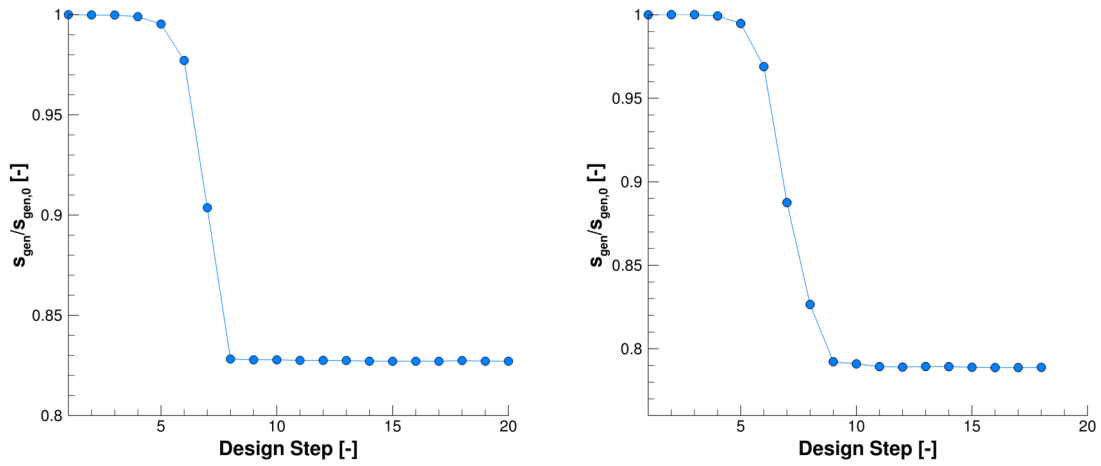

(1) Steady-state.

(2) Harmonic balance.

Figure 5.14: Optimization history of stage *A1* with air as ideal gas.

The main characteristics of the baseline and optimized stages are presented in table 5.5. Note that these performance figures are calculated with their respective solvers, and so the efficiencies of the optimized stages as shown here are not to be compared in absolute terms. Rather, the table shows the relative improvement over both processes. Both efficiency and entropy generation improvements are slightly larger for the harmonic balance optimization. The harmonic balance figures are averaged over time, and so do not show the full picture. The total-to-total efficiency of the baseline and optimized stages, both

for the steady and HB cases over the blade passing period are shown in figure 5.15. Clearly, not only does the average efficiency increase over the course of the harmonic balance optimization, but its amplitude changes as well. This leads to believe that the optimization damps out some of the major sources of unsteadiness, making the efficiency (and other flow parameters by extension) less time variant.

Table 5.5: Optimization results for stage *A1*.

Geometry	s_{gen} [J/K]	$\Delta s_{gen}/s_{gen,MP}$ [%]	η_{TT} [%]	$\Delta\eta_{TT}/\eta_{TT,MP}$ [%]
Baseline MP	0.01985	n.a.	96.04	n.a.
Optimized MP	0.01641	-17.33	96.67	+0.66
Baseline HB	0.02079	n.a.	95.71	n.a.
Optimized HB	0.01640	-21.11	96.81	+1.15

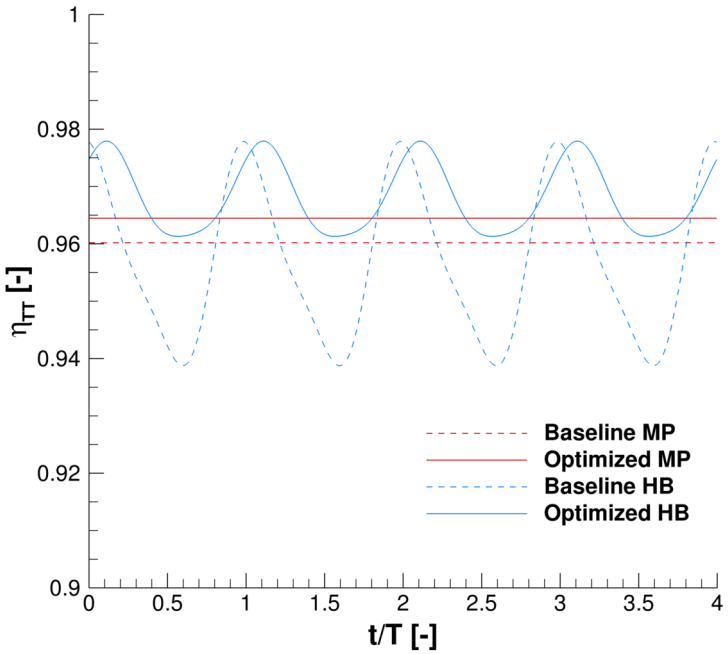

Figure 5.15: Total-to-total efficiency of baseline and optimized blade shapes of stage *A1* in function of time.

Figure 5.16 shows the optimized blade geometries resulting from the steady-state mixing plane (MP) and harmonic balance optimization processes. The shape changes are clearly visible. The mixing plane and harmonic balance optimized blades share some features, while clearly differing in other areas. Overall, the steady-optimized blade resembles the original shape more closely.

In the stator row, the optimized shapes clearly indicate a tendency of the optimizer to reduce the thickness of the airfoil. Both the MP- and HB-optimized airfoils - but especially the latter - are notably thinner and flatter along the suction side of the blade. The physical consequence of this operation is clearly visible in figures 5.17 and 5.18. In figure 5.17, the relative Mach flow field of the baseline and optimized stages in both steady-state and harmonic balance are shown. A major change is visible in the flow throughout the stator channel. Locally flattening the blade significantly delays the high-Mach region and lowers the Mach numbers encountered over the suction side of the airfoil overall. Investigating in further detail, figure 5.18 plots the isentropic Mach number in function of the normalized

stator chord length. Clearly, Mach numbers are lower in the optimized blades. Regions with relatively low Mach numbers show less physical shape change as well as less deviation in the Ma_{is} plot. The higher Mach regions along the suction side of the stator blade and the back of the pressure side are where the majority of the surface displacement is found. Consequently, the isentropic Mach surface plots show larger decreases there. The overall decrease is more extreme in the harmonic balance optimized stator.

There is a distinct and fundamental difference in the shape modification between the optimization in the steady and unsteady branch of *SU2*. This is clear both from the final geometry and its effect on the flow field. The steady-state optimized blade is thinner than the original one, but generally retains the same shape and proportions. The harmonic balance optimized stator shape is more locally flattened. This is clearly observable in figure 5.17. The MP-optimized stator cascase shows a rather uniform decrease in Mach numbers. The blade resulting from the HB optimization in 5.174 yields a more fundamentally changed flow field, delaying the high Mach region. One could say that the 'design philosophy' behind both optimization processes differs.

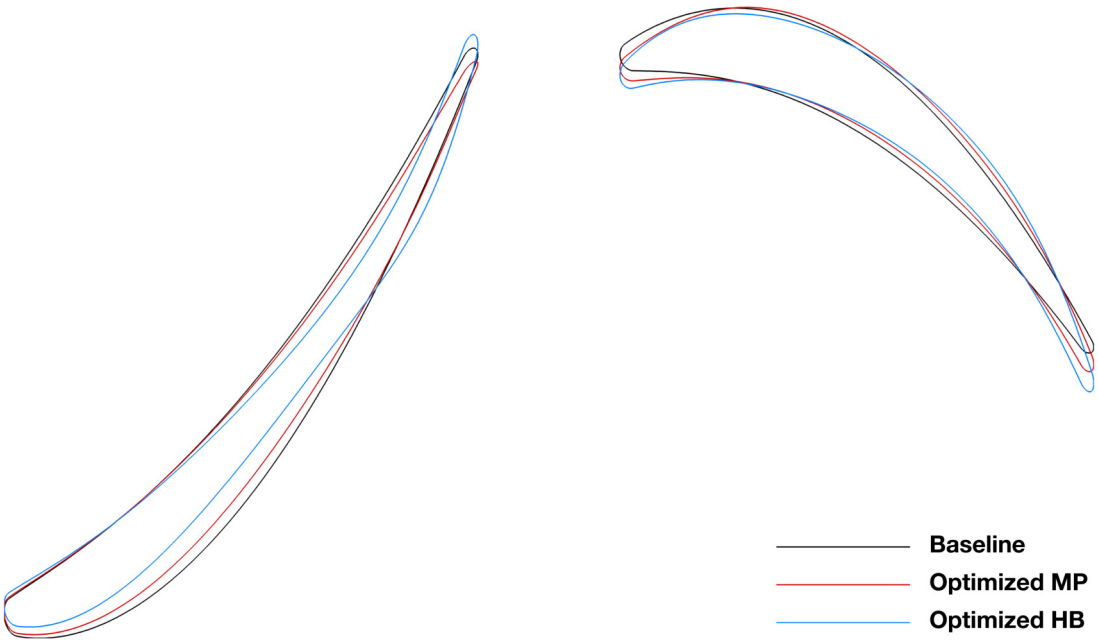

Figure 5.16: Baseline versus optimized blade shapes of stage *A1* with air as ideal gas.

This observation is supported by another aspect of the stator geometry. A second impact on the shape of the stator blade is namely the increase in camber at the trailing edge of the blade in the harmonic balance optimized blade. Once again, the main instigator of this evolution seems to be the Mach numbers throughout the stator throat. The throat is locally widened before the trailing edge of the blade. The curvature at the end of a blade serves a second purpose, however. While flattening the suction side of the blade to decrease Mach numbers aids in decreasing losses, the loss of camber decreases the work done by the blade. This is resolved by adding more curvature at the upper trailing edge. The effect is visible in the isentropic Mach plot in figure 5.182, where clearly there is a plateau in the Mach number over a large part of the suction side of the stator blade, after which significant acceleration of the flow occurs towards the trailing edge. This evolution in the camber line and trailing edge is completely absent in the steady-state optimized stator blade. This divergence in the way the stage geometries are altered over both optimization processes strongly points at the impact of unsteady effects on the solver performance.

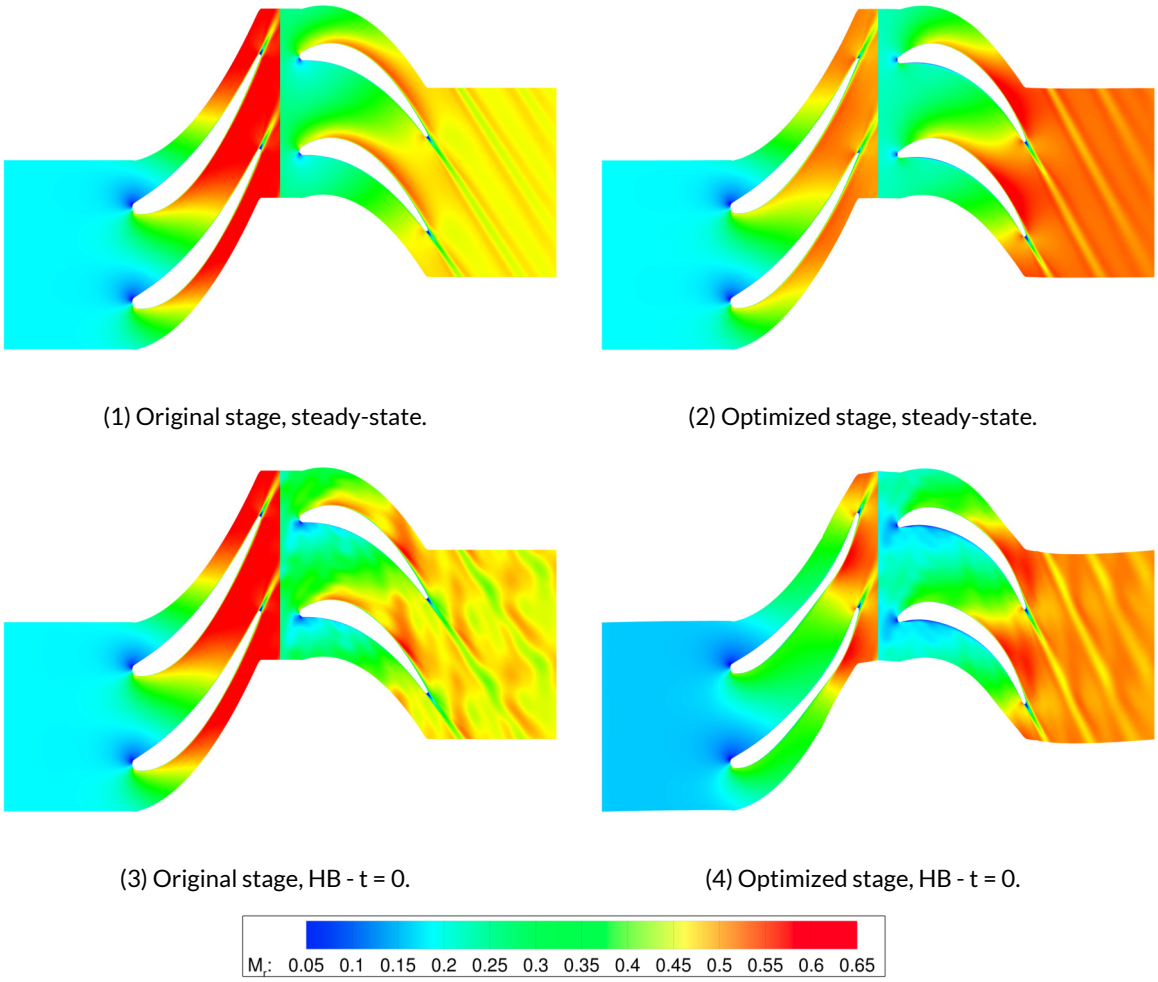

(1) Original stage, steady-state.

(2) Optimized stage, steady-state.

(3) Original stage, HB - t = 0.

(4) Optimized stage, HB - t = 0.

Figure 5.17: Relative Mach contours of stage *A1*.

Another interesting point arises when looking at the pressure distribution along the stator blade. Figure 5.18 can be considered the inverse plot of the pressure coefficient C_P along the surface of the baseline and optimized blade shapes. The shape of the distribution of the HB-optimized stator blade stands out due to its resemblance with the distribution associated with supercritical airfoils in aircraft wings. Just like in these supercritical airfoils, the optimizer aims to delay the onset of wave drag at transonic Mach numbers. Another shared characteristic is the increase of camber at the trailing edge to account for lost lift/work. This resemblance boosts confidence in the optimization procedure performed in this thesis work, as the results clearly move towards a previously known concept within the field. The difference with the steady-state optimized blade and the way its shape is deformed is clear once again when comparing these pressure distributions. The differences in C_P are more gradual and linear in the case of the steady optimizer, and closer to the general distribution of the original *A1* stator blade. Overall, the way in which the physical blade shape is perturbed is reflected nicely in the pressure distributions.

In the rotor row, the changes to the blade shape are significant but different in nature to what has been observed in the upstream stator blades. A clear step the optimizer has taken is to drop the leading edge of the blade - or increase the curvature at the leading edge. As can be seen in figure 5.17, this is most likely done to better match the incidence angle of the inflow and better position the stagnation point.

The final major change throughout the optimization processes is the increase of curvature in the

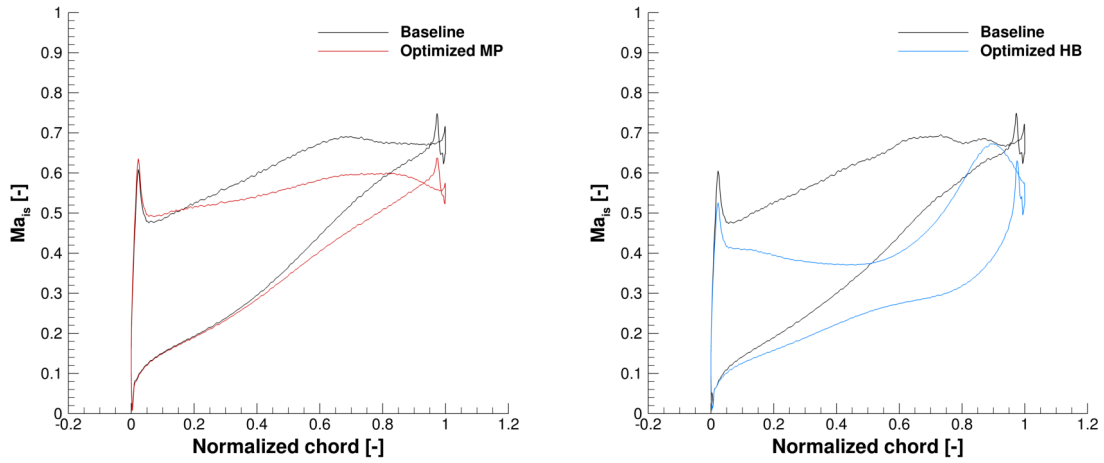

(1) Steady-state.

(2) Harmonic balance - t = 0.

Figure 5.18: Isentropic Mach over stator chord of stage *A1* with air as ideal gas.

trailing edge of the rotor blade. The outflow angle has been increased quite significantly, as can also be seen in the angle of the wake in the entropy countours in figure 5.19. The result of the overall increase in curvature over the rotor blade, and especially of the drop of the trailing edge which decreases the local throat area, is that Mach numbers in the rotor passage are higher than in the initial baseline case. This can clearly be observed in figure 5.17.

Figure 5.19 shows the entropy contours for the baseline and optimized cases, both from the steady-state mixing plane and harmonic balance unsteady optimization processes. In both cases, the entropy contours are noticeably less pronounced in the optimized stage cascade. This is especially true for the harmonic balance case, where, because of the visibility of wake interaction, the behavior can be seen much more clearly. The decrease in Mach effects likely positively affects mixing losses at the outflow of the stator cascade.

Table 5.6: Optimization results for stage *A1*.

Geometry	$\eta_{TT,HB}$ [%]	$\frac{\Delta\eta_{TT}}{\eta_{TT,MPopt}}$ [%]
Optimized MP	96.18	n.a.
Optimized HB	96.73	+0.58

The values presented in table 5.5 are not representative for comparing the actual effect of the flow solver on the final result of a design optimization process. For that purpose, and in the context of setting up design guidelines, the total-to-total efficiency of both MP- and HB-optimized stages is to be determined in an equal and accurate way. This is achieved with an additional 7 time-instance harmonic balance flow evaluation of both optimized blade cascades, as proposed in chapter 4. The efficiencies of the optimized *A1* stages are presented in table 5.6. The efficiency of the HB-optimized stage is found to be 0.55 percentage points higher, an increase in efficiency of 0.58% compared to the MP-optimized stage. This value is higher than the 0.32% difference found between the MP and HB results form the primal flow solver. This difference implies that the discrepancy within the flow simulation step propagates and increases over the course of a full shape optimization. This is rather believable, given the large amount of flow evaluations that make up the optimization process.

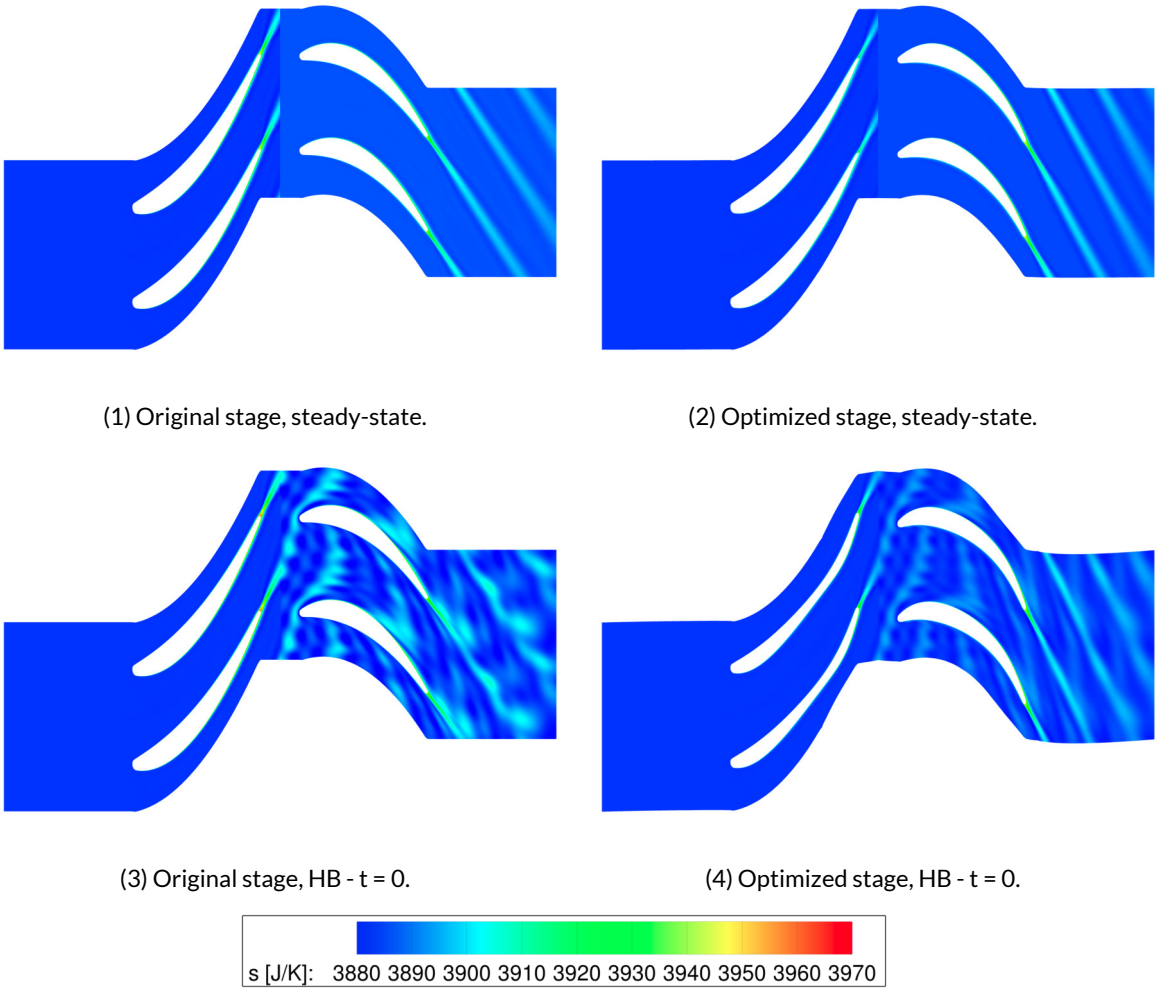

(1) Original stage, steady-state.

(2) Optimized stage, steady-state.

(3) Original stage, HB - t = 0.

(4) Optimized stage, HB - t = 0.

Figure 5.19: Entropy contours of stage *A1*.

5.2.3. Optimization Case 2: Stage B1 Operating with Air

The second optimization case uses the *B1* geometry ($\phi = 0.55, \psi = 1.65$) as its starting point. This way, the effect of an increase in work coefficient on the optimization results from the MP and HB solvers can be observed independently. Just as in the previous shape optimization, air is the working medium of choice, and the stage operates at R_v equal to 1.34.

The design history of the MP and HB-based optimizations is shown in figure 5.20. In both cases, the optimization process converged after eight design steps, reaching the lower limit in gradient size. The steady-state and HB optimization went through 20 and 23 flow/adjoint evaluations, respectively. The corresponding computational times are 10.77 hours and 120.13 hours (5 days). The HB optimization took 11 times longer to reach convergence than the equivalent MP process.

The main baseline and optimized characteristics are presented in table 5.7. These performance figures are calculated with their respective solvers, and so the efficiencies of the optimized stages as shown here should not to be compared in absolute terms. This data suggests a larger improvement in both entropy generation and total-to-total efficiency over the harmonic balance optimization process. Just as in the optimization of stage *A1*, this is likely due to the fact that the unsteady loss mechanisms are less present in the steady-state case to begin with, and that there is consequently less to improve on.

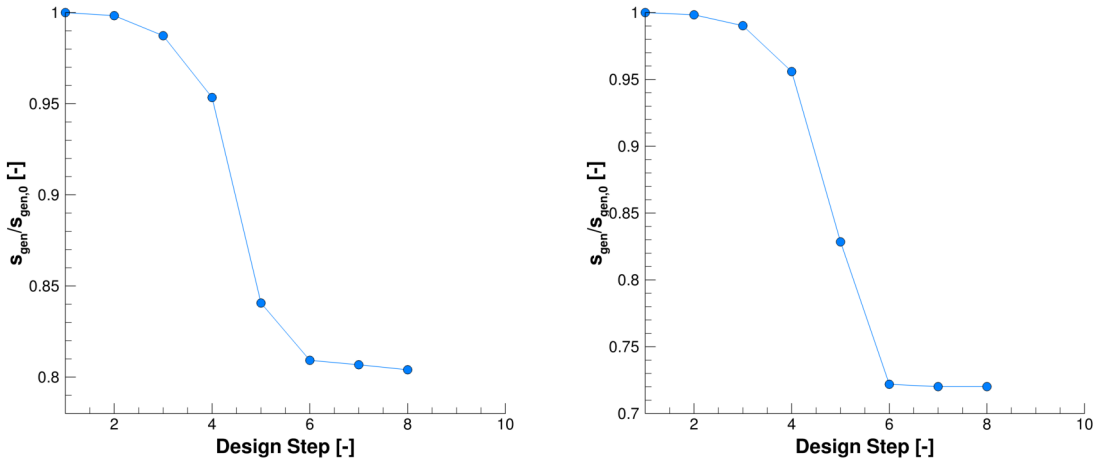

(1) Steady-state.

(2) Harmonic balance.

Figure 5.20: Optimization history of stage *B1* with air as ideal gas.

Table 5.7: Optimization results for stage *B1*.

Geometry	s_{gen} [J/K]	$\Delta s_{gen}/s_{gen,MP}$ [%]	η_{TT} [%]	$\Delta\eta_{TT}/\eta_{TT,MP}$ [%]
Baseline MP	0.02348	n.a.	95.57	n.a.
Optimized MP	0.01888	-19.59	96.21	+0.67
Baseline HB	0.02565	n.a.	95.07	n.a.
Optimized HB	0.01847	-27.99	96.24	+1.23

The optimized blade shapes are shown against the baseline *B1* stage geometry in figure 5.21. Both MP- and HB-optimized blades are rather similar to the original blade in terms of general size and proportions. This is in contrast with the optimization of stage *A1*, where the harmonic balance optimization resulted in a distinctly different geometry - particularly clear in the stator blade. Like for the *A1* case, the shape of the HB-optimized *B1* stage, across the board, is differs more from the baseline shape than the shape resulting from the steady-state optimization. This is especially true for the deformation of the stator blade.

Just like in the optimization of stage *A1*, the most obvious change to the stage geometry over both MP and HB optimization processes is to the thickness of the stator blade. Figure 5.21 clearly shows this deformation. The thickness reduction manifests itself in the form of a flattening on the suction side of the stator blade. The change in thickness is more pronounced in the HB-optimized stator blade. The results of this shape change are clear in the Mach contours displayed in figure 5.22. Both optimization processes result in flow fields with significantly lower flow velocities throughout the stator throat. The thinner HB-optimized stator makes for even lower flow velocities than in the equivalent MP-optimized stator cascade. Mach numbers in the throat are decreased by up to 0.15 after the MP optimization and 0.2 for the harmonic balance method. The isentropic Mach plots of the stator blades in figure 5.23 clearly support that conclusion. The flattening on the blade's suction surface yields a decrease in Mach numbers from x/b = 0.2 onwards. Unlike in the HB-optimized *A1* stage, the shape of the Ma_{is}/C_p distribution is not fundamentally different. This was already expected from the more uniform deformation of the blade shape. The result of the lower Mach numbers in the stator is a higher relative Mach number at the rotor outlet, however. The optimizer favors improvement in the stator flow field over the rotor flow

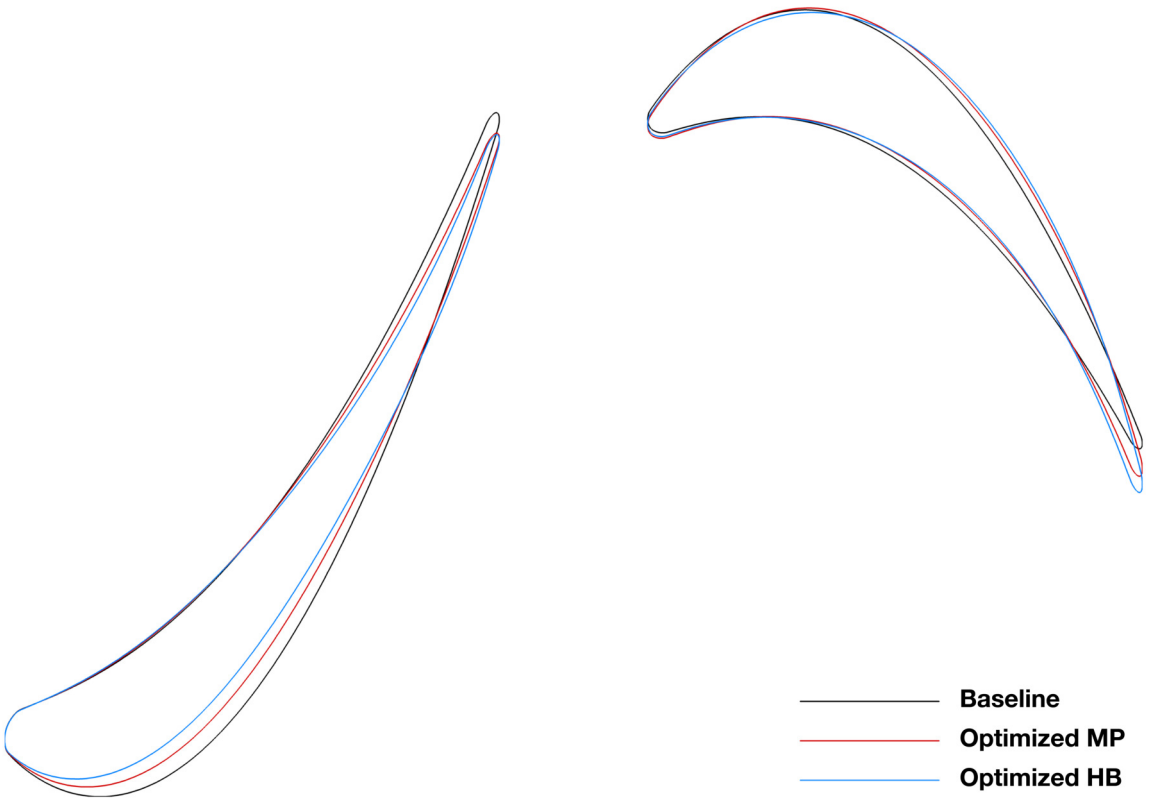

Figure 5.21: Baseline versus optimized blade shapes of stage *B1* with air as ideal gas.

field given the downstream propagation of unsteadiness and the interaction of the rotor blade with the static pressure disturbance caused by the stator.

Both optimized stages show a slight straightening of the stator trailing edge. Effectively, the outlet flow angle is decreased, as is clear from the entropy contours in figure 5.24. The opposite is true in the rotor, where the curvature of the blade and therefore the flow outlet angle is increased over the course of the optimization. This last feature is also contributing to the higher flow Mach numbers. Effectively, the degree of reaction is larger in the optimized blades. Calculating the corresponding values confirms this observation. The degree of reaction of the stage goes up from 0.33 to 0.62 over the course of the steady optimization, and reaches up to 0.7 in the HB-optimized stage.

The rotor blade shape overall is not modified as significantly as the stator blade. Especially the leading edge region, and up to around a third of the chord is virtually unaltered compared to the baseline *B1* stage. In line with the dropped trailing edge, the curvature along the aft half of the blade is increased, adding to the effect on flow turning over the rotor.

Finally, as for the *A1* optimization case, it is imperative to compare the efficiency of the MP- and HB-optimized cases on equal footing. Again, this is achieved by means of a higher fidelity, 7 time instance harmonic balance flow simulation on both optimized stages. Their resulting total-to-total efficiencies are displayed in table 5.8. Once again, the HB-optimized stage boasts a higher efficiency than the turbine cascade optimized by means of the steady-state solver.

Contrary to what would be expected from the simulation results discussed in the previous section, the difference between MP- and HB-optimized stages is smaller for the *B1* case than for *A1*. The set of two optimizations is too small to really confirm or debunk the validity of the simulation results in section

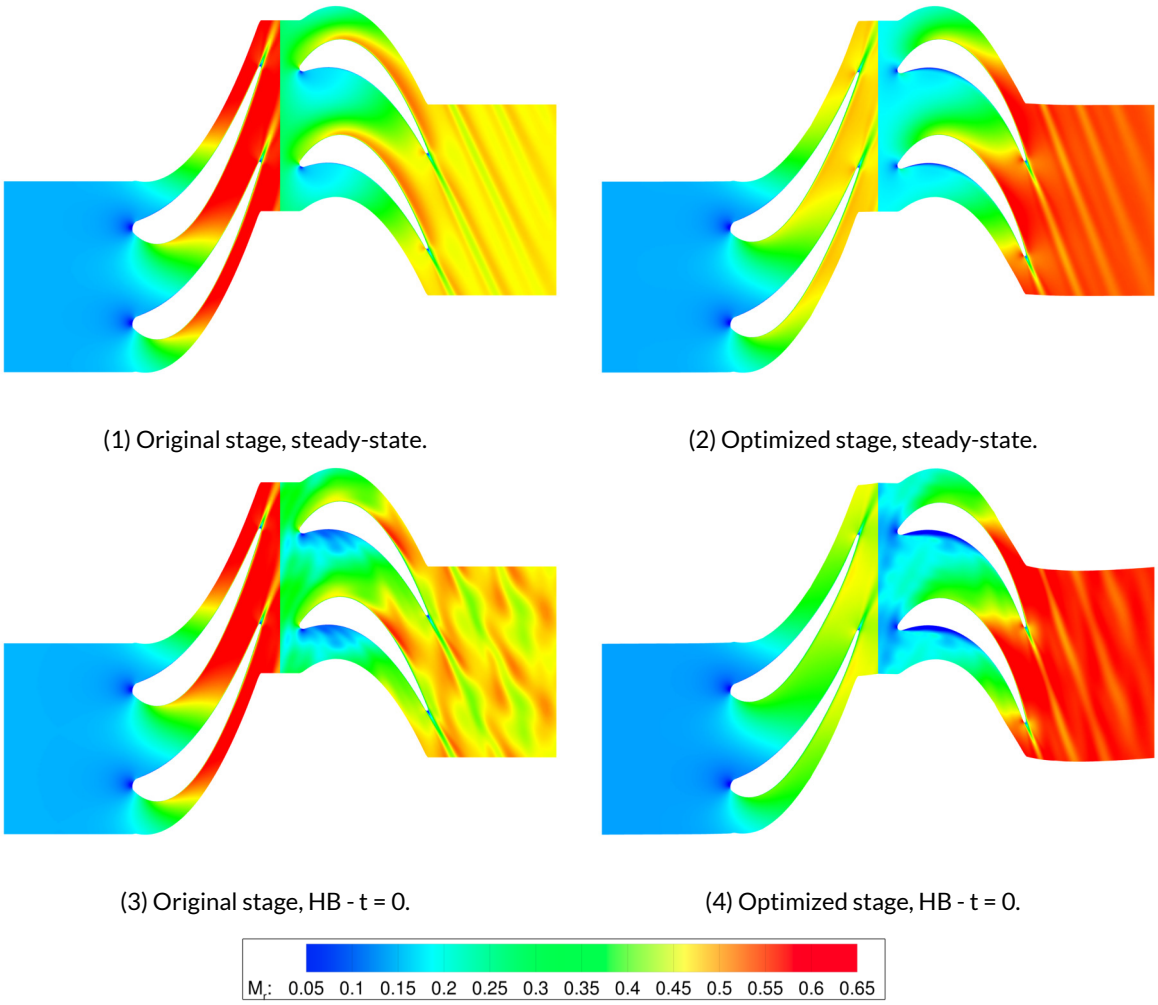

(1) Original stage, steady-state.

(2) Optimized stage, steady-state.

(3) Original stage, HB - t = 0.

(4) Optimized stage, HB - t = 0.

Figure 5.22: Relative Mach contours of stage *B1*.

Table 5.8: Optimization results for stage *B1*.

Geometry	$\eta_{TT,HB}$ [%]	$\frac{\Delta\eta_{TT}}{\eta_{TT,MPopt}}$ [%]
Optimized MP	95.94	n.a.
Optimized HB	96.06	+0.12

5.1 in an optimization. More shape optimizations are required to come to a valid conclusion on this matter. Additionally, the selected optimization cases are both not at extremes of the design space. The trends observed in the simulation cases will most likely be reflected more strongly in geometry *C3* or for a high γ_{Pv} non-ideal fluid case. Once again, further investigation would be needed to shed light on those particular cases. Overall, the difference between the MP- and HB-optimized stage efficiency for both the *A1* and *B1* cases is small. These results highlight the remarkable accuracy achieved with - what effectively non-physical - MP flow solvers.

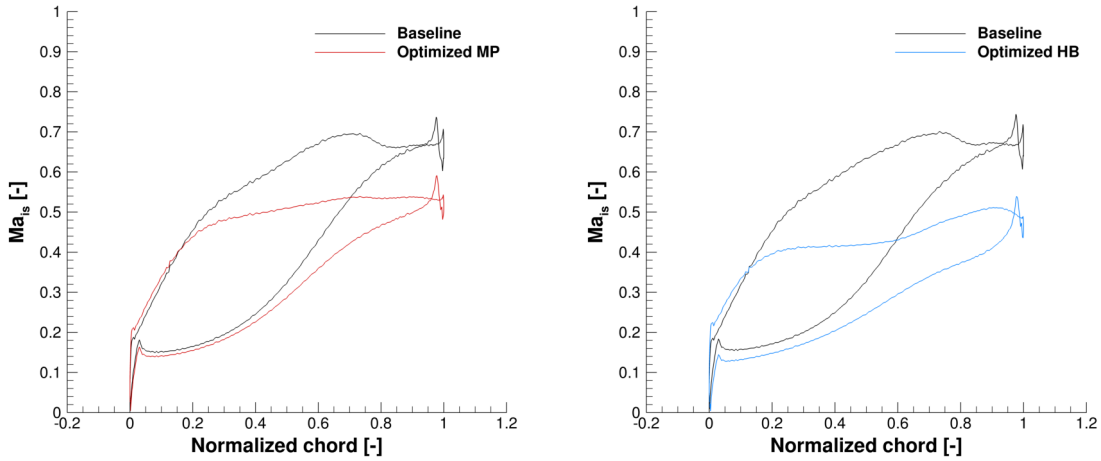

(1) Steady-state. (2) Harmonic balance - t = 0.

Figure 5.23: Isentropic Mach over stator chord of stage *B1* with air as ideal gas.

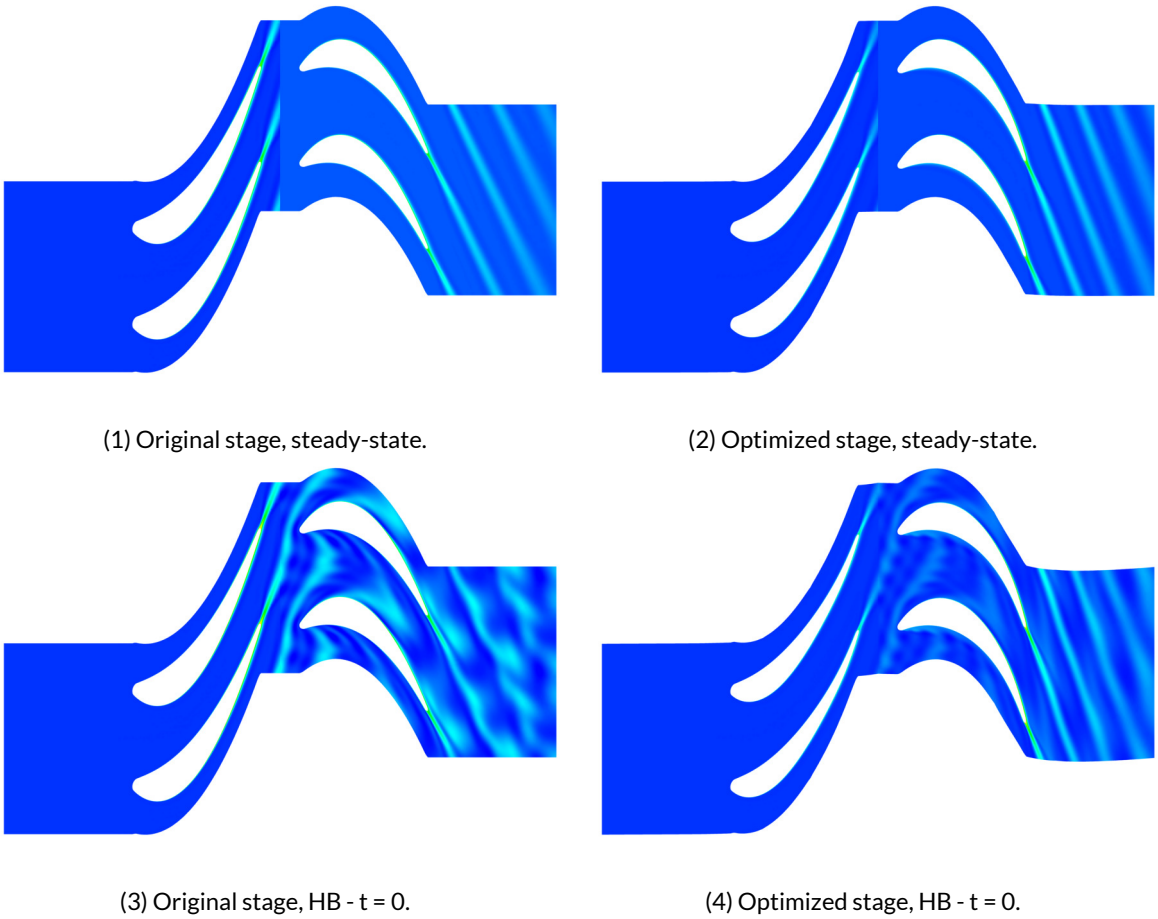

(1) Original stage, steady-state. (2) Optimized stage, steady-state.

(3) Original stage, HB - t = 0. (4) Optimized stage, HB - t = 0.

Figure 5.24: Entropy contours of stage *B1*.

5.3. Guidelines for Design Optimization

In this section of the report, the data and insight obtained over the more than 96 flow simulations and two full shape optimizations performed are translated into design guidelines that provide indications about the most appropriate flow model for the analysis and design of turbine stages operating with ideal and non-ideal compressible flows.

The effect of five main stage characteristics has been studied over the course of many simulations, with the focus on the difference between results obtained by a steady-state and harmonic balance unsteady flow solver. These are the flow coefficient ϕ, work coefficient ψ, working fluid on the basis of γ, non-ideality represented by γ_{Pv} and volumetric flow ratio R_v. Throughout section 5.1, it is found that the behavior of the flow solvers is indeed subject to changes associated with variation in these characteristics. This correlation does not equate to causation: the five parameters are not the base physical cause behind the deviation in solver results. Therefore, a relationship or design guideline based on these five would not be productive nor intuitive. The goal is to identify the underlying base parameters indicating the flow characteristics responsible for the deviant behavior between steady and HB solvers. That way, the resulting indicator parameters can also be applied to design cases with different nondimensional groups or governing parameters. The combination of the following three main stage and flow characteristics - previously discussed in 5.1 - has been found to fulfill that aim. They together result in a single indicator of difference between steady and HB solver performance.

- The reduced frequency, f_r, as defined in equation 2.1, is considered the basis for this new indicator. It physically represents the ratio between the unsteady and dissipative behavior of the flow. Despite its purpose as a main indicator of unsteadiness, the results in section 5.1 show that the reduced frequency fails to predict the difference between steady-state and HB results by itself. In order to obtain a valid design guideline, the reduced frequency is corrected or adjusted to cover a wider scale of unsteady flow phenomena. In this light, the newly composed parameter is referred to as the adjusted reduced frequency. The contribution of f_r to the adjusted reduced frequency lies mostly in the prediction of wake and pressure field interaction. Given the relation between reduced frequency and flow coefficient shown in equation 2.1 and the invariance of solidity over all test cases in this research, substituting f_r by the inverse of the flow coefficient would fulfill the same role. However, for the sake of finding the most broadly applicable relation, the reduced frequency as a whole is deemed relevant. This way, effect of both flow coefficient and stage solidity are represented within the adjusted reduced frequency.

- Ma_{max} is the maximum relative Mach number measured in the stage domain. Its purpose within the adjusted reduced frequency parameter is to factor in the shock effects that are present within the turbine stage. Mach effects are not (sufficiently) covered by the reduced frequency alone, as is clear from the flow simulations in section 5.1.

- Finally, the work coefficient ψ completes the list of contributors to $f_{r,adj}$. Its purpose is to adjust the parameter with respect to the effect of the static pressure field disturbance caused by the stator row, and its subsequent interaction with the downstream rotor blades. As discussed in section 5.1, this effect is thought not to be sufficiently captured by the reduced frequency.

These three quantities - representing the degree of unsteadiness, compressibility effects and blade loading respectively - have together been found to result in a parameter that is in a linear dependency with the total-to-total efficiency difference between the steady and harmonic balance solver. The following relation for such adjusted reduced frequency $f_{r,adj}$ has been empirically deduced based on the results of the case studies.

$$f_{r,adj} = f_r \cdot \psi \cdot Ma_{max}^{1.1} \tag{5.2}$$

The found relation is remarkably straightforward, simply multiplying the three governing parameters. The Mach number is assigned an exponent of 1.1. This way, supersonic Mach numbers are disproportionally penalized in terms of their performance impact, while the effect of subsonic Mach numbers is toned down. The exponent's value close to one makes its effect rather subtle.

Applying the relation to the different flow simulation cases performed and described in section 5.1 results in the plot shown in figure 5.25. The results show that:

- The relation holds when varying flow and work coefficient.
- Different values of the volumetric flow ratio are covered by the trend. This is expected, given the almost nonexistent impact of γ observed in the test results.
- The adjusted reduced frequency also applies to the non-ideal fluid case tested in this research. This achievement greatly expands the applicability of the adjusted reduced frequency parameter.
- The relation does not apply to the higher volumetric flow ratio results. They are therefore not represented in the plot in figure 5.25. Hypothetically, this is a result of the same problems with the flow simulations or their results that have been observed in the simulation data and discussed in more detail in section 5.1. Further research might shed a light on the cause of this discrepancy and hopefully confirm the applicability of the adjusted reduced frequency to stages with higher (or lower) volumetric flow ratios.

For the stages and cases encountered in this thesis work, the relation between the difference between steady and HB flow results (represented by the total-to-total efficiency) and the reduced frequency is

$$\frac{\eta_{TT,St} - \eta_{TT,HB}}{\eta_{TT,St}}[\%] = 0.31 \cdot f_{r,adj} - 0.62 \tag{5.3}$$

This empirical relationship can now be used in an inverse way in order to make decisions on what solver to use for a new case study. By determining the adjusted reduced frequency of a case, the expected accuracy gain from using an harmonic balance solver can be estimated using formula 5.3. The elegance of this adjusted reduced frequency is promising for use as part of a preliminary analysis in the conceptual phase of turbomachinery design. The reduced frequency and work coefficient in particular are parameters that require only information known already in the first stage of design. The maximum Mach number is more problematic in this respect, given the fact that it results from a flow simulation. Consequently, it takes away from the potential of the adjusted reduced frequency parameter to assist in selecting which flow solver to use in the preliminary design phase. Neither averaged inlet or outlet Mach number prove to be a worthy alternative for the local maximum Mach number. Another option is the isentropic Mach number, defined as:

$$M_{is} = \sqrt{\frac{2}{\gamma - 1}\left(R_v^{\frac{1}{\gamma-1}} - 1\right)} \tag{5.4}$$

As the equation suggests, however, the impact of the isentropic Mach is (almost) non-existent, at least for the cases for which both the working fluid and volumetric flow ratio are constant. Flow and work coefficient do not affect the isentropic Mach number, while clearly the maximum Mach number is very

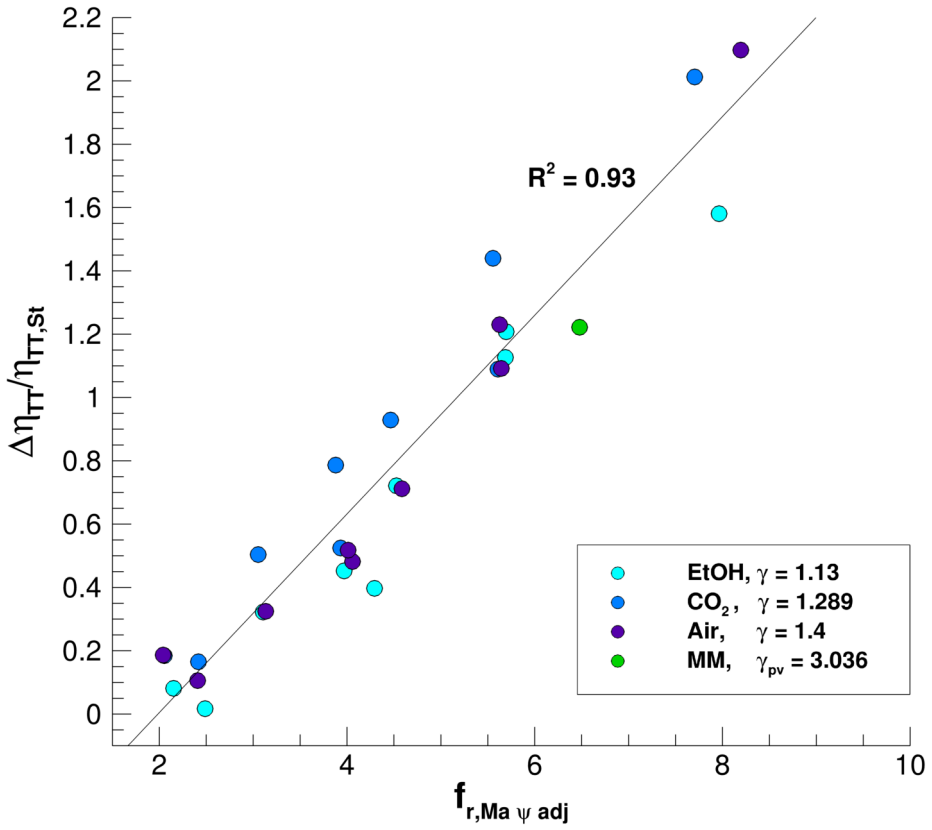

Figure 5.25: Total-to-total efficiency difference between steady-state and HB flow simulation in function of adjusted reduced frequency.

sensitive to both, as shown earlier. Other empirical relations for the Mach number may prove to be more useful. Alternatively, a single steady flow simulation can provide the maximum Mach number of the stage. Within the context of a full design optimization process, this one flow simulation is a small investment.

Depending on the user's requirements, if the expected accuracy gain from an HB solver is sufficiently high, this can justify selecting this more computationally expensive option. The opposite holds as well: if $f_{r,adj}$ found using the relation, and by extension the expected difference in solver performance, is small enough, this can lead the designer to opt for a much more computationally efficient steady-state simulation or optimization.

The results obtained from the simulations in this research and as shown in figure 5.25 indicate that the difference between both solvers would theoretically be zero at an $f_{r,adj} = 2$. Consequently, based on the data at hand, stages with adjusted reduced frequencies of two or lower may well always be resolved using a steady-state solver. As $f_{r,adj}$ increases, it is up to the designer and his/her constraints to determine where the tipping point for accuracy versus computational time lies.

Finally, in order to explore the possibility to obtain an adjusted reduced frequency-like parameter without the limits of human empirical methods, a number of stage parameters are fed to a computer algorithm. The software used for this purpose is *GeneXproTools 5.0*. Data sets with efficiency difference, reduced frequency, inlet Mach, outlet Mach, maximum Mach, work coefficient, specific heat ratio and

volumetric flow ratio are used as inputs to the genetic algorithm (GA). The final equation found by the genetic algorithm and displayed in 5.5 contains a multitude terms and is therefore completely impractical for the purpose of a preliminary design guideline.

$$\begin{aligned}\frac{\eta_{TT,St}-\eta_{TT,HB}}{\eta_{TT,St}}[\%] = &\left[\psi^4 - Ma_{max}^{-3.98/4}\right] + \sqrt[3]{\psi - 6.53}\; Ma_{max}^{1/4} \\ &+\sqrt[4]{6.74+\psi} + \frac{-0.78 + Ma_{max}}{f_r - \psi} + \sqrt[3]{f_r - 5.68}\end{aligned} \tag{5.5}$$

Still, the resulting relation is found to give estimations close to the much more elegant $f_{r,adj}$ indicator proposed earlier. The weight of the chosen parameters is of additional interest. The genetic algorithm clearly assigns the majority of the weight to the work coefficient, maximum Mach number and reduced frequency, in that order. As a result, this small and simplistic GA check at least serves as a rough verification of the empirically derived relation.

6

Conclusion and Recommendations

This final chapter concludes the master thesis report. The main results and achievements of the research are summarized and reviewed against the respective research objectives. The chapter is completed by a set of recommendations for future work in the field.

6.1. Conclusion

Faced with the challenge posed by climate change, the design of thermal engines is increasingly focused on reaching higher levels of efficiency in turbomachines. New flow solving techniques such as the HB method offer an alternative to current industry standards in shape optimization by bridging the gap between rudimentary steady-state solvers and computationally intensive time-accurate unsteady methods. Consequently, questions arise on the precise gains in predictive capability of HB solvers over common steady-state ones. Of particular interest to the community is the how the performance difference between MP and HB solvers depends on the stage type. Consequently, the central research goal of this thesis project is described as follows:

Contribute to the field of turbomachinery design by providing best practices on what flow solving method to use for a specific turbomachinery design problem.

From a diverse set of flow simulations and shape optimizations under varying nondimensional parameters, observations can be made on how these parameters affect the accuracy loss in steady-state flow and optimization results. From there, inverting the reasoning, best practices can be distilled for future design. Based on the observations from this work, the turbomachinery community can make decisions on what flow solver to use for the case at hand.

These are the main findings resulting from this master thesis research:

- The flow coefficient ϕ, work coefficient ψ, working fluid on the basis of γ, non-ideality represented by γ_{Pv} and volumetric flow ratio R_v are identified as parameters of interest when it comes to their variation impacting steady-state versus HB solver behavior.

- It is found that the accuracy difference between steady and HB solver decreases slightly with flow coefficient as reduced frequency goes down and increases significantly with the stage work coefficient as Mach effects increase.
- Varying working fluids under the ideal gas law is found not to impact the stage and solver performance given the volumetric flow ratio is a similarity parameter.
- In cases where γ_{Pv} is significantly larger than γ, a major increase in stage Mach numbers is observed. Consequently, the difference in results found by steady-state and harmonic balance solvers is considerably larger.
- Upon increasing the volumetric flow ratio over the stage, stage efficiencies have found to increase and solver performance differences to decrease. This conclusion does not match expectations nor does it reflect the flow field resulting from the simulation. The cause of this mismatch is expected to lie in the *SU2* solution or post-processing.
- Two sets of steady-state and harmonic balance based blade shape optimizations are performed, illustrating the effects of the behavior observed in flow simulations on a full optimization process and reiterating the difference in computational time between both methods.
- The HB-optimized turbine stages are 0.58% and 0.12% more efficient than the MP-optimized cascades for the *A1* and *B1* geometries respectively. These values do not completely match up with the trends resulting from the simulation results. The iteration process at the base of an optimization might be responsible for enlarging or canceling out differences in flow solver performance. More optimization cases at more different operating conditions are necessary for well-founded conclusions.
- A new design indicator named the adjusted reduced frequency has been introduced. It is based on the reduced frequency, work coefficient and maximum stage Mach number, and defined as $f_{r,adj} = f_r \cdot \psi \cdot Ma_{max}^{1.1}$.
- $f_{r,adj}$ is found to linearly relate to the difference in total-to-total efficiency between that found by steady-state and harmonic balance solvers in flow simulation. They are related as $\frac{\eta_{TT,St}-\eta_{TT,HB}}{\eta_{TT,St}}[\%] = 0.31 \cdot f_{r,adj} - 0.62$.
- The relation between $f_{r,adj}$ and $\frac{\eta_{TT,St}-\eta_{TT,HB}}{\eta_{TT,St}}$ holds for all tested variations of ϕ, ψ, γ and γ_{Pv}. The higher R_v results do not match, most probably due to the general issues with their results discussed earlier.
- $f_{r,adj}$ can be used in the opposite direction to trade-off accuracy and computational time and select the right solver for a given case. Calculating $f_{r,adj}$ for a given case gives an indication of the expected increase in predictive capability when opting for a HB solver instead of an MP one.

6.2. Recommendations

Given the finite time resources associated with a master thesis work, some newly attained insights may be translated into inspiration for future work.

- Automating the geometry generating and meshing process and their interaction may allow for an even larger number of simulations, providing a better and wider range of data for the extraction of trends and guidelines.

- Investigating the discrepancies found for different values of R_v in order to verify the validity of the $f_{r,adj}$ indicator for such cases.
- Performing a higher number and a more varied set of optimizations to verify the validity of $f_{r,adj}$ in an optimization context.
- Validating the guidelines set out in this work with one or more cases (as with a test set in a machine learning process).
- Transforming the design guidelines into a usable (software) tool.
- Extending the work to a 3D context, introducing endwall losses and investigating the validity of the 2D results in that context.
- Extending the work to include stages with one or more extra blade rows in order to study the effect of the propagation of unsteadiness in greater detail.

Bibliography

[1] A. Jameson, *Aerodynamic Design via Control Theory,* , 17.

[2] A. Gopinath, E. van der Weide, J. Alonso, A. Jameson, K. Ekici, and K. Hall, *Three-Dimensional Unsteady Multi-stage Turbomachinery Simulations Using the Harmonic Balance Technique,* in *45th AIAA Aerospace Sciences Meeting and Exhibit* (American Institute of Aeronautics and Astronautics, Reno, Nevada, 2007).

[3] H. Wang, *Adjoint aerodynamic design optimization for blades in multistage turbomachines - part i: Methodology and verification,* Journal of Fluid Mechanics , 15 (2010).

[4] F. Sicot, G. Dufour, and N. Gourdain, *A Time-Domain Harmonic Balance Method for Rotor/Stator Interactions,* Journal of Turbomachinery **134**, 011001 (2012).

[5] J. Erdos, E. Alzner, and W. Mcnally, *Numerical solution of periodic transonic flow through a fan stage,* in *9th Fluid and PlasmaDynamics Conference* (American Institute of Aeronautics and Astronautics, San Diego,CA,U.S.A., 1976).

[6] D. Mavriplis, *Solution of the unsteady discrete adjoint for three-dimensional problems on dynamically deforming unstructured meshes,* Aerospace Sciences meeting and Exibit, AIAA **46** (2008).

[7] A. Rubino, S. Vitale, M. Pini, and P. Colonna, *Assessment of fully-turbulent steady and unsteady adjoint sensitivities for stator-rotor interaction in turbomachinery,* , 8.

[8] J. Denton, *Loss mechanisms in turbomachinery,* Journal of Turbomachinery **115** (1993).

[9] P. Gaetani, *Stator-rotor interaction in axial turbines: Flow physics and design perspective,* ppt (2018).

[10] H. Huang and K. Ekici, *An efficient harmonic balance method for unsteady flows in cascades,* Aerospace Science and Technology **29**, 144 (2013).

[11] K. Hall, J. Thomas, K. Ekici, and D. Voytovich, *Frequency Domain Techniques for Complex and Nonlinear Flows in Turbomachinery (Invited),* in *33rd AIAA Fluid Dynamics Conference and Exhibit* (American Institute of Aeronautics and Astronautics, Orlando, Florida, 2003).

[12] W. Ning and L. He, *Computation of Unsteady Flows Around Oscillating Blades Using Linear and Nonlinear Harmonic Euler Methods,* (1998).

[13] L. He and W. Ning, *Efficient Approach for Analysis of Unsteady Viscous Flows in Turbomachines,* AIAA Journal **36**, 2005 (1998).

[14] K. C. Hall, J. P. Thomas, and W. S. Clark, *Computation of Unsteady Nonlinear Flows in Cascades Using a Harmonic Balance Technique,* , 8.

[15] A. Rubino, M. Pini, and P. Colonna, *Unsteady simulation of quasi-periodic flows in Organic Rankine Cycle cascades using a Harmonic Balance method,* Energy Procedia **129**, 1101 (2017).

[16] A. Rubino, M. Pini, P. Colonna, T. Albring, S. Nimmagadda, T. Economon, and J. Alonso, *Adjoint-based fluid dynamic design optimization in quasi-periodic unsteady flow problems using a harmonic balance method,* Journal of Computational Physics **372**, 220 (2018).

[17] T. Guédeney, A. Gomar, F. Gallard, F. Sicot, G. Dufour, and G. Puigt, *Non-uniform time sampling for multiple-frequency harmonic balance computations,* Journal of Computational Physics **236**, 317 (2013).

[18] K. Ekici, K. C. Hall, and E. H. Dowell, *Computationally fast harmonic balance methods for unsteady aerodynamic predictions of helicopter rotors,* Journal of Computational Physics **227**, 6206 (2008).

[19] G. Cvijetic and H. Jasak, *The Compressible Harmonic Balance Method for Turbomachinery,* in *2018 AIAA Aerospace Sciences Meeting* (American Institute of Aeronautics and Astronautics, Kissimmee, Florida, 2018).

[20] H. Huang and K. Ekici, *A discrete adjoint harmonic balance method for turbomachinery shape optimization,* Aerospace Science and Technology **39**, 481 (2014).

[21] R. D'Amato, *A comparison between steady and unsteady methods for turbomachinery design using scaling analysis*, Master's thesis, Università di Pisa (2018).

[22] T. Verstraete, *Introduction to optimization and multidisciplinary design,* in *Introduction to Optimization and Multidisciplinary Design in Aeronautics and Turbomachinery* (Von Karman Institute for Fluid Dynamics, 2014).

[23] H.-Y. Wu, F. Liu, and H.-M. Tsai, *Aerodynamic Design of Turbine Blades Using an Adjoint Equation Method,* in *43rd AIAA Aerospace Sciences Meeting and Exhibit* (American Institute of Aeronautics and Astronautics, Reno, Nevada, 2005).

[24] B. Walther and S. Nadarajah, *Adjoint-Based Constrained Aerodynamic Shape Optimization for Multistage Turbomachines,* Journal of Propulsion and Power **31**, 1298 (2015).

[25] O. Pironneau, *On optimum design in fluid mechanics,* Journal of Fluid Mechanics **64**, 97 (1974).

[26] A. Jameson, W. Schmidt, and E. Turkel, *Numerical solution of the Euler equations by finite volume methods using Runge Kutta time stepping schemes,* in *14th Fluid and Plasma Dynamics Conference* (American Institute of Aeronautics and Astronautics, Palo Alto,CA,U.S.A., 1981).

[27] C. Ma, X. Su, and X. Yuan, *An Efficient Unsteady Adjoint Optimization System for Multistage Turbomachinery,* Journal of Turbomachinery **139**, 011003 (2016).

[28] H. La Rocca, Oliviero, *Mdo for aerospace applications: On parameterization techniques,* ppt (2017).

[29] J. Luo, J. Xiong, F. Liu, and I. McBean, *Three-Dimensional Aerodynamic Design Optimization of a Turbine Blade by Using an Adjoint Method,* Journal of Turbomachinery **133**, 011026 (2011).

[30] X. Tang, J. Luo, and F. Liu, *Adjoint aerodynamic optimization of a transonic fan rotor blade with a localized two-level mesh deformation method,* Aerospace Science and Technology **72**, 267 (2018).

[31] N. Anand, S. Vitale, M. Pini, and P. Colonna, *Assessment of FFD and CAD-based shape parametrization methods for adjoint-based turbomachinery shape optimization.* (2018).

[32] F. Palacios, J. Alonso, K. Duraisamy, M. Colonno, J. Hicken, A. Aranake, A. Campos, S. Copeland, T. Economon, A. Lonkar, T. Lukaczyk, and T. Taylor, *Stanford University Unstructured (SU^2): An open-source integrated computational environment for multi-physics simulation and design,* in *51st AIAA Aerospace Sciences Meeting including the New Horizons Forum and Aerospace Exposition* (American Institute of Aeronautics and Astronautics, Grapevine (Dallas/Ft. Worth Region), Texas, 2013).

[33] J. A. Keep, S. Vitale, M. Pini, and M. Burigana, *Preliminary verification of the open-source CFD solver SU2 for radial-inflow turbine applications,* Energy Procedia **129**, 1071 (2017).

[34] S. Quoilin, M. V. D. Broek, S. Declaye, P. Dewallef, and V. Lemort, *Techno-economic survey of organic rankine cycle (orc) systems,* Renewable and Sustainable Energy Reviews **22**, 168 (2013).

[35] P. Nederstigt, *Real Gas Thermodynamics and the isentropic behavior of substances*, Master's thesis, TU Delft (2017).

[36] A. Giuffre and M. Pini, *Design guidelines for axial turbines operating with non-conventional fluids,* Turbo Expo 2020 (2020).

[37] J. Denton, *Multall: An open source,cfd based, turbomachinery design system,* Journal of Turbomachinery **139** (2017), 10.1115/1.4037819.

[38] A. Ghidoni, E. Pelizzari, S. Rebay, and V. Selmin, *3d anisotropic unstructured grid generation,* International Journal for Numerical Methods in Fluids **51**, 1097 (2006).

[39] F. Menter, *Zonal two equation k-w turbulence models for aerodynamic flows,* in *23rd Fluid Dynamics, Plasmadynamics, and Lasers Conference*, https://arc.aiaa.org/doi/pdf/10.2514/6.1993-2906 .

[40] P. Spalart and S. Allmaras, *A one-equation turbulence model for aerodynamic flows,* AIAA **439** (1992), 10.2514/6.1992-439.